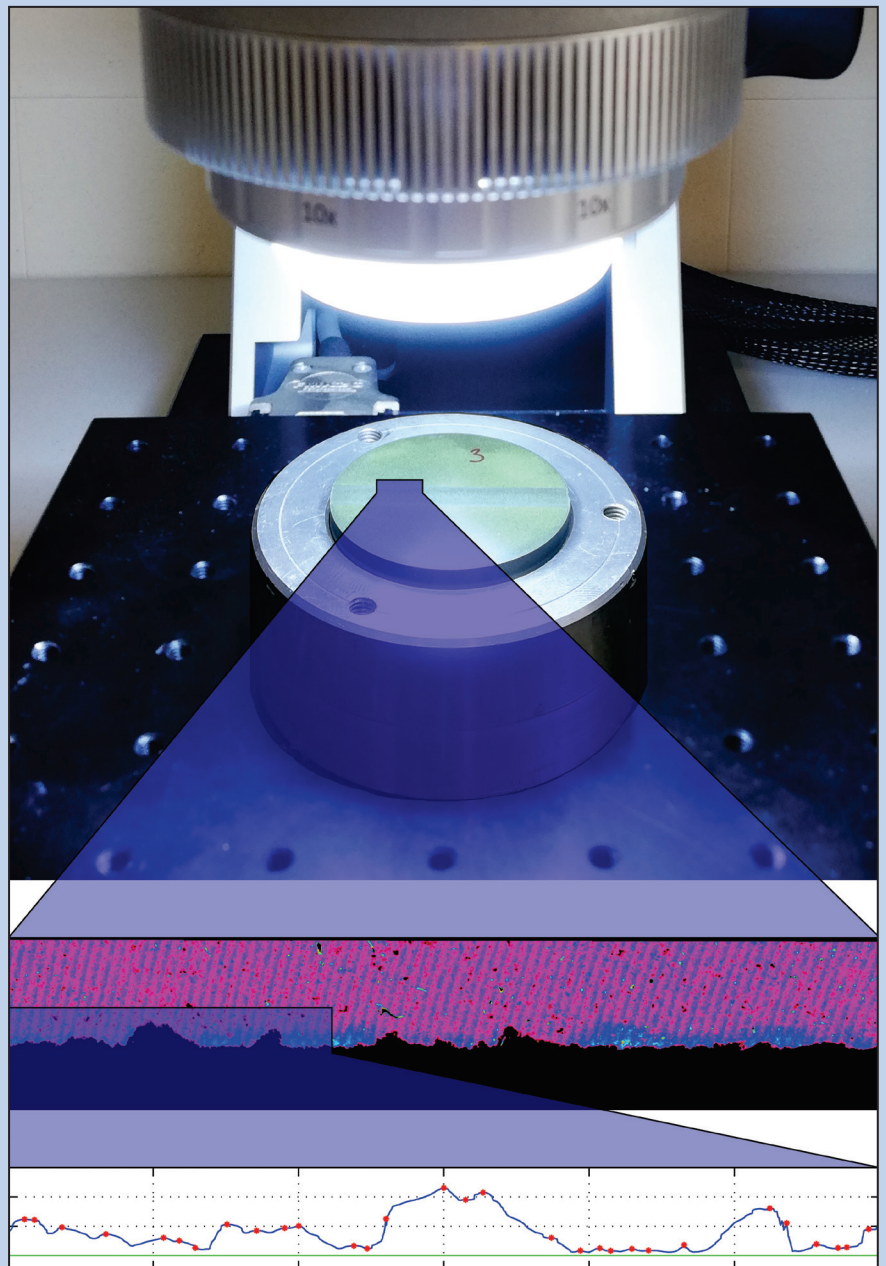




# Strojniški vestnik

## Journal of Mechanical Engineering



no. **10**  
year **2019**  
volume **65**

# Strojniški vestnik – Journal of Mechanical Engineering (SV-JME)

## Aim and Scope

The international journal publishes original and (mini)review articles covering the concepts of materials science, mechanics, kinematics, thermodynamics, energy and environment, mechatronics and robotics, fluid mechanics, tribology, cybernetics, industrial engineering and structural analysis.

The journal follows new trends and progress proven practice in the mechanical engineering and also in the closely related sciences as are electrical, civil and process engineering, medicine, microbiology, ecology, agriculture, transport systems, aviation, and others, thus creating a unique forum for interdisciplinary or multidisciplinary dialogue.

The international conferences selected papers are welcome for publishing as a special issue of SV-JME with invited co-editor(s).

## Editor in Chief

Vincenc Butala

University of Ljubljana, Faculty of Mechanical Engineering, Slovenia

## Technical Editor

Pika Škraba

University of Ljubljana, Faculty of Mechanical Engineering, Slovenia

## Founding Editor

Bojan Kraut

University of Ljubljana, Faculty of Mechanical Engineering, Slovenia

## Editorial Office

University of Ljubljana, Faculty of Mechanical Engineering

SV-JME, Aškerčeva 6, SI-1000 Ljubljana, Slovenia

Phone: 386 (0)1 4771 137

Fax: 386 (0)1 2518 567

info@sv-jme.eu, <http://www.sv-jme.eu>

**Print:** Papirografika, printed in 300 copies

## Founders and Publishers

University of Ljubljana, Faculty of Mechanical Engineering, Slovenia

University of Maribor, Faculty of Mechanical Engineering, Slovenia

Association of Mechanical Engineers of Slovenia

Chamber of Commerce and Industry of Slovenia,

Metal Processing Industry Association

## President of Publishing Council

Mitjan Kalin

University of Ljubljana, Faculty of Mechanical Engineering, Slovenia

## Vice-President of Publishing Council

Bojan Dolšak

University of Maribor, Faculty of Mechanical Engineering, Slovenia

## International Editorial Board

Kamil Arslan, Karabuk University, Turkey

Hafiz Muhammad Ali, King Fahd U. of Petroleum & Minerals, Saudi Arabia

Josep M. Bergada, Politechnical University of Catalonia, Spain

Anton Bergant, Litoštroj Power, Slovenia

Miha Boltežar, University of Ljubljana, Slovenia

Filippo Cianetti, University of Perugia, Italy

Franci Čuš, University of Maribor, Slovenia

Janez Diaci, University of Ljubljana, Slovenia

Anselmo Eduardo Diniz, State University of Campinas, Brazil

Jožef Duhovnik, University of Ljubljana, Slovenia

Igor Emri, University of Ljubljana, Slovenia

Imre Felde, Obuda University, Faculty of Informatics, Hungary

Janez Grum, University of Ljubljana, Slovenia

Imre Horvath, Delft University of Technology, The Netherlands

Aleš Hribernik, University of Maribor, Slovenia

Soichi Ibaraki, Kyoto University, Department of Micro Eng., Japan

Julius Kaplunov, Brunel University, West London, UK

Iyas Khader, Fraunhofer Institute for Mechanics of Materials, Germany

Jernej Klemenc, University of Ljubljana, Slovenia

Milan Kljajin, J.J. Strossmayer University of Osijek, Croatia

Peter Krajnik, Chalmers University of Technology, Sweden

Janez Kušar, University of Ljubljana, Slovenia

Gorazd Lojen, University of Maribor, Slovenia

Thomas Lübben, University of Bremen, Germany

Jure Marn, University of Maribor, Slovenia

George K. Nikas, KADMOS Engineering, UK

Tomaž Pepelnjak, University of Ljubljana, Slovenia

Vladimir Popović, University of Belgrade, Serbia

Franci Pušavec, University of Ljubljana, Slovenia

Mohammad Reza Safaei, Florida International University, USA

Marco Sortino, University of Udine, Italy

Branko Vasić, University of Belgrade, Serbia

Arkady Voloshin, Lehigh University, Bethlehem, USA

## General information

Strojniški vestnik – Journal of Mechanical Engineering is published in 11 issues per year (July and August is a double issue).

Institutional prices include print & online access: institutional subscription price and foreign subscription €100,00 (the price of a single issue is €10,00); general public subscription and student subscription €50,00 (the price of a single issue is €5,00). Prices are exclusive of tax. Delivery is included in the price. The recipient is responsible for paying any import duties or taxes. Legal title passes to the customer on dispatch by our distributor. Single issues from current and recent volumes are available at the current single-issue price. To order the journal, please complete the form on our website. For submissions, subscriptions and all other information please visit: <http://www.sv-jme.eu>.

You can advertise on the inner and outer side of the back cover of the journal. The authors of the published papers are invited to send photos or pictures with short explanation for cover content.

We would like to thank the reviewers who have taken part in the peer-review process.

The journal is subsidized by Slovenian Research Agency.

Strojniški vestnik - Journal of Mechanical Engineering is available on <https://www.sv-jme.eu>.



### Cover:

Precise 3D measurements, performed on the Alicona InfiniteFocusSL measuring system, used to assess the chipping of ceramic workpiece edges after milling.

### Image courtesy:

University of Ljubljana,  
Faculty of Mechanical Engineering,  
Chair of Machining Technology Management,  
Slovenia

ISSN 0039-2480, ISSN 2536-2948 (online)

© 2019 Strojniški vestnik - Journal of Mechanical Engineering. All rights reserved. SV-JME is indexed / abstracted in: SCI-Expanded, Compendex, Inspec, ProQuest-CSA, SCOPUS, TEMA. The list of the remaining bases, in which SV-JME is indexed, is available on the website.

# Contents

**Strojniški vestnik - Journal of Mechanical Engineering**  
**volume 65, (2019), number 10**  
**Ljubljana, October 2019**  
**ISSN 0039-2480**

**Published monthly**

## **Papers**

- David Muženič, Jaka Dugar, Davorin Kramar, Matija Jezeršek, Franci Pušavec: Improvements in Machinability of Zinc Oxide Ceramics by Laser-Assisted Milling 539
- Daniel Miler, Stanko Škec, Branko Katana, Dragan Žeželj: An Experimental Study of Composite Plain Bearings: The Influence of Clearance on Friction Coefficient and Temperature 547
- Thangavel Yuvaraj, Paramasivam Suresh: Analysis of EDM Process Parameters on Inconel 718 Using the Grey-Taguchi and Topsis Methods 557
- Fariha Mukhtar, Faisal Qayyum, Hassan Elahi, Masood Shah: Studying the Effect of Thermal Fatigue on Multiple Cracks Propagating in an SS316L Thin Flange on a Shaft Specimen Using a Multi-Physics Numerical Simulation Model 565
- Mohammad Hadi Izadi, Shahrokh Hosseini Hashemi, Moharam Habibnejad Korayem: Buckling of Joined Composite Conical Shells Using Shear Deformation Theory under Axial Compression 574
- Roman Satošek, Michal Valeš, Tomaž Pepelnjak: Study of Influential Parameters of the Sphere Indentation Used for the Control Function of Material Properties in Forming Operations 585
- Chang Wang, Jun Liu, Zhiwei Luo: Suppression of Self-Excited Vibrations in Rotating Machinery Utilizing Leaf Springs 599



# Improvements in Machinability of Zinc Oxide Ceramics by Laser-Assisted Milling

David Muženič\* – Jaka Dugar – Davorin Kramar – Matija Jezeršek – Franci Pušavec  
University of Ljubljana, Faculty of Mechanical Engineering, Slovenia

*In this paper, an attempt is made to advance the understanding of Laser-Assisted Milling (LAMill) of zinc oxide (ZnO) electronic ceramics. A series of conventional milling and LAMill experiments with varying laser power were conducted to determine the effect of laser assistance on the machinability of this material. Improved machinability in terms of reduction in machined surface roughness and edge chipping was achieved by adjusting laser power. At an optimal laser power of 120 W, determined for the machining parameters used,  $R_a$  and  $R_z$  were reduced by 37 % and 46 %, respectively, while the average and maximum chipping widths were reduced by 15 % and 17 %, respectively.*

**Keywords:** zinc oxide (ZnO) ceramics, machinability, laser-assisted milling, surface roughness, edge chipping

## Highlights

- This paper deals with LAMill of ZnO electronic ceramics; milling of ZnO electronic ceramics has not been researched previously.
- Conventional milling and LAMill experiments using various levels of laser power were conducted.
- The effect of laser power on the machined surface integrity was determined in terms of surface roughness and interior edge chipping.
- Optimal level of laser power was proposed for the used machining conditions.

## 0 INTRODUCTION

Machinability in cutting processes, which is the ability to economically machine a certain material, is usually closely related to the performance of the to-be-cut material. Engineering ceramics are known for their poor machinability due to high hardness and brittleness. Thus, often the state-of-the-art in precision shaping of these materials are low material-removal rate processes, e.g. grinding and lapping, resulting in high machining costs. Nowadays, new ceramic materials are being developed in different areas of the industry (e.g. electronic ceramics). These ceramics are usually not known for high hardness or strength, yet high brittleness and low fracture toughness that lead towards excessive edge chipping. Therefore, machinability of these materials is significantly reduced. Edge chipping of ceramics is sudden edge damage on the macro- or microscale, caused by fractures usually while the cutting tool either comes in contact or separates from the workpiece. Ng et al. [1] described three types of edge chipping, namely entry edge chipping, interior edge chipping and exit edge chipping (Fig. 1), while milling a tetrasilic mica glass ceramic. On finished parts, the presence of edge chipping is detrimental to the mechanical characteristics as well as dimensional and geometrical accuracy, and often severely limits the productivity of ceramic machining processes.

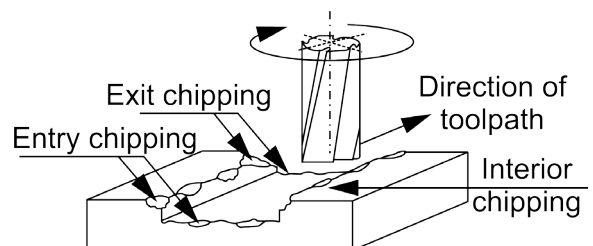


Fig. 1. Types of edge chipping [1]

Some improvements in machinability of both structural and electronic ceramics were achieved by optimizing the conventional fixed abrasive machining processes [2]. Besides improvements in conventional processes, large reductions in cutting forces and edge chipping in ceramics fixed abrasive machining were achieved with ultrasonic oscillations of the cutting tool during machining [3]. Another hybrid approach to fixed abrasive machining of silicon nitride ( $\text{Si}_3\text{N}_4$ ) structural ceramics was presented by Guerrini et al. [4]. The authors proposed a combined process wherein a laser source is used to induce controlled cracking of the workpiece material surface, which aids the consequent grinding process. Zhang et al. [5] have adopted a similar shaping approach for zirconium oxide ceramics. Besides improvements in fixed abrasive machining processes, other non-traditional or hybrid processes such as electrical-discharge machining [6], laser machining [7] and thermally

\*Corr. Author's Address: University of Ljubljana, Faculty of Mechanical Engineering, Aškerčeva cesta 6, Ljubljana, Slovenia, david.muzenic@fs.uni-lj.si

enhanced machining [8] have been used to address the poor machinability of ceramic materials.

In thermally enhanced machining, a heat source is used to heat the workpiece material right before the cutting zone, resulting in local softening of the to-be-cut material. By heating ceramic materials above a certain temperature, a reduction in hardness can be achieved as well as the change in deformation behaviour from brittle to ductile [9]. Amongst the thermally enhanced machining processes, laser-assisted machining (LAM) has been shown to be superior method for improving the machinability of different structural ceramics due to the ability of a fast, local and controlled input of heat into the workpiece material. In comparison to grinding and lapping, much higher material-removal rates can be achieved in LAM, leading to a significant reduction in machining costs. Lei et al. [10] evaluated the potential of laser-assisted turning (LAT) as an economically viable process for the fabrication of precision  $\text{Si}_3\text{N}_4$  ceramic parts. Compared to the conventional diamond grinding, a decrease in the thickness of the subsurface damage layer was observed, while achieving tool life, comparable to metal cutting. Tian et al. [11] also report on achieving tool life, comparable to metal cutting, while successfully producing  $\text{Si}_3\text{N}_4$  parts with complex geometry. Pfefferkorn et al. [12] demonstrated the feasibility of LAT of magnesia-partially-stabilized zirconia (PSZ) by achieving a process with 0 % flaws, which would cause a workpiece to be scrapped. The experiments showed that at a laser power of 100 W, the material removal temperature rises to 530 °C and the material can be successfully machined, although a PCBN-tipped tool life was only 3 min. Further increasing the laser power to 250 W leads to a material removal temperature of 1210 °C and a drastic increase in tool life (up to 120 min). While several studies on LAT of structural ceramics are reported in literature, the authors found only two reports on laser-assisted milling (LAMill) of these materials. The possible reasons for that are that LAMill is generally more complex than LAT with regards to the laser setup and in the case of brittle materials, milling is significantly more subjected to workpiece edge chipping than turning. Tian et al. [13] achieved good surface finish, repeatable performance and acceptable tool wear in LAMill of  $\text{Si}_3\text{N}_4$  ceramics using TiAlN coated carbide tools, although the problem of edge chipping was not addressed in this study. A detailed study on edge chipping mechanisms in LAMill of this material was presented by Yang et al. [9]. The authors concluded that by heating the material above the softening point, edge chipping is

reduced due to the reduction in cutting forces. By heating the material further, above the brittle/ductile transition temperature, edge toughness of  $\text{Si}_3\text{N}_4$  is increased significantly, resulting in a further reduction of edge chipping.

In this study, an attempt is made to advance the understanding of LAMill on the machinability of zinc oxide (ZnO) based electronic ceramic. Detailed information about the composition and preparation of this ceramic is provided in [14]. Lapping process represents the state of the art in machining of ZnO ceramic. Achieving a successful milling operation, however, would result in a drastic increase in quality, achievable material removal rate and consequently a decrease in machining costs. No reports on machining of this material can be found in literature, nor information about the material edge toughness or edge chipping tendencies. The authors performed preliminary studies on conventional milling of ZnO ceramics and concluded that conventional milling is not appropriate for its machining and that edge chipping is the main factor, reducing its machinability. The latter is supported by comparing the fracture toughness of zinc oxide ceramics (2.10  $\text{MPa}\cdot\text{m}^{1/2}$  to 2.16  $\text{MPa}\cdot\text{m}^{1/2}$  [15]) to previously discussed structural ceramics (for example  $\text{Si}_3\text{N}_4$ , 4  $\text{MPa}\cdot\text{m}^{1/2}$  to 8  $\text{MPa}\cdot\text{m}^{1/2}$  [16]).

Based on the similarities between ZnO ceramics and other electronic ceramics, or even structural ceramics, the authors assume that laser assistance should provide significant machinability improvement in milling of ZnO ceramic material. Therefore, the aim of this study is defining the effect of laser assistance on the machinability of zinc oxide ceramics. To observe laser assistance significance, only laser power was varied throughout the experimental repetitions, while the machining parameters were kept constant at levels that were found as optimal by the preliminary conventional milling experiments.

## 1 EXPERIMENTAL PROCEDURE

### 1.1 Laser-Assisted Milling Experiments

The laser-assisted dry milling experiments were performed on a 3-axis Mori Seiki Frontier M1 vertical machining center, equipped with a 400 W YLR-400-AC continuous wave fiber laser from IPG Photonics with a wavelength of 1070 nm and the collimated laser beam diameter of 5 mm. The cutting tool used in the experiments was a DIXI 72420 PCD end mill with a diameter of 4 mm and a single cutting edge.

A depth and width of cut of 0.1 mm and 0.33 mm, respectively, a feed velocity of 250 mm/min, a spindle speed of 6250 rev/min ( $v_c = 78.5$  m/min and  $f_z = 0.04$  mm) and the position of the laser spot relative to the cutting tool (Fig. 2) were kept constant throughout all experimental repetitions. For every experimental repetition, a 4 mm wide and 0.1 mm deep slot was milled at the centre of the workpiece in the  $x$ -direction without laser assistance and then two consecutive LAMill passes with the same width of cut in the positive  $y$ -direction were performed, as shown in Fig. 2.

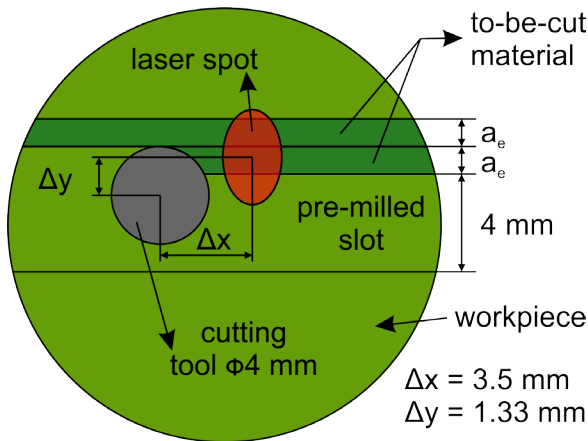


Fig. 2. Laser-assisted milling strategy

Table 1 shows the plan of laser-assisted milling experiments. Experiments N° 1 to 6 were performed with two repetitions with the same experimental parameters, each time on a new workpiece. As the results indicated an area of interest between the two used levels of laser power, four more experiments (N° 7 to 10) were performed, with one repetition per laser power used.

1.2 Surface Integrity Analysis

Surface integrity was evaluated in terms of interior edge chipping and machined surface roughness. For the purpose of surface integrity analysis, a 3D scan including the edge and the surface, generated in the two machining passes, shown in Fig. 2, was executed on an Alicona InfiniteFocusSL measurement system.

The measurement setup used for surface integrity analysis is shown in Fig. 3.

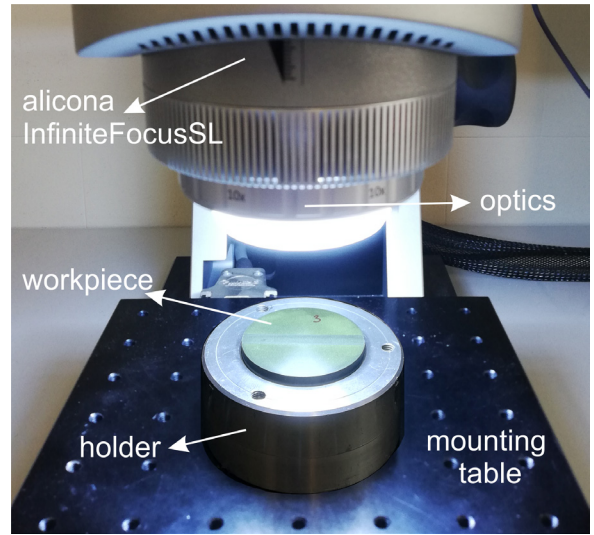


Fig. 3. Surface integrity measurement setup

Edge chipping was evaluated by fitting a reference plane on the portion of un-machined surface in the scan and extracting the intersection curve of a plane 5 μm below the reference plane and the scanned surface. A plot of the distance from the reference plane for the case 0W<sub>1</sub>, where the lower limit of the colour scale was set to - 5 μm and thus evidencing the detected edge as the border of the black-coloured area is shown in Fig. 4a). A portion of the detected edge around the maximum detected chipping for the case 0W<sub>1</sub> is shown in Fig. 4b). Edge chipping is characterized by the chipping widths,  $w_{c,n}$ , which are the normal distances from the ideal edge, without edge defects (green line), to the local extremes (red marks) of the detected edge (blue line), as shown in Fig. 4 b). Two parameters were chosen to evaluate edge chipping, namely maximum ( $w_{c,max}$ ) and average ( $w_{c,avg}$ ) chipping width, which are the maximum and mean value of the detected chipping widths in an experimental repetition, respectively.

Surface roughness at the machined surface (black area in Fig. 4a) was measured on three different randomly selected 5 mm long profiles in the  $x$ -direction for every experimental repetition. For each profile an average of 5 profiles, each 10 μm

Table 1. Plan of laser-assisted milling experiments

N°	1	2	3	4	5	6	7	8	9	10
P [W]	0	0	80	80	160	160	110	120	130	140
label	0W <sub>1</sub>	0W <sub>2</sub>	80W <sub>1</sub>	80W <sub>2</sub>	160W <sub>1</sub>	160W <sub>2</sub>	110W <sub>1</sub>	120W <sub>1</sub>	130W <sub>1</sub>	140W <sub>1</sub>

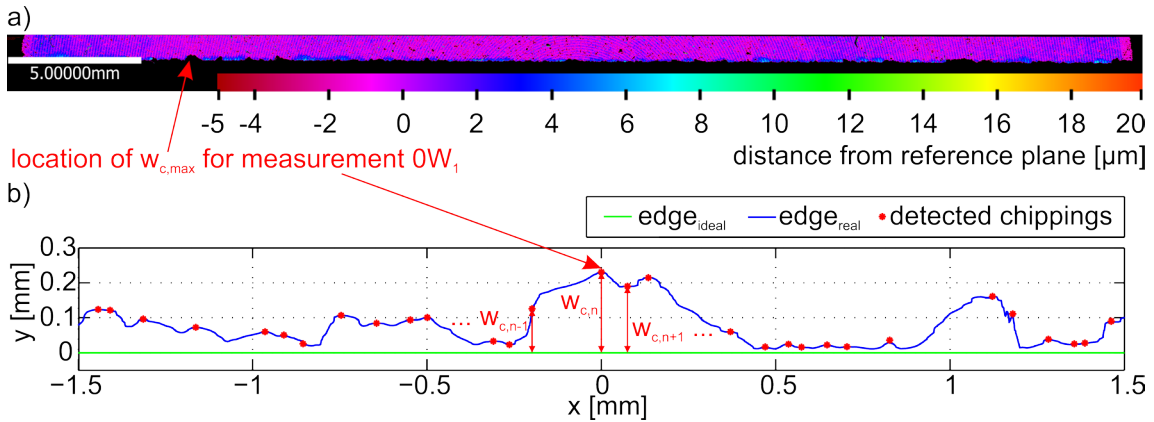


Fig. 4. Edge chipping: a) detection methodology and b) definition

apart in the  $y$ -direction, was taken into account and a cut-off wavelength of  $800 \mu\text{m}$  was used to eliminate waviness.

## 2 RESULTS AND DISCUSSION

The effects of laser power on the surface integrity of milled ZnO ceramic parts was evaluated in terms of machined surface roughness (chapter 2.1) and interior edge chipping (chapter 2.2). Furthermore, optimal level of laser power is discussed in chapter 2.3.

### 2.1 Surface Roughness

To evaluate the machined surface roughness,  $R_a$  and  $R_z$  were chosen as representative parameters. Fig. 5 shows the results of surface roughness measurements, grouped by the laser power used. Each vertical bar represents the highest and lowest measured value, while the connecting line represents the mean value for each group of experiments. Note that for laser powers of 0 W, 80 W and 160 W, six measurements are included in the group, while only three measurements are included in the other groups.

The results are showing that both  $R_a$  and  $R_z$  decrease with laser power almost linearly from 0 W to 110 W, followed by a sharp decrease at 120 W and a slight increase with further increasing the laser power. This suggests that 120 W is the optimal laser power level when milling ZnO ceramics with the proposed machining parameters. Furthermore, the difference between the highest and lowest measured  $R_a$  or  $R_z$ , for a fixed laser power, decreases drastically when increasing the laser power above 80 W. This suggests an improvement in process stability while increasing

the laser power above a threshold value between 80 W and 110 W.

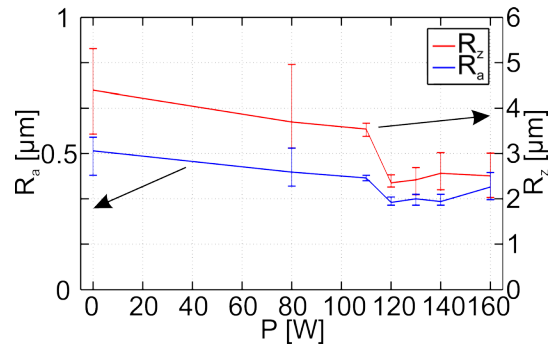


Fig. 5. Effect of laser power on machined surface roughness

The results are indicating that machined surface roughness is in direct correlation with the occurrence of grain pull-out during machining. The latter is facilitated by the brittleness of the thin layer of Bi-rich intergranular phase, through which the cracks propagate during brittle fracture of this material at room temperature. By preheating the workpiece material before cutting, the intergranular phase softens, inhibiting grain pull-out. Furthermore, the authors assume that at a threshold value of laser power between 80 W and 110 W, the material is heated above the glassy transition temperature of the Bi-rich intergranular phase ( $\sim 350 \text{ }^\circ\text{C}$  [17]), resulting in changes in the deformation behaviour and the material removal mechanism. A brittle/ductile transition, like in the case of  $\text{Si}_3\text{N}_4$  [9], where random cracks during brittle fracture are replaced by the viscous flow of the workpiece material, would explain the increase in process stability. This means that, optimally, the laser power should be kept just above that point (120 W),

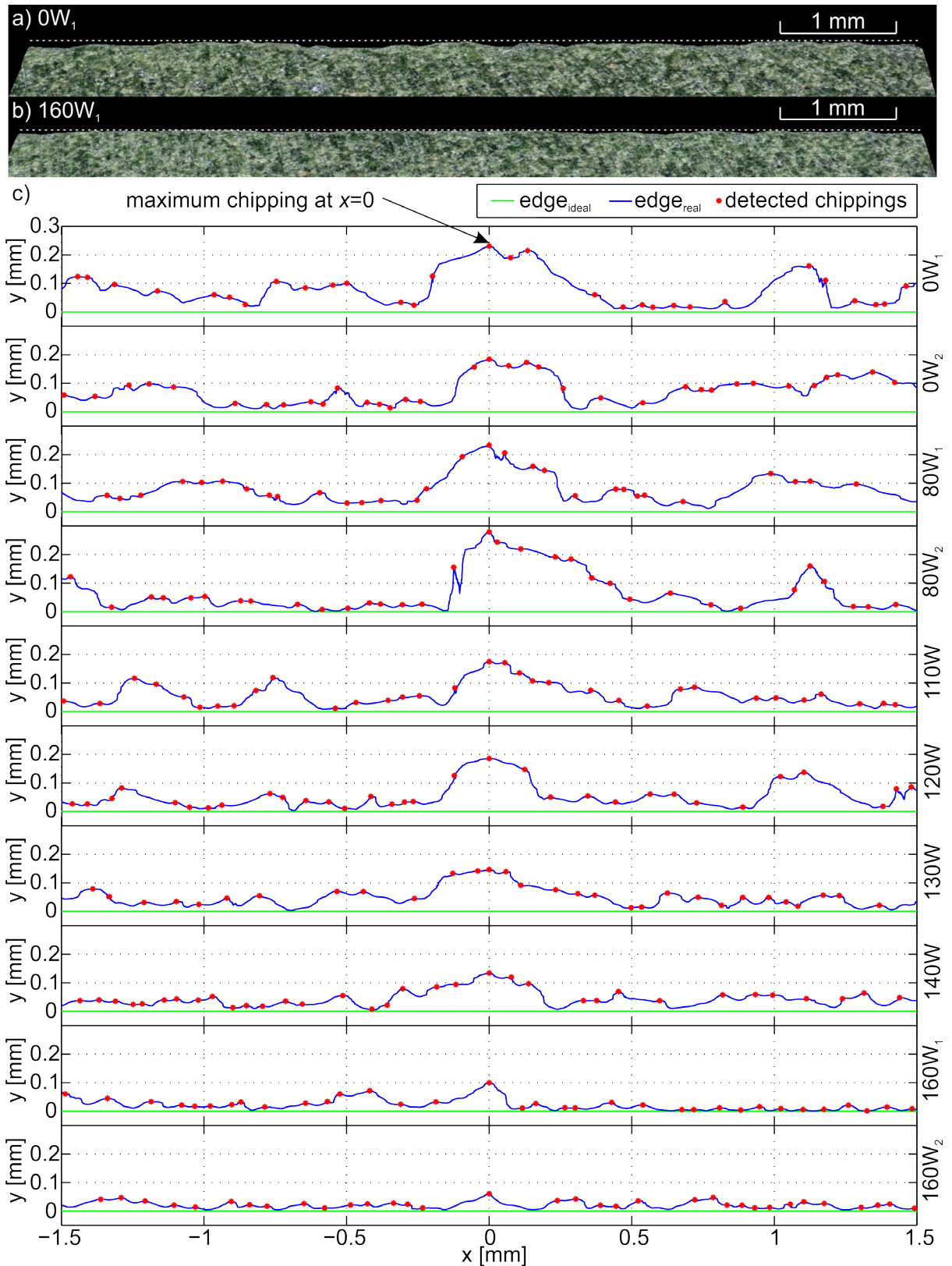


Fig. 6. Sample edge, achieved with a) conventional milling and b) LAMill using a laser power of 160 W and c) area around the maximum detected edge chipping for every experimental repetition

as using higher power does not lead to improvements in surface roughness and results in cracks on the machined surface (Fig. 8).

## 2.2 Edge Chipping

Laser assistance has also a significant effect on interior edge chipping; however, its correlation with laser power differs from the findings of surface roughness. A sample edge, achieved with conventional milling in  $0W_1$  and a sample edge from  $160W_1$ , where the best results regarding edge chipping were achieved, are presented in Fig. 6(a) and b), respectively. Fig. 6 c) shows the area around  $w_{c,max}$  (centred at  $x = 0$ ) for every experimental repetition and the detected chippings. It can be seen that the definition of a chipping differs from the literature [9] and [18]. To clarify, in this work, a chipping detection algorithm based on local extremes was constructed and used. In contrast with the other definitions of a chipping, several detected chippings in the area of a single, longer (in the  $x$ -direction) chipping are detected. However, as stated by Yang et al. [9], the maximum chipping width and the chipping area, which is the area surrounded by the real and ideal edges in Fig. 4, are independent of the chipping definition. Moreover, as the plot of chipping area shows the same trend as the  $w_{c,avg}$  in Fig. 7, the authors consider the algorithm to be appropriate for edge chipping evaluation. The dependence of  $w_{c,max}$  and  $w_{c,avg}$  on laser power is presented in Fig. 7. A trend line is added to the data as a third degree polynomial fit. It can be seen that both  $w_{c,max}$  and  $w_{c,avg}$  increase with laser power, for low laser powers, and then decrease linearly for laser powers above 80 W, with the values at 80 W still being significantly larger than at 0 W. This suggests that the optimal laser power for the machining parameters used is outside the tested range, above 160 W.

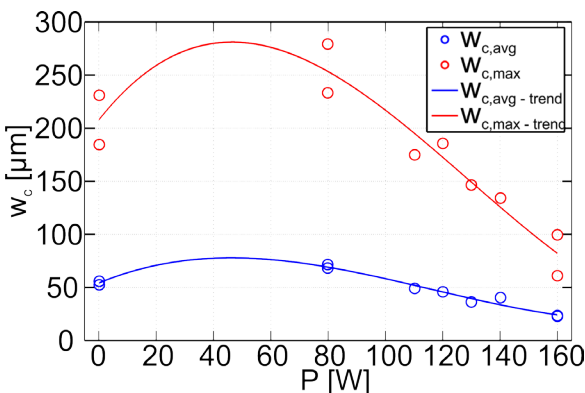


Fig. 7. Edge chipping for different laser powers

It can be seen in Fig. 7 that the benefits of laser assistance are only achieved with laser powers exceeding 110 W, where both  $w_{c,max}$  and  $w_{c,avg}$  are reduced, compared to those, achieved by conventional milling. This suggests that the glassy transition of the Bi-rich intergranular phase plays an important role in interior edge chipping as well as in the previously discussed surface roughness. Similarly, for the case of  $\text{Si}_3\text{N}_4$ , Yang et al. [9] report that there are two factors, contributing to edge toughness. Firstly, edge chipping is reduced due to reduction in cutting forces in LAMill and secondly, while increasing laser power so to heat the material above the glassy transition temperature, the edge toughening mechanism takes place, further reducing edge chipping.

## 2.3 Optimal Level of Laser Power

This study showed that positive effects on the machinability of ZnO ceramics in terms of reduction of interior edge chipping and improved machined surface quality can be achieved with laser assistance by adjusting laser power. At a laser power of 120 W,  $R_a$  and  $R_z$  were reduced by 37 % and 46 %, respectively, compared to conventional milling, and a 4.5- and 7-fold reduction in the difference between the highest and lowest measured values was observed for  $R_a$  and  $R_z$ , respectively at this laser power. The highest reduction of edge chipping was obtained at the highest laser power used, 160 W, where the average and maximum chipping widths were reduced by 55 % and 60 %, respectively. However, using this level of laser power resulted in cracks in the workpiece due to thermal shock, as shown in Fig. 8. The stresses, as a consequence of excessive temperature gradient are causing this problem. Based on this, the minimum power above the glassy transition point is considered as the most reliable choice by the authors (i.e. 120 W). By using a laser power of 120 W, the average and maximum chipping widths were reduced by 15 % and 17 %, respectively.

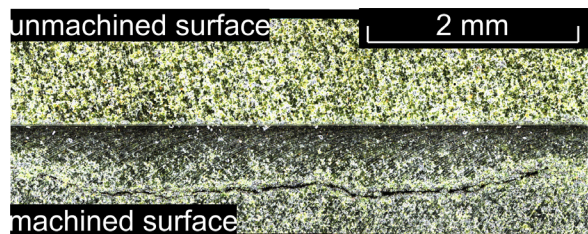


Fig. 8. Thermal crack, formed when using a laser power of 160 W

## 3 CONCLUSIONS

The paper contributes to an advanced understanding of laser assistance and represents a pioneering work in the field of LAMill of ZnO electronic ceramics. Conventional milling and LAMill experiments, using various levels of laser power, were conducted to determine the effect of laser power on the machined surface integrity. The key findings of this research are summarized as follows.

- Edge chipping is the main factor, reducing the machinability of ZnO ceramics. Laser assistance can improve the machinability of ZnO ceramics by reducing edge chipping and improving surface roughness. For the machining parameters used, an optimal level of laser power exists, where the highest improvement in machinability was achieved.
- At the optimal level of laser power of 120 W,  $R_a$  and  $R_z$  were reduced by 37 % and 46 %, respectively.
- By using a laser power of 120 W, the average and maximum chipping widths were reduced by 15 % and 17 %, respectively. Higher reductions in edge chipping were achieved at higher levels of laser power, but cracks due to thermal shock started to appear on the machined surface.

Although the novel approach of LAMill applied in this study showed an improvement in the machinability of this material, many areas are yet to be researched to fully understand and implement LAMill in ZnO ceramic part production. As concluded previously, edge chipping is considered the main factor reducing the machinability of ZnO ceramics and LAMill of this material is limited by thermal shock. Therefore, a thermal model that can reliably predict temperatures near the edges of the workpiece after laser heating is crucial for further studies of LAMill of this material. Furthermore, the mechanisms that result in the improvement of surface integrity, while machining ZnO at high temperatures have to be researched to master LAMill of ZnO.

## 4 ACKNOWLEDGEMENTS

The authors would like to thank the Slovenian Research Agency (ARRS) for their financial support through the P2-0266 Research Program and prof. dr. Slavko Bernik from the Department for Nanostructured materials at the Jožef Stefan Institute for his support with knowledge in the field of ZnO ceramics.

## 5 REFERENCES

- [1] Ng, S.J., Le, D.T., Tucker, S.R., Zhang, G. (1996). Control of Machining Induced Edge Chipping on Glass Ceramics. Institute of System Research, University of Maryland, College Park.
- [2] Shih, A.J., Denkena, B., Grove, T., Curry, D., Hocheng, H., Tsai, H.-Y., Ohmori, H., Katahira, K., Pei, Z.J. (2018). Fixed abrasive machining of non-metallic materials. *CIRP Annals*, vol. 67, no. 2, p. 767-790, DOI:10.1016/j.cirp.2018.05.010.
- [3] Wang, J., Zhang, J., Feng, P., Guo, P. (2018). Damage formation and suppression in rotary ultrasonic machining of hard and brittle materials: A critical review. *Ceramics International*, vol. 44, no. 2, p. 1227-1239, DOI:10.1016/j.ceramint.2017.10.050.
- [4] Guerrini, G., Fortunato, A., Melkote, S.N., Ascari, A., Lutey, A.H.A. (2018). Hybrid laser assisted machining: A new manufacturing technology for ceramic components. *Procedia CIRP*, vol. 74, p. 761-764, DOI:10.1016/j.procir.2018.08.015.
- [5] Zhang, X., Deng, Z., Ren, Y., Chen, G., Liu, W., Zhang, G. (2015). Laser-induced deterioration grinding of zirconium oxide (ZrO<sub>2</sub>) – generation of layer patterns and performance evaluation. *Strojniški vestnik - Journal of Mechanical Engineering*, vol. 61, no. 12, p. 689-697, DOI:10.5545/sv-jme.2015.2794.
- [6] Pachaury, Y., Tandon, P. (2017). An overview of electric discharge machining of ceramics and ceramic based composites. *Journal of Manufacturing Processes*, vol. 25, p. 369-390, DOI:10.1016/j.jmapro.2016.12.010.
- [7] Samant, A.N., Dahotre, N.B. (2009). Laser machining of structural ceramics-a review. *Journal of the European Ceramic Society*, vol. 29, no. 6, p. 969-993, DOI:10.1016/j.jeurceramsoc.2008.11.010.
- [8] Sun, S., Brandt, M., Dargusch, M.S. (2010). Thermally enhanced machining of hard-to-machine materials—a review. *International Journal of Machine Tools and Manufacture*, vol. 50, no. 8, p. 663-680, DOI:10.1016/j.ijmactools.2010.04.008.
- [9] Yang, B., Shen, X., Lei, S. (2009). Mechanisms of edge chipping in laser-assisted milling of silicon nitride ceramics. *International Journal of Machine Tools and Manufacture*, vol. 49, no. 3-4, p. 344-350, DOI:10.1016/j.ijmactools.2008.09.006.
- [10] Lei, S., Shin, Y.C., Incropera, F.P. (2001). Experimental investigation of thermo-mechanical characteristics in laser-assisted machining of silicon nitride ceramics. *Journal of Manufacturing Science and Engineering - Transactions of the ASME*, vol. 123, no. 4, p. 639-646, DOI:10.1115/1.1380382.
- [11] Tian, Y.G., Shin, Y.C. (2006). Thermal modeling for laser-assisted machining of silicon nitride ceramics with complex features. *Journal of Manufacturing Science and Engineering - Transactions of the ASME*, vol. 128, no. 2, p. 425-434, DOI:10.1115/1.2162906.
- [12] Pfefferkorn, F.E., Shin, Y.C., Tian, Y.G., Incropera, F.P. (2004). Laser-assisted machining of magnesia-partially-stabilized zirconia. *Journal of Manufacturing Science and Engineering - Transactions of the ASME*, vol. 126, no. 1, p. 42-51, DOI:10.1115/1.1644542.
- [13] Tian, Y.G., Wu, B.X., Anderson, M., Shin, Y.C. (2008). Laser-assisted milling of silicon nitride ceramics and inconel 718. *Journal of Manufacturing Science and*

*Engineering - Transactions of the ASME*, vol. 130, no. 3, DOI:10.1115/1.2927447.

- [14] Bernik, S. (2017). Influence of granulate and pressure on green compacts and the current-voltage characteristics of sintered zno-based varistor ceramics. *Journal of Microelectronics, Electronic Components and Materials*, vol. 47, no. 3, p. 171-177.
- [15] Roy, T.K. (2015). Assessing hardness and fracture toughness in sintered zinc oxide ceramics through indentation technique. *Materials Science and Engineering: A*, vol. 640, p. 267-274, DOI:10.1016/j.msea.2015.05.107.
- [16] Ferraris, E., Vleugels, J., Guo, Y., Bourell, D., Kruth, J.P., Lauwers, B. (2016). Shaping of engineering ceramics by electro, chemical and physical processes. *CIRP Annals*, vol. 65, no. 2, p. 761-784, DOI:10.1016/j.cirp.2016.06.001.
- [17] Kim, Y. J., Hwang, S. J., Kim, H. S. (2006). Thermal Properties of Bi2O3-B2O3-ZnO Glass System. *Materials Science Forum*, vol. 510-511, p. 578-581, DOI:10.4028/www.scientific.net/MSF.510-511.578.
- [18] Ohbuchi, Y., Matsuo, T., Sakat, M. (1995). Chipping in high-precision slot grinding of Mn-Zn ferrite. *CIRP Annals*, vol. 44, no. 1, p. 273-277, DOI:10.1016/S0007-8506(07)62324-5.

# An Experimental Study of Composite Plain Bearings: The Influence of Clearance on Friction Coefficient and Temperature

Daniel Miler<sup>1</sup> – Stanko Škec<sup>1,2\*</sup> – Branko Katana<sup>1</sup> – Dragan Žeželj<sup>1</sup>

<sup>1</sup> University of Zagreb, Faculty of Mechanical Engineering and Naval Architecture, Croatia

<sup>2</sup> Technical University of Denmark, Denmark

*Plain bearings are often used due to their compact dimensions and low cost. Their frictional and wear properties are affected by several parameters: load, sliding velocity, temperature, and surface roughness, among others. In this article, the authors have experimentally investigated the influence of clearance size on the friction and wear in composite plain bearings. An experimental rig was designed to enable the testing of plain bearings in working conditions similar to those encountered throughout their exploitation. Two load levels, two lubrication types, and four clearance levels were varied, resulting in 48 experiments, as each was replicated twice. The friction coefficient and bearing temperature were measured during the experiment, while the material loss and change in surface roughness were determined post-experiment. The results have shown that clearance affects the friction in both the dry running specimens and specimens lubricated using a solid lubricant (polytetrafluoroethylene).*

**Keywords:** clearance, composite, friction coefficient, plain bearing.

## Highlights

- The influence of plain bearing clearance on friction coefficient, temperature, and wear was studied.
- The experiment was designed as the full factorial; loads, lubrication regimes, and clearance sizes were varied.
- In dry running specimens, the friction coefficient reduces as the clearance size is increased, while in PTFE-lubricated specimens local minimum must be found.
- In specimens tested at 65 N load, the linear relation between the friction coefficient and the bearing temperature was found.

## 0 INTRODUCTION

The bearings enable relative linear or rotational motion between the two parts by reducing the friction coefficient. Plain bearings are a frequently used bearing sub-type, most likely due to their fairly simple geometry and low manufacturing cost. Since no additional rolling elements are required, their outer diameter is small, while the large contact surface increases the load-carrying capacity. The performance of a plain bearing can be evaluated through a number of criteria, such as its efficiency [1], durability [2], or load-carrying capacity [3]. As such, it is influenced by several parameters: load, sliding velocity, operating temperature, surface roughness, clearance between the plain bearing and the shaft [4], and material.

Composite materials are often used in the design of machine elements to provide engineers with a wider range of possibilities in terms of material mechanical properties. The composites have diverse mechanical properties, which are usually achieved by combining different matrix, filler, and reinforcement materials. For example, polymer matrices are chemically resistant but are adversely affected by an increase in temperature. As noted by Prehn et al. [5], a chemically resistant polymer matrix (polyetheretherketone and epoxy resin were used in the referenced study)

embedded with fibre reinforcement (CF) and filler (SiC) has improved wear properties while also enabling use in adverse environments, such as seawater [6]. Further, the working temperature often narrows the suitable matrix materials to thermally resistant ones; for example, an increase in temperature decreases the mechanical properties of polymers [7], such as the tensile strength, permissible Hertzian stress, and Young modulus, rendering them unusable. Increase in temperature reduces the tensile strength, permissible Hertzian (contact) stress, and Young modulus of polymer materials. Building on these premises, a compromise during the selection of composite materials may be required to achieve the desired bearing properties, such as the high load capacity or low power losses.

As a plain bearing material, composites have several advantages when compared to the traditionally used bronze alloys [8]: higher chemical resistance, lower wear rate, vibration damping, and lower weight. For that reason, there has been a steady rise in composite use for plain bearing manufacturing. It should be noted that the composites used as plain bearing materials are thermal insulators, meaning that an increase in the working temperature will be higher. Moreover, to better understand the overall performance and limitations of the composite plain

\*Corr. Author's Address: University of Zagreb, Faculty of Mechanical Engineering and Naval Architecture, Ivana Lučića 5, 10002 Zagreb, Croatia, stanko.skec@fsb.hr

bearings, most of the current research efforts are focused on the analysis of tribological properties [9] and [10], the optimization of design itself [11] and [12], application of novel materials and coatings [13] and [14], or studying the lubrication models [15].

Generally, the research on tribological properties includes studying the adhesion, friction, wear, and lubrication of surfaces in contact [16]. The tribological properties of the composite materials such as the friction coefficient and wear rate can be improved by altering the orientation, volume fraction, and shape of the reinforcements. For example, El-Sayed et al. [17] found that, for the observed composite material, the lowest friction coefficient is achieved using either transversal or longitudinal fibre orientation. Moreover, increased volume fraction was found to have a beneficial effect on both the wear rate and friction coefficient. By varying the whisker aspect ratios, Ji et al. [18] determined whether the reinforcement shape affects the frictional and wear properties of the composite. Whiskers with lower aspect ratios resulted in more stable mechanical properties. Masripan et al. [19] studied the effect of hardness on a plain bearing's tribological properties. The authors concluded that using the hardest test specimen will result in the lowest friction and, consequently, the lowest wear. The design can be enhanced by altering the microgeometry; with surface texturing being one of the methods. Rahmani and Rahnejat [12] used analytical methods to optimize texture geometry of composite reinforcements. Orientation and layout of the surface fibre were varied to increase the load capacity.

When aiming to improve the performance of a bearing-shaft system, in addition to the design and material selection, the use of lubricant is essential. It reduces the friction and material wear in plain bearings and, consequently, improves their efficiency and service life [20]. The lubricants can be either liquid (greases, oils), solid or gaseous. In composite materials with a polymer matrix, lubricants can be impregnated into the matrix, or the running can be dry (no lubricant). This research study is focused on solid lubricants, which are most often used when a continuous adherent film is required in the rubbing surfaces [21], a case encountered in plain bearings. The key advantage to solid lubricants in bearing design is simplicity; there is no need for a lubricating system. Additionally, they ensure uniform friction coefficient and increased permissible contact stresses at the cost of a limited lifetime and modest heat dissipation properties [22]. For lubrication of polymer materials the diamond-like carbon (DLC), polytetrafluoroethylene (PTFE), and MoS<sub>2</sub> are the

most widely used solid lubricants, with PTFE often described as promising [23].

For the dry running specimen, Rezaei et al. [4] conducted an experimental study using the oscillatory motion, often found in mechanical joints. The clearance was found to have a significant impact on the contact stress distribution. No further studies considering the influence of clearance on dry running plain bearings were found.

For this reason, in this article, the authors investigated whether the clearance has an influence on friction coefficient and wear in plain bearings operating at constant rotational speed, as found in mechanical transmissions. The rotational shaft movement was used instead of the oscillatory one to more precisely simulate a bearing-shaft system [4].

## 1 METHODS

The main goal of this experimental study was to determine how the clearance affects the friction coefficient between the bearing and shaft, and the wear of the composite bearing itself. The experimental rig is described in Section 2, while the variables of interest and associated levels are given in Section 2.1.

The plain bearing specimens made of NORDEN Marine 605 composite are coupled with the shaft made of AISI 316. The composite consists of a thermosetting resin reinforced with synthetic fabric and impregnated with solid lubricants to enhance the dry running capabilities. As such, it is an orthotropic material. Its mechanical properties are shown in Table 1. Additional manufacturer-provided data that includes the composite material specifications, machining recommendations, and handling information can be found in [24].

The influence of clearance on the composite plain bearing performance regarding the bearing efficiency and durability was assessed for both the dry running and lubricated specimens. Solid lubricants were applied instead of the liquid ones to avoid the swelling of the polymer matrix. Within the study, polymer swelling is undesirable since it affects the clearances that must remain the same during the test run. PTFE was selected as a lubricant due to its tribological properties (low friction) and convenient application.

The conducted study is based on the approach used by Rezaei et al. [4], who studied the clearance influence on the contact stresses in polymeric composite journal bearings. Rezaei et al. conducted an experiment using two different bearings, each having a different vertical load, clearance, and width. PTFE filler was used as a lubricant in both bearings.

In this research study, a full factorial experimental design was used (more details in Section 2.2). Two lubrication types were combined with two load and four clearance levels, resulting in a total of 16 required measurements per replication. Three replications were made for each specimen to obtain statistically relevant data. Each measurement lasted 120 minutes to avoid the transitional phenomena, thus ensuring the robustness of results. Level selection is explained in Section 2.1.

**Table 1.** NORDEN Marine 605 mechanical properties [24]

Property	
Maximum tensile strength [N/mm <sup>2</sup> ]	60
Maximum safe static load [N/mm <sup>2</sup> ]	110
Maximum safe dynamic load [N/mm <sup>2</sup> ]	55
Density [kg/m <sup>3</sup> ]	1300
Maximum water swell [%]	0.15
Maximum working temperature [°C]	100

## 2 EXPERIMENTAL

The experimental rig was created to emulate the working conditions, and the loads plain bearings have to endure during their working life (Fig. 1). The rig enables the adjustment of bearing load  $F_w$  by using weights, which are attached to the ball bearing to keep a constant orientation of load vector. The ball bearing is fitted on the outer side of the plain bearing housing, as shown in Fig. 1. The torque  $T$  used to overcome the frictional losses is provided by an alternating current (AC) electric motor and is measured using the torque meter. The torque meter of accuracy class 0.2 and a nominal torque of 20 Nm was used. A plain bearing is mounted in the housing using the press fit.

The shaft diameter is 34 mm. During the experiment, the rotational speed of the shaft is constant. The rotation causes relative movement between the static plain bearing and the shaft. At the end of the upper rig arm, a load cell (accuracy class 0.2, a nominal force of 500 N) is mounted to enable the measurement of force  $F_m$ . Sensors were connected to the data acquisition unit operating using professional software.

The rig geometry is defined as follows; the distance  $L = 150$  mm is the distance between the shaft axis and the load cell. An increase in length  $L$  enables the use of a lower capacity load cell, the advantage of which is higher test rig accuracy, as the cell sensitivity is specified as a percentage of the maximum capacity.

Due to a higher thermal expansion coefficient of the polymer matrix composites, an increase in

temperature will result in a larger decrease in the clearance, when compared to the steel parts. A thermometer has been installed to keep track of the change in temperature, which causes thermal expansion. The highest temperature is expected in the contact zone between the bearing and shaft, where it cannot be measured directly. For this reason, the thermometer beam is focused on the plain bearing side, near the contact point. The contactless thermometer (declared accuracy of  $\pm 1\%$ ) was used to measure the plain bearing temperature  $\vartheta$ . The disadvantages of using the above-described method to determine the polymer temperature are shown in [25].

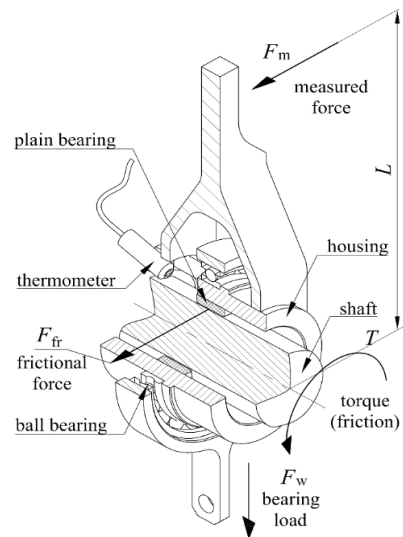


**Fig. 1.** Experimental rig

### 2.1 Experimental Variables

Preliminary variable analysis and selection were necessary due to a limited number of runs. The experimental variables can be divided into three groups: independent variables, dependent variables, and control variables. Independent variables serve as input and are manipulated to determine their influence on the dependent variables, which is measured throughout the experiment, while the control variables remain unchanged to prevent them from affecting the results. Influences of the following independent variables were considered in this experimental study:

**Clearance** - the primary aim of the study was to conclude whether the clearance influences the plain bearing friction and wear. The clearance size  $S$ , defined as the difference between the internal bearing and shaft diameter, was varied. Bearings were made with bore widths of 34.15 mm, 34.25 mm, 34.5 mm,

and 34.9 mm, resulting in clearances of 0.15 mm, 0.25 mm, 0.5 mm and 0.9 mm respectively. To diminish the influence of manufacturing error on the experimental results, specimens were measured before the experiment. An internal micrometer with a precision of 0.001 mm was used.

**Bearing load** – is equal to the radial force applied to the bearing through the shaft. It is included as an independent variable since, at both ends of the load spectrum (light and heavy loads), load effect on the friction coefficient was found. The former was presented by Myshkin et al. [26] in a review article, in which an overview of research articles studying load influence on friction in various polymers was shown, mostly using the ball-on-disc method. For light loads, the friction decreases as the load increases, while the opposite is correct for the heavy loads [27]. Since the Norden Maritim 605 has a polymer matrix, results are relevant to the case observed in the study at hand. To account for bearing load ( $F_w$ ) influence, two load levels were used. A load of 65 N was chosen to represent the regular working load, while 115 N represents the higher end of the load spectrum.

**Lubrication** – the lubricant is used to reduce the friction coefficient between the two parts in relative motion and as such influences the friction coefficient. Thus, the two lubrication types were included as independent variables; the dry running specimens were compared to specimens lubricated using a solid lubricant, PTFE. It should be emphasized that the lack of oil film in solid lubrication eases the thermometer beam focusing.

The following dependent variables were measured or calculated during the experiment:

**Friction coefficient** – is one of the key factors for assessing the efficiency of a power transmission [28]; reducing the friction coefficient will result in lower power losses. The defined test rig geometry (moment arm lengths  $L$  and  $r$ ) and the known forces  $F_m$  and  $F_w$  enable the friction coefficient calculation using Eq. (1), as follows:

$$\mu = \frac{F_m \cdot L}{F_w \cdot r}, \quad (1)$$

where  $F_m$  [N] is the load cell measured load;  $L$  [mm] the distance between the shaft axis and the load cell;  $r$  [mm] the inner plain bearing radius, and  $F_w$  [N] the applied weight.

**Temperature** – is known to affect the friction coefficient between the parts [26]. Moreover, an increase in the temperature causes thermal expansion, reducing the previously measured clearances. The

low thermal conductivity of the matrix should also be noted, as the expected contact temperature could be higher than the measured one. To enable the assessment of thermal influence on the friction coefficient, it is selected as a dependent variable and tracked throughout the experiment. As described in Section 2, a contactless thermometer was used to measure the change in temperature close to the point of contact. By keeping track of the changes in temperature, it is possible to determine the magnitude of thermal expansion.

**Wear** – to determine the influence of the clearance on composite plain bearing wear, specimens were weighed before and after the experiment [29]:

$$\Delta m = m_{\text{initial}} - m_{\text{final}}, \quad (2)$$

where  $m_{\text{initial}}$  [mg] and  $m_{\text{final}}$  [mg] are bearing masses before and after the experimental run, respectively. The digital scale with an accuracy of 0.001 g was used to weigh the specimens. The PTFE-lubricated specimens were weighed before and after lubrication.

**Surface roughness** – although the influence of surface roughness on the friction coefficient exists, as demonstrated in [30], it was not considered in this study. However, mean surface roughness was measured before and after the experiment to keep track of the smoothing effect. All the specimens were to be manufactured with the equal mean surface roughness of  $Ra = 3.2 \mu\text{m}$ . Its values are measured in the axial direction before and after the experiment to provide data for possible future studies. The authors used a roughness tester with a resolution of  $0.002 \mu\text{m}$  at a  $25 \mu\text{m}$  range.

Lastly, the following variables were chosen as constants:

**Sliding velocity** – the sliding velocity influences both the friction and wear [8], but was not considered within this research study. According to Myshkin, et al. [26], for insignificant variations in contact temperature, independence of friction coefficient in relation to the sliding velocity can be assumed. The sliding velocity  $v_s = 0.53 \text{ m/s}$  was selected for all the specimens. Temperature measurements were used for the validation of the sliding velocity simplification procedure.

**Bearing width** – plain bearing width was 27 mm for all test specimens.

**Outer bearing diameter** – a value of 39 mm was used for all the test specimens.

## 2.2 Design of Experiment

The experiment was organized as full factorial since it was difficult to predict the possible interactions between variables, and whether there are saddle points within the interval at hand. The clearance size, lubrication, and bearing load selected as independent variables (see Fig. 2). Additionally, measurements were replicated twice to increase the reliability, resulting in a total of 48 experimental runs.

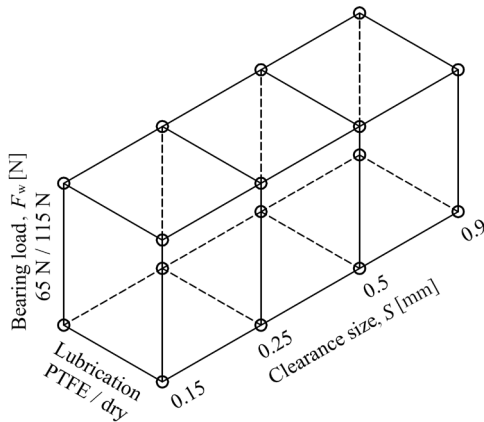


Fig. 2. Design of experiment schema

The clearances between the shaft and the bearings were measured to determine the scale of manufacturing error (see Table 2).

Table 2. Clearances

Lubrication	Bearing load, $F_w$ [N]	Theoretical clearance $S_{th}$ [mm]	Measured clearance $S$ , [mm]			
			I	II	III	
Dry running	65	0.15	0.128	0.13	0.133	
		0.25	0.224	0.235	0.243	
		0.5	0.511	0.52	0.562	
		0.9	0.866	0.872	0.882	
	115	0.15	0.145	0.17	0.19	
		0.25	0.224	0.241	0.246	
		0.5	0.532	0.535	0.541	
		0.9	0.91	0.918	0.919	
	Solid lubricant (PTFE)	65	0.15	0.145	0.147	0.147
			0.25	0.241	0.242	0.243
			0.5	0.532	0.535	0.536
			0.9	0.917	0.918	0.93
115		0.15	0.165	0.168	0.186	
		0.25	0.251	0.253	0.282	
		0.5	0.505	0.55	0.58	
		0.9	0.925	0.935	0.94	

## 3 RESULTS

A total of 48 measurements have been carried out. All the specimens were inspected after the experiment to avoid erroneous measurements. The inspection procedure consisted of disassembling the experimental rig and removing the test specimen, which was then cleaned using the solvent cleaner. After the cleaning, visual inspection using a magnification lens was carried out. During the visual inspection, the focus was on detecting failure modes caused by the manufacturing process or inaccurate assembly (i.e. uneven wear). Failure modes that develop slowly, such as corrosion or fatigue failure were not considered since the experiment lasted for only 120 minutes. Uneven wear was the only defect the authors detected within the study. The authors assume that it was caused by a misalignment of the plain bearing and shaft axes. For all the specimens where a defect was detected, a measurement was repeated.

The relation between the friction coefficient, the plain bearing temperature, and the clearance is shown in Fig. 3 (for additional plots see Appendix, Fig. 7). Dry running specimens displayed inconclusive results; trends were not consistent for loads of 65 N and 115 N. In the former, greater clearance caused a decline in the friction coefficient. Measurements on clearances of 0.25 mm and 0.5 mm found no significant difference in friction coefficient. For the load of 115 N, friction coefficients displayed a different trend. The lowest friction coefficient  $\mu = 0.184$  was found at the 0.15 mm clearance, followed by  $\mu = 0.192$  at the 0.9 mm clearance. In PTFE-lubricated specimens, results are consistent for both load levels. The highest friction coefficient was found at the clearance of 0.15 mm. With the increase in clearance, up to 0.5 mm, the friction coefficient was reduced. The change was more prominent for the higher load level; the lowest friction coefficient values were measured for clearance of 0.5 mm. Further increase in the clearances resulted in an increased friction coefficient. Lastly, when compared to the PTFE-lubricated specimens, the calculated friction coefficients were higher for the dry running specimens.

As shown in Fig. 3, changes in the measured temperatures are related to the changes in friction coefficient. The relationship is the most prominent for dry running specimens under the load of 65 N. The exceptions were 0.15 mm clearances, for which no relation with the friction coefficient was found. The largest deviations were found in dry running specimens loaded with 65 N and the lubricated specimen loaded with 115 N. Dry running specimens displayed similar

behaviour at both load levels except for 0.15 mm clearance. Increase in the clearances resulted in minor decreases in the temperatures. For the PTFE-lubricated specimens, the highest temperatures were measured at the clearance of 0.15 mm. Increases in clearance resulted in lower temperatures up to clearance of 0.5 mm; the lowest temperature was measured for both load levels. Further increase in clearance resulted in increased temperature. On average, the difference in measured temperature between the dry running and PTFE-lubricated specimens was 4.26 °C at the load level of 65 N, and 4.35 °C at 115 N. When comparing the load level influence on the temperatures, the average difference in temperature between the 115 N and 65 N load was 7 °C for dry running and 6.7 °C for PTFE-lubricated specimens.

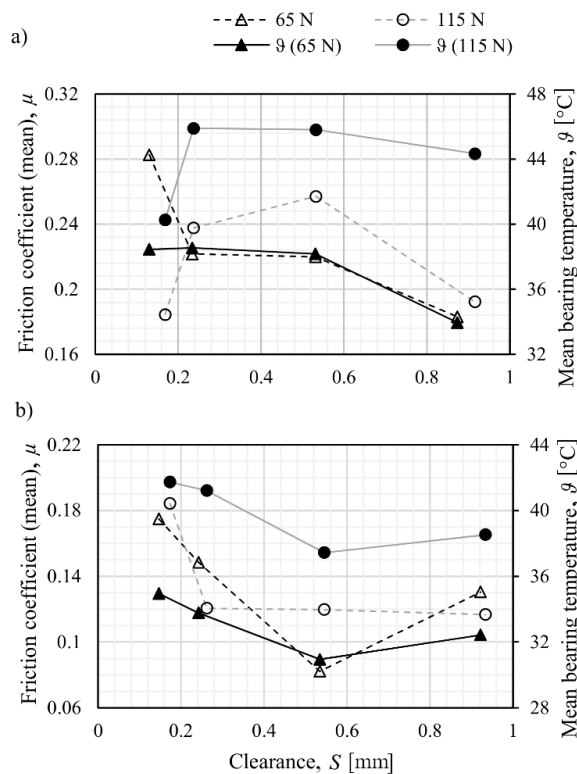


Fig. 3. Influence of clearance on a friction coefficient and temperature a) dry running and b) PTFE-lubricated

The weighing of specimens has shown that clearance has an impact on bearing wear (Fig. 4). By using the experiment data, the average mass loss was calculated for each test condition. As expected, higher wear is measured in dry running specimens at both load levels; on average, usage of the PTFE lubricant reduced the lost material mass by 1 mg for 65 N and 0.66 mg for 115 N load. The lowest wear was found in

0.5 mm clearance bearings for both lubrication regimes and load levels. When compared to 0.9 mm clearance, using 0.15 mm and 0.25 mm clearances causes a more prominent increase in wear. When comparing the influence of load levels, dry running specimens displayed inconclusive results. For clearance of 0.15 mm, lower load resulted in lower wear, while for the 0.25 mm and 0.5 mm clearances higher load coincided with the lower wear. At the 0.9 mm clearance, average mass losses due to wear were equal. The behaviour observed in PTFE-lubricated specimens was similar; at clearances of 0.15 mm and 0.5 mm, lower wear was recorded for 65 N load, in contrast to 0.25 mm and 0.9 mm clearances, which favoured the higher load. As noted in Section 2.1, mean surface roughness was measured both before and after the experiment. For the dry running specimens, the average change in mean surface roughness was 0.87 μm at 65 N, and 0.89 μm at 115 N. Lubricated specimens displayed greater smoothing effect; average change in mean surface roughness was 1.56 μm at a load of 65 N and 1.28 μm at 115 N.

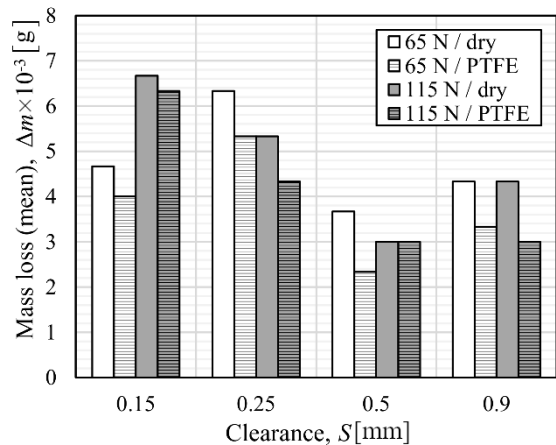


Fig. 4. Bearing mass loss for different clearances

#### 4 DISCUSSION

In plain bearings working under constant rotational speed, the clearance size affects the friction coefficient, differing from the results for oscillating movement presented in [4]. For example, at 65 N loads, the lowest friction coefficient was measured for 0.5 mm clearance. In the vicinity of that value lays the optimal clearance for a corresponding set of selected parameters. By either increasing or decreasing the clearance, the friction coefficient increases.

Lowering the clearance size results in an increase in the friction coefficient, thus increasing

the risk of bearing failure. The former statement was validated by repeating the experiment for the bearings with clearances of 0.05 mm (Fig. 5). Each test run, regardless of load level and lubrication regime, resulted in bearing seizure within the first hour. The average friction coefficients for the duration of the experiment were ranging from 0.782 to 0.819 for dry running and from 0.636 to 0.65 for PTFE-lubricated specimens. Similar results were reported by Brockwell and DeCamillo in [31], where a small decrease in clearance size resulted in a steep increase of the temperature, restricting the rotational velocities.

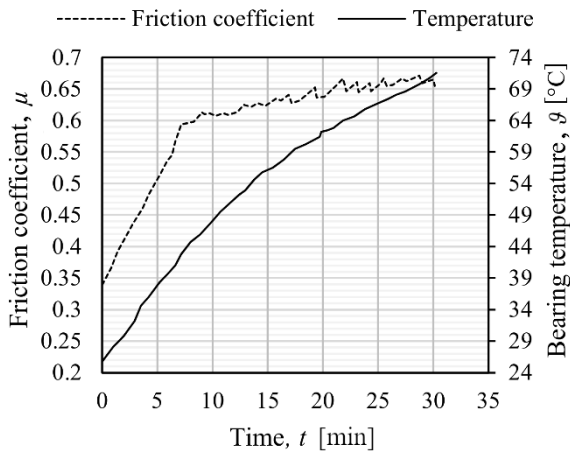


Fig. 5. Results for PTFE-lubricated specimen (115 N)

On the other side of the spectrum, for the dry running specimens, the increase in clearance size resulted in a lower friction coefficient. In PTFE-lubricated specimens, however, larger clearance sizes also resulted in higher friction coefficients. With an increase in clearance size, contact surface decreased, causing the contact pressure to rise. Using the procedure presented in [32], in specimens loaded with 65 N contact pressure of 0.8 MPa was calculated for 0.15 mm, and 1.9 MPa for 0.9 mm clearance. At a higher load level, values were 1 MPa and 2.5 MPa, respectively. It should be added that a study carried out by Domitran, et al. [25], in which the authors used polyethylene (PET) samples with the addition of PTFE, has shown that an increase in contact pressure also increased the friction coefficient. Building on these premises, an increase in contact pressure could affect the increase in friction coefficient in lower clearance sizes. When assessing the relationship between the bearing load and friction coefficient, higher friction coefficients were calculated for higher loads, regardless of the lubrication regime.

Furthermore, the friction coefficient trendlines in dry running specimens had a similar shape for

65 N and 115 N loads. The same was found in PTFE-lubricated specimens. Exceptions to former statements were the dry running specimens with 0.15 mm clearance and PTFE-lubricated specimens with 0.25 mm clearance. The differences regarding the lubrication regime were also noted. In dry running specimens, the lower friction coefficient was achieved by increasing the clearance size. For PTFE-lubricated specimens, optimal clearance must be found. The optimal clearance will be a trade-off between the seizure at the low clearance sizes and an increase in contact pressure in higher clearance sizes.

The clearance affects the temperature of bearing near the contact point (Fig. 5). However, those changes are low; the largest difference in temperature  $\Delta\theta_{\max} = 5.6$  °C was measured for bearings operating at 115 N load with no lubricant. Accordingly, as the  $\Delta\theta_{\max}$  is rather low and comparable to the fluctuations in the ambient temperature, the assumption regarding the use of constant sliding velocity is valid (see Section 2.1, [26]). The bearing load was also shown to affect the bearing temperature. In specimens loaded with 65 N loads, changes in clearance size resulted in a linear relationship between the friction coefficients and measured bearing temperature (Fig. 6). It was more prominent in PTFE-lubricated specimens, likely due to a more uniform surface resulting from the application of solid lubricant. No distinct trends were noted for the specimens operating under a heavier load. The lower friction coefficient results in a lower frictional force, which in turn reduces the amount of heat transferred to the bearing and its wear. Consequently, the lower temperature was measured in PTFE-lubricated specimens. By further increasing the clearance size to 0.9 mm, the temperature started to increase. For the dry running specimens, the bearing temperature decreased with the increase in clearance.

The lowest mass loss was measured for 0.5 mm clearances, which proved to be optimal regarding the wear for all the specimens. Furthermore, with the increase of clearance size from 0.15 mm to 0.5 mm, mass loss in specimens working under 115 N load decreased, after which it rose at a clearance of 0.9 mm. The similar behaviour was observed in the friction coefficient. For loads of 65 N, highest wear was found in 0.25 mm clearances. It was also observed that, contrary to the higher load level, specimens working at 65 N load have multiple local minima, suggesting the need for including additional clearance size levels in the future studies.

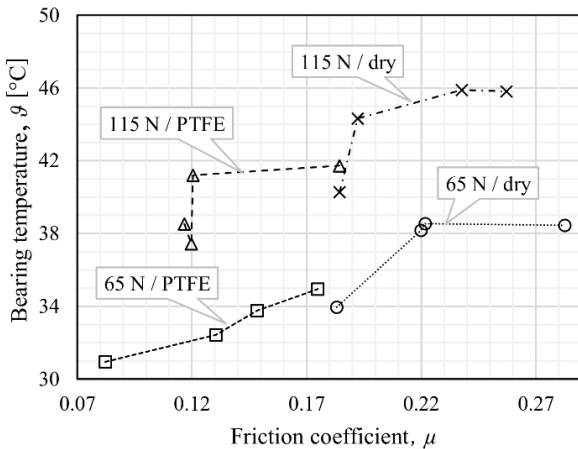


Fig. 6. Relationship between the friction coefficient and bearing temperature (not sequenced by the clearance)

Similarly to the friction coefficient and temperature, the higher load caused more intensive wear. The larger frictional force, caused by higher friction coefficient and normal load, resulted in more intensive bearing wear. Thus, it was expected that a mass loss will increase as the friction coefficient increases. However, the experimental results were not in agreement with the former statement; even though the increase in wear is expected as the load level rises [33], no consistency in mass loss depending on the load was found. The use of lubricant resulted in lower wear for all the clearances and load levels, as expected. The mass loss reduction was lower for the higher bearing load. When considering the surface roughness, even though the lowest average values were found in 0.5 mm clearance specimens, differences were rather modest. No bearing load impact was observed as the lowest change was recorded in the dry running specimens at 65 N load.

## 5 CONCLUSIONS

The study of the influence of clearance on the friction coefficient and wear in composite plain bearings has been carried out. A total of 48 experimental measurements have been conducted. The performances of composite plain bearings manufactured with different clearances were observed under two levels of load and two different lubrication regimes; dry running and solid lubricant applied (PTFE). Not accounting for the manufacturing error, four different clearances were observed.

The results have shown that the friction coefficient is affected by clearance. For the dry running specimens, the results have shown that

the friction coefficient reduces as the clearance size is increased. In PTFE-lubricated specimens, the optimum must be found, as the local friction coefficient minimum was found inside the observed clearance size interval. When considering the bearing temperature, in specimens tested under the 65 N loads, the linear relation between the friction coefficient and the bearing temperature was found. The relation between the temperature and friction coefficient was found only at the lower load level (65 N), while no general trends were observed for the wear and surface roughness change.

Even though the study has shown that clearance affects the friction coefficient, temperature, and wear in dry running and PTFE-lubricated specimens, initial results point out that the further work is required to determine its optimal values. By decreasing the interval between the different clearance size levels, the optimal solution could be found. Increase of a number of clearance size levels could mitigate the possible saddle points found when observing wear.

## 6 ACKNOWLEDGEMENTS

This paper reports on work funded by the Croatian Science Foundation project IP-2018-01-7269: Team Adaptability for Innovation-Oriented Product Development (TAIDE).

## 7 NOMENCLATURES

$b$	bearing width, [mm]
$F_m$	measured force, [N]
$F_w$	bearing load, [N]
$F_{fr}$	frictional force, [N]
$L$	distance between the load cell and shaft axis, [mm]
$\Delta m$	plain bearing mass loss, [g]
$r$	inner bearing radius, [mm]
$\Delta Ra$	difference between the initial and final mean surface roughness, [ $\mu\text{m}$ ]
$S$	clearance between the plain bearing and the shaft, [mm]
$T$	motor-provided torque, [Nm]
$v_s$	sliding velocity, [m/s]
$\theta$	bearing temperature, [ $^{\circ}\text{C}$ ]
$\mu$	friction coefficient, [-]

## 8 REFERENCES

- [1] Hirani, H., Suh, N.P. (2005). Journal bearing design using multiobjective genetic algorithm and axiomatic design approaches. *Tribology International*, vol. 38, no. 5, p. 481-491, DOI:10.1016/j.triboint.2004.10.008.
- [2] Schmidt, A.A., Schmidt, T., Grabherr, O., Bartel, D. (2018). Transient wear simulation based on three-dimensional finite element analysis for a dry running tilted shaft-bushing bearing. *Wear*, vol. 408-409, p. 171-179, DOI:10.1016/j.wear.2018.05.008.
- [3] Shinde, A.B., Pawar, P.M. (2017). Multi-objective optimization of surface textured journal bearing by Taguchi based Grey relational analysis. *Tribology International*, vol. 114, p. 349-357, DOI:10.1016/j.triboint.2017.04.041.
- [4] Rezaei, Van Paepegem, W., Ost, W., De Baets, P., Degrieck, J. (2012). A study on the effect of the clearance on the contact stresses and kinematics of polymeric composite journal bearings under reciprocating sliding conditions. *Tribology International*, vol. 48, p. 8-14, DOI:10.1016/j.triboint.2011.06.031.
- [5] Prehn, R., Hauptert, F., Friedrich, K. (2005). Sliding wear performance of polymer composites under abrasive and water lubricated conditions for pump applications. *Wear*, vol. 259, no 1-6, p. 693-696, DOI:10.1016/j.wear.2005.02.054.
- [6] Chen, B., Wang, J., Yan, F. (2012). Comparative investigation on the tribological behaviors of CF/PEEK composites under sea water lubrication. *Tribology International*, vol. 52, p. 170-177, DOI:10.1016/j.triboint.2012.03.017.
- [7] VDI 2736-2:2014. *Thermoplastic Gear Wheels - Cylindrical Gears - Calculation of The Load-Carrying Capacity*, Verlag des Vereins Deutscher Ingenieure, Düsseldorf.
- [8] Opalić, M., Domitran, Z., Katana, B. (2014). Comparison of Antifriiction Properties of Polymer Composites and Bronze. *Tehnički Vjesnik - Technical Gazette*, vol. 21, no. 5, p. 1089-1095.
- [9] Eliezer, Z., Khanna, V.D., Amateau, M.F. (1978). Wear mechanism in composites: a qualitative model. *Wear*, vol. 51, no. 1, p. 169-179, DOI:10.1016/0043-1648(78)90064-9.
- [10] Rezaei, Van Paepegem, W., De Baets, P., Ost, W., Degrieck, J. (2012). Adaptive finite element simulation of wear evolution in radial sliding bearings. *Wear*, vol. 296, no. 1-2, p. 660-671, DOI:10.1016/j.wear.2012.08.013.
- [11] Etsion, I., Burstein, L. (1996). A model for mechanical seals with regular microsurface structure. *Tribology Transactions*, vol. 39, no. 3, p. 677-683, DOI:10.1080/10402009608983582.
- [12] Rahmani, R., Rahnejat, H. (2018). Enhanced performance of optimised partially textured load bearing surfaces. *Tribology International*, vol. 117, p. 272-282, DOI:10.1016/j.triboint.2017.09.011.
- [13] Maksimkin, A.V., Danilov, V.D., Senatov, F.S., Olifirov, L.K., Kaloshkin, S.D. (2017). Wear performance of bulk oriented nanocomposites UHMWPE/FMWCNT and metal-polymer composite sliding bearings. *Wear*, vol. 392-393, p. 167-173, DOI:10.1016/j.wear.2017.09.025.
- [14] Wang, Y., Yin, Z., Li, H., Gao, G., Zhang, X. (2017). Friction and wear characteristics of ultrahigh molecular weight polyethylene (UHMWPE) composites containing glass fibers and carbon fibers under dry and water-lubricated conditions. *Wear*, vol. 380-381, p. 42-51, DOI:10.1016/j.wear.2017.03.006.
- [15] Andersson, S., Söderberg, A. Björklund, S. (2007). Friction models for sliding dry, boundary and mixed lubricated contacts. *Tribology International*, vol., 40, no. 4, p. 580-587, DOI:10.1016/j.triboint.2005.11.014.
- [16] Buckley, D.H. (1978). Tribological properties of surfaces. *Thin Solid Films*, vol. 53, no. 3, p. 271-283, DOI:10.1016/0040-6090(78)90221-3.
- [17] El-Sayed, A.A., El-Sherbiny, M.G., Abo-El-Ezz, A.S., Aggag, G.A. (1995). Friction and wear properties of polymeric composite materials for bearing applications. *Wear*, vol. 184, no. 1, p. 45-53, DOI:10.1016/0043-1648(94)06546-2.
- [18] Ji, Z., Luo, W., Zhou, K., Hou, S., Zhang, Q., Li, J., Jin, H. (2018). Effects of the shapes and dimensions of mullite whisker on the friction and wear behaviors of resin-based friction materials. *Wear*, vol. 406-407, p. 118-125, DOI:10.1016/0043-1648(94)06546-2.
- [19] Bin Masripan, N.A., Ohara, K., Umehara, N., Kousaka, H., Tokoroyama, T., Inami, S., Zushi, K., Fujita, M. (2013). Hardness effect of DLC on tribological properties for sliding bearing under boundary lubrication condition in additive-free mineral base oil. *Tribology International*, vol. 65, p. 265-269, DOI:10.1016/j.triboint.2013.01.016.
- [20] Qiu, M., Chen, L., Yingchun, Li., Yan, J. (2017). *Bearing Tribology - Principles and Applications*. Springer Nature, Berlin.
- [21] Street, K.W., Miyoshi, K., Vander Wal, R.L. (2007). Application of carbon based nano-materials to aeronautics and space lubrication. Erdemir, A., Martin, J.-M. (Eds.), *Superlubricity*. NASA, Cleveland, p. 311-340, DOI:10.1016/b978-0-44452772-1/50050-0.
- [22] Katana, B. (2017). Life time of composite bearing (doctoral thesis), University of Zagreb, Zagreb.
- [23] Bijwe, J., Sen, S., Ghosh, A. (2005). Influence of PTFE content in PEEK-PTFE blends on mechanical properties and tribo-performance in various wear modes. *Wear*, vol. 258, p. 1536-1542, DOI:10.1016/j.wear.2004.10.008.
- [24] Norden Maritim. Marine Engineering Manual Rudder Bearing Design Guide, from <https://www.nordenmaritim.no/>, accessed on 2019-09-09.
- [25] Domitran, Z., Žeželj, D., Katana, B. (2016). Influence of contact pressure and sliding speed on the temperature and coefficient of friction in sliding contact between two PET samples. *Tehnički Vjesnik - Technical Gazette*, vol. 23, no. 2, p. 389-396, DOI:10.17559/TV-20151124163215.
- [26] Myshkin, N.K., Petrokovets, M.I., Kovalev, A.V. (2005). Tribology of polymers: Adhesion, friction, wear, and mass-transfer. *Tribology International*, vol. 38, no. 11-12, p. 910-921, DOI:10.1016/j.triboint.2005.07.016.
- [27] Shooter, K.V., Tabor, D. (1952). The Frictional Properties of Plastics. *Proceedings of the Physical Society, Section B*, vol. 65, p. 661-671, DOI:10.1088/0370-1301/65/9/302.
- [28] Michaelis, K., Höhn, B., Hinterstoißer, M. (2011). Influence factors on gearbox power loss. *Industrial Lubrication and Tribology*, vol. 63, no. 1, p. 46-55, DOI:10.1108/00368791111101830.

[29] Lin, L., Ecke, N., Kamerling, S., Sun, C., Wang, H., Song, X., Wang, K., Zhao, S., Zhang, J., Schlarb, A.K. (2018). Study on the impact of graphene and cellulose nanocrystal on the friction and wear properties of SBR/NR composites under dry sliding conditions. *Wear*, vol. 414-415, p. 43-49, DOI:10.1016/j.wear.2018.07.027.

[30] Saxena, P., Schinzel, M., Andrich, M., Modler, N. (2016). Development of a novel test-setup for identifying the frictional characteristics of carbon fibre reinforced polymer composites at high surface pressure. *IOP Conference Series Materials Science and Engineering*, vol. 149, p. 012124, DOI:10.1088/1757-899X/149/1/012124.

[31] Brockwell, K., DeCamillo, S. (1997). Performance Evaluation of the LEG tilting pad journal bearing, from [www.kingsbury.com](http://www.kingsbury.com), accessed on 2019-09-09.

[32] Budynas, R., Nisbett, K. (2007). *Shigley's Mechanical Engineering Design*, McGraw-Hill, New York.

[33] Mao, K. (2007). A new approach for polymer composite gear design. *Wear*, vol. 262, no. 3-4, p. 432-441, DOI:10.1016/j.wear.2006.06.005.

9 APPENDIX

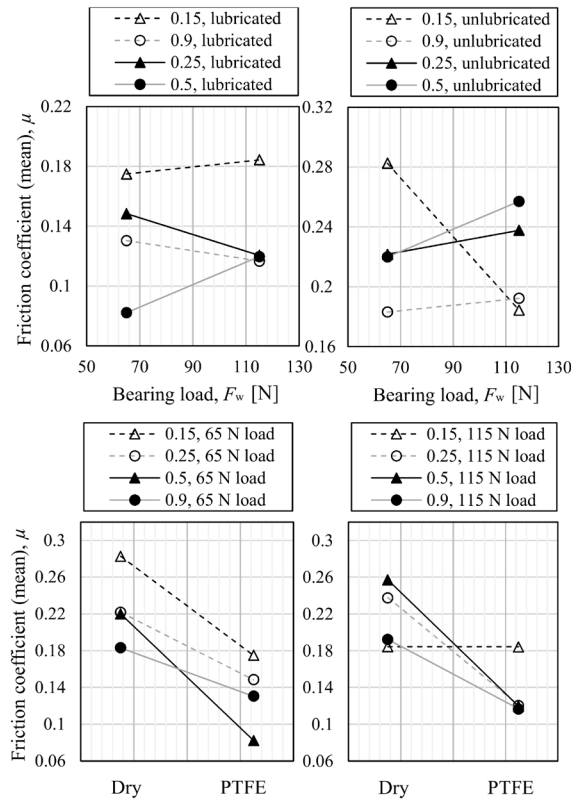


Fig. 7. Mean effect plot

# Analysis of EDM Process Parameters on Inconel 718 Using the Grey-Taguchi and Topsis Methods

Thangavel Yuvaraj\* – Paramasivam Suresh

Muthayammal Engineering College (Autonomous) Rasipuram, Department of Mechanical Engineering, India

Nickel-based superalloys are gaining importance for their growing usage in aerospace industries. Amidst the various advanced machining processes, electro discharge machining (EDM) is considered to be an important one for its ability to machine materials irrespective of its intrinsic properties. In this study, Inconel 718 is considered as a work material, and an  $L_{18}$  orthogonal array (OA) experimental plan is utilized to machine the work material. The influential factors, which affect the EDM performance characteristics, are identified using analysis of variance (ANOVA). Not much work has been done regarding using grey-Taguchi technique for order of preference by similarity to ideal solution (TOPSIS) methods, although these methods can be easily applied for multi-objective optimization. These methods provide the best results with the available sparse data. The best combination of machining factors is determined using grey-Taguchi and TOPSIS methods. Based on the conducted experiments, voltage (V) and pulse off-time ( $t_{off}$ ) show a notable contribution on output performance. The optimal combination of input parameter through grey-Taguchi is found to be 10 A, 30 V, 200  $\mu$ s, and 20  $\mu$ s respectively, for the EDM parameters: current (I), V, pulse on-time ( $t_{on}$ ) and  $t_{off}$  for improved response. Moreover, the best parameter setting (I = 10 A, V = 30 V,  $t_{on}$  = 100  $\mu$ s and  $t_{off}$  = 20  $\mu$ s) is identified using the TOPSIS method for the performance measures machining rate (MR), tool wear rate (TWR), overcut (OC), and taper overcut (TOC). Further tool wear behaviour is also studied through scanning electron microscope (SEM) images by varying the voltage.

**Keywords:** Inconel, ANOVA, grey-Taguchi, overcut, taper

## Highlights

- EDM process parameters (voltage, current, pulse on-time and pulse off-time) were optimized through the  $L_{18}$  orthogonal experimental design method, and the grey relational analysis (GRA) method, considering multi-responses, such as machining rate (MR), tool wear rate (TWR), overcut (OC), and taper overcut (TOC).
- The methods grey-Taguchi and TOPSIS were used to study the influential parameters that provide the best results with the available sparse data.
- Based on GRA and TOPSIS, the optimum level parameters for EDM have been identified. Furthermore, the tool wear behaviour is also studied through SEM images by varying the voltage.
- The optimal combination of the input parameter to acquire better responses based on grey-Taguchi has been found to be (10 A), V (30 V),  $t_{on}$  (200  $\mu$ s), and  $t_{off}$  (20  $\mu$ s). According to ANOVA, the voltage and  $t_{off}$  plays a prominent role in machining Inconel 718.
- The best combinations identified using the TOPSIS method for better performance measures is 10 A, 30 V, 100  $\mu$ s and 20  $\mu$ s.

## 0 INTRODUCTION

Electro discharge machining (EDM) has a one-off significant process for the machining of hard materials and superalloys. Heat-resistant superalloys (HRSA), especially the Inconel alloy, find applications in aerospace and marine components, cryogenic storage tanks, and nuclear reactor components. Understanding the importance of the Inconel alloy, manufacturing scientists and engineers are attempting to understand the behaviour of it through EDM processes. In the machining of Inconel 718, Shen et al. [1] applied high-speed EDM with air as a dielectric medium and produced components with better surface quality. The importance of powder-mixed dielectric fluid in the EDM for machining Inconel alloy was analysed by Talla et al. [2]. The researchers revealed better results for surface quality and accuracy while using

different powders, such as graphite, silicon, and aluminium [3] and [4]. Torres et al. [5] investigated the behaviour of an Inconel 600 alloy through EDM process. They studied the electrical parameters' influence and concluded that the change in polarity has a significant influence on surface quality. Tanjilul et al. [6] reported that a novel flushing method and a machining current significantly influences the debris removal. The size of the debris particles increases with increasing machining current. Rajesha et al. [7] studied the effect of process parameters such as current, duty cycle, sensitivity control, inter-electrode gap control, and flushing pressure on the material removal rate (MRR) and surface roughness (SR). They found that the pulse current and duty factor has the highest influence. Kuppan et al. [8] reported that the MRR and SR increase with the increase in peak current, duty factor, and electrode speed.

\*Corr. Author's Address: Department of Mechanical Engineering, Muthayammal Engineering College (Autonomous), Rasipuram, India, yuvarajt2019@gmail.com

Mohanty et al. [9] conducted an  $L_9$  orthogonal array (OA) and optimized the EDM process parameters of Inconel 825 using grey relational analysis (GRA). The parameters combination ( $I$  (1A),  $t_{on}$  (10  $\mu$ s), and duty cycle (75 %)) showed good results for the rate of material removed, surface quality, and radial overcut. Mohanty et al. [10] highlighted the importance of cryogenic treatment of tool in EDM on output performance using technique for order of preference by the similarity to ideal solution (TOPSIS) method and teaching-learning-based optimization algorithm. Dang [11] optimized the EDM parameters using a kriging model and particle swarm optimization method, finding that the model and method is suitable for the optimization of EDM process. Lin et al. [12] optimized and enhanced the EDM process parameters for Inconel 718 through multi-objective optimization technique using grey-Taguchi. Muthuramalingam and Mohan [13] machined SS 201 through EDM and established the importance of peak current. Lin et al. [14] conducted experiments on Ti-6Al-4V alloy through Micro-EDM and studied the influence of process parameters and gaps using the grey relational analysis (GRA)-Taguchi technique. The use of the GRA with Taguchi technique yields better results for tool electrode wear and overcut. Based on the above literature, the characteristics of EDM for machining holes on Inconel 718 are influenced by various input parameters. Each performance characteristic has different combinations of optimal process parameters and thus, in the case of multiple responses, the selections of optimal machining parameters are difficult. The grey system, proposed by Deng [15], handles the vague information and thus the GRA method is recommended as a principal method for multiple response optimisation. Therefore, researchers optimized the machining of Inconel 718 using electrical parameters and inter-electrode gap (IEG). In this paper, EDM process parameters:  $I$ ,  $V$ ,  $t_{on}$  and  $t_{off}$  were optimized through the  $L_{18}$  orthogonal experimental design method, and the GRA method considering multi-responses, such as machining rate (MR), tool wear rate (TWR), overcut (OC) and taper overcut (TOC). Not much work has been done using the grey-Taguchi and TOPSIS methods although these can be easily applied for multi-objective optimization. The significant contribution of this research is in using these methods to study the influential parameters that provide the best results with the available sparse data. Based on GRA and TOPSIS, the optimum level parameters for EDM have been identified. Furthermore, the tool wear behaviour is also studied

through scanning electron microscope (SEM) images by varying the voltage.

## 1 EXPERIMENTAL

The experimental set-up for EDM machining process is shown in Fig. 1. It consists of a maximum working voltage of 415 V, maximum current of 25 A, work table size of 600 mm  $\times$  400 mm, a maximum electrode length of 400 mm, and a servomotor for inter-electrode gap control. Inconel 718 has been selected as a workpiece material, whereas a brass electrode of  $\varnothing$  0.5 mm is used with EDM oil as the dielectric medium. Tables 1 and 2 provides the details of chemical and mechanical properties of Inconel 718 [16]. The thickness of workpiece is 3.1 mm. Since the discharge energy is primarily determined by current ( $I$ ), voltage ( $V$ ), pulse on-time ( $t_{on}$ ), and pulse off-time ( $t_{off}$ ), these factors are used as the input parameters. These parameters are selected based on the literature review, and levels are identified based the preliminary experiments; 10 A, 12 A and 14 A have been considered as current variables; 30 V, 40 V and 50 V have been chosen as voltage variables; 100  $\mu$ s, 150  $\mu$ s and 200  $\mu$ s have been chosen as  $t_{on}$  values with  $t_{off}$  values of 20  $\mu$ s, 30  $\mu$ s and 40  $\mu$ s. Table 3 shows the experimental layout using an  $L_{18}$  OA. MR is calculated by dividing the length of the through hole with the machining time required to complete the through hole. TWR is calculated using the relation mass is  $\rho \times v$ , where  $\rho$  is brass density,  $v$  volume of brass tool ( $\pi r^2 h$ ),  $h$  brass tool height. During the start and end of each

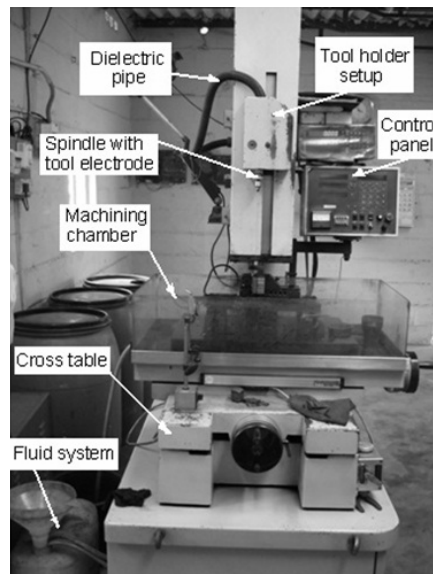


Fig. 1. Experimental setup

**Table 1.** Chemical composition of Inconel 718 (weight %)

C	Mn	Si	Cr	Ni	Co	Mo	Nb+Ta	Ti	Al	Fe
0.040	0.08	0.08	18.37	53.37	0.23	3.04	5.34	0.98	0.50	17.80

experiment, the length of the brass tool is measured, and the difference is noted as  $h$ ; this value is used to calculate the volume of brass electrode. The ratio of volume of electrode wear to the time taken to complete the experiment is called  $TWR$ .  $OC$  is calculated using optical microscopic images.  $OC$  is defined by  $\Delta R = Re - Rt$ , where  $Re$  is the entrance radius of the machined hole and  $Rt$  the tool electrode radius. The difference in  $Re$  and  $Rt$  results in  $OC$ .  $TOC$  is defined by  $TOC = D - d / (2L)$ , where,  $D$  is entry diameter of the machined hole,  $d$  exit diameter of the machined hole, and  $L$  thickness of the workpiece.

**Table 2.** Mechanical properties of Inconel 718

Hardness [HB]	Yield limits [MPa]	Tensile stress [MPa]
388	1375	1170

## 2 RESULTS

MR is the measure of machinability of the material. Hence, for a characteristic like  $MR$ , “larger-the-better”

is considered and the obtained  $MR$  data values are homogenized as shown below [14]:

$$x_j^*(i) = \frac{x_j(i) - \min x_j(i)}{\max x_j(i) - \min x_j(i)}, \quad (1)$$

where  $x_j^*(i)$  are the homogenized  $MR$  after the preprocessing, is the signal-to-noise ratio of the  $MR$ , where  $i=1$  for  $MR$ ;  $i=1, 2, 3, \dots, 18$  for experiments 1 to 18.

EDM performance is also measured using  $TWR$ ,  $OC$  and  $TOC$ . Hence, to achieve better machining quality, the “smaller-the-better” is considered in view of minimizing  $TWR$ ,  $OC$ , and  $TOC$ . Therefore the actual sequence must be normalized as follows [14]:

$$x_j^*(i) = \frac{\max x_j(i) - x_j(i)}{\max x_j(i) - \min x_j(i)}, \quad (2)$$

where  $x_0^*(i)$ ,  $\Delta_{0j}(i)$ ,  $x_j^*(i)$  are reference sequence, deviation sequence and comparability sequence, respectively.

$$\Delta_{0j}(i) = |x_0^*(i) - x_j^*(i)|. \quad (3)$$

**Table 3.**  $L_{18}$  orthogonal array

Experiment No.	Range of factors				Actual value of parameters			
	A	B	C	D	$MR$ [mm/min]	$TWR$ [g/min]	$OC$ [mm]	$TOC$ [mm]
1	1	1	1	1	0.019137	0.00261	0.2419	0.04839
2	1	2	2	2	0.042738	0.00466	0.1630	0.06966
3	1	3	3	3	0.065654	0.00205	0.1978	0.03706
4	2	1	1	2	0.056586	0.00351	0.1885	0.05388
5	2	2	2	3	0.049971	0.00410	0.1328	0.03871
6	2	3	3	1	0.062078	0.00317	0.1398	0.04179
7	3	1	2	1	0.090978	0.00905	0.1398	0.01508
8	3	2	3	2	0.051362	0.00366	0.1143	0.06070
9	3	3	1	3	0.072961	0.00675	0.0911	0.04752
10	1	1	3	3	0.044799	0.00371	0.1398	0.03871
11	1	2	1	1	0.039450	0.00436	0.1027	0.04284
12	1	3	2	2	0.032244	0.00559	0.1444	0.04806
13	2	1	2	3	0.081764	0.00526	0.1537	0.03786
14	2	2	3	1	0.050321	0.00456	0.1491	0.05987
15	2	3	1	2	0.043268	0.00399	0.1003	0.04493
16	3	1	3	2	0.070008	0.00488	0.1676	0.06497
17	3	2	1	3	0.062579	0.00699	0.1235	0.11196
18	3	3	2	1	0.081983	0.00456	0.1769	0.09516

Similarly, other computation was carried out for 18 experiments and the values of all  $\Delta_{0j}$  for  $j=1,2,3,\dots,18$  are represented in Table 4.

In continuation of data preprocessing, a coefficient for grey relational analysis is found using the relation given below [14]:

$$\xi_j(i) = \frac{\Delta_{\min} + \zeta \cdot \Delta_{\max}}{\Delta_{0j}(k) + \zeta \cdot \Delta_{\max}}, \quad (4)$$

where  $\zeta$  is a unique coefficient and  $\zeta$  is considered as 0.5 because all parameters are given equal weight.

The grey relational grade (GRG) presented in Table 5 is calculated by averaging the GRC and overall

**Table 4.** Performance characteristics of the processed data

Experiment run reference sequence	Performance characteristics after data processing				Deviation sequences			
	MR [mm/min]	TWR [g/min]	OC [mm]	TOC [mm]	MR [mm/min]	TWR [g/min]	OC [mm]	TOC [mm]
1	0.0000	0.9197	0.0000	0.6562	1.0000	0.0803	0.0000	0.3438
2	0.3285	0.6270	0.5231	0.4366	0.6715	0.3730	0.5231	0.5634
3	0.6475	1.0000	0.2924	0.7731	0.3525	0.0000	0.2924	0.2269
4	0.5213	0.7921	0.3539	0.5995	0.4787	0.2079	0.3539	0.4005
5	0.4292	0.7069	0.7231	0.7561	0.5708	0.2931	0.7231	0.2439
6	0.5977	0.8399	0.6769	0.7243	0.4023	0.1601	0.6769	0.2757
7	1.0000	0.0000	0.6769	1.0000	0.0000	1.0000	0.6769	0.0000
8	0.4486	0.7697	0.8462	0.5291	0.5514	0.2303	0.8462	0.4709
9	0.7492	0.3289	1.0000	0.6652	0.2508	0.6711	1.0000	0.3348
10	0.3572	0.7634	0.6769	0.7561	0.6428	0.2366	0.6769	0.2439
11	0.2827	0.6695	0.9231	0.7135	0.7173	0.3305	0.9231	0.2865
12	0.1824	0.4937	0.6462	0.6596	0.8176	0.5063	0.6462	0.3404
13	0.8718	0.5416	0.5846	0.7649	0.1282	0.4584	0.5846	0.2351
14	0.4341	0.6418	0.6154	0.5377	0.5659	0.3582	0.6154	0.4623
15	0.3359	0.7221	0.9385	0.6919	0.6641	0.2779	0.9385	0.3081
16	0.7081	0.5952	0.4923	0.4851	0.2919	0.4048	0.4923	0.5149
17	0.6047	0.2939	0.7846	0.0000	0.3953	0.7061	0.7846	1.0000
18	0.8748	0.6418	0.4308	0.1734	0.1252	0.3582	0.4308	0.8266

**Table 5.** Computed Grey relational grade

Experiment No.	GRC				Grey relational grade (GRG) $y_i = 1/4 \cdot (\xi_{i(1)} + \xi_{i(2)} + \xi_{i(3)} + \xi_{i(4)})$
	MR $\xi_{i(1)}$	TWR $\xi_{i(2)}$	OC $\xi_{i(3)}$	MR $\xi_{i(4)}$	
1	0.3333	0.8617	1.0000	0.5926	0.6969
2	0.4268	0.5727	0.4887	0.4702	0.4896
3	0.5865	1.0000	0.6310	0.6879	0.7263
4	0.5109	0.7063	0.5856	0.5552	0.5895
5	0.4669	0.6304	0.4088	0.6722	0.5446
6	0.5542	0.7574	0.4248	0.6446	0.5952
7	1.0000	0.3333	0.4248	1.0000	0.6895
8	0.4755	0.6847	0.3714	0.5150	0.5117
9	0.6660	0.4270	0.3333	0.5989	0.5063
10	0.4375	0.6788	0.4248	0.6722	0.5533
11	0.4108	0.6020	0.3514	0.6357	0.5000
12	0.3795	0.4969	0.4362	0.5949	0.4769
13	0.7959	0.5217	0.4610	0.6802	0.6147
14	0.4691	0.5826	0.4483	0.5196	0.5049
15	0.4295	0.6428	0.3476	0.6188	0.5097
16	0.6314	0.5526	0.5039	0.4927	0.5451
17	0.5585	0.4146	0.3892	0.3333	0.4239
18	0.7997	0.5826	0.5372	0.3769	0.5741

assessment of the multiple objective optimization determined using Eq. (5).

$$\gamma_j = \frac{1}{b} \sum_{a=1}^b \chi_i(a), \quad (5)$$

where  $\gamma_j$  is the GRG of  $j^{\text{th}}$  experiment and  $b$  is the number of performance characteristics.

### 3 DISCUSSION

The multi-response performance index presented in Table 6 presents the average value of the GRG for every level. The highest value of GRG indicates the best possible level of the process parameters. The calculated higher GRG value indicates the closeness to the optimal value. The total mean of the GRG for the eighteen runs was estimated and is presented in Table 6. The optimal parameter combination for better MR and lesser TWR, OC and TO is found to be (A<sub>1</sub>B<sub>1</sub>C<sub>3</sub>D<sub>1</sub>) as given in Table 6.

**Table 6.** Multi response performance index

Symbol	Level 1	Level 2	Level 3	Main effect (max-min)
A	0.5738	0.5598	0.5418	0.0321
B	0.6148	0.4958	0.5648	0.1191
C	0.5377	0.5649	0.5728	0.0351
D	0.5934	0.5204	0.5615	0.0730
$y_i = 0.5585$				

#### 3.1 ANOVA

The influence of process parameter on the performance characteristic was analyzed using analysis of variance (ANOVA). The effect of process parameters is measured by the sum of the squared deviations. It predicts the influential process parameter on output performance. The total sum of the squared deviations ( $SS_D$ ) from the total mean of the GRG  $y_i$  can be calculated as:

$$SS_D = \sum_{j=1}^p (\gamma_j - y_i)^2. \quad (6)$$

In which,  $p$  is the number of experiments in the OA and  $\gamma_j$  is the mean of the GRG for the  $j^{\text{th}}$  experiment.

The sum of the squares (SS) calculated is divided by degrees of freedom (DoF) to obtain mean square of a factor ( $MS_j$ ) or error ( $MS_e$ ). The percentage contribution ( $\phi$ ) of each of the design parameters is obtained using the Eq. (7) [14].

$$\phi_j = \frac{SS_j}{SS_T}. \quad (7)$$

Moreover, Fisher's test ( $F$  test) is also performed to establish machining parameters' influence on the performance characteristic [17]. ANOVA for GRG is presented in Table 7. Based on the ANOVA, table voltage and pulse off-time show a higher percentage contribution, hence voltage and pulse off-time are dominant parameters that affect the MR, TWR, OC and TOC. In EDM, increase voltage increase the current required for machining which improves the ionization effect between the tool and electrode. This ionization effect increases the temperature of the tool and electrode, resulting in melting of workpiece material. The molten material resulted from heating is evaporated during pulse off time of the EDM process. Hence, the voltage and pulse off-time are considered as significant factors in EDM.

**Table 7.** ANOVA table

Factors	DoF	SS	MSj	F ratio	$\phi$
$I$	2	0.003	0.0016	0.2931	2.72
$V$	2	0.042	0.0214	4.056	37.71
$t_{on}$	2	0.004	0.002	0.3841	3.57
$t_{off}$	2	0.016	0.008	1.521	14.14
Error	9	0.047	0.0053		41.84
Total	17	0.113	0.0067		100

#### 3.2 Confirmation Test

Confirmation tests were performed to show the improvement of performance characteristics [14]. The calculated GRG ( $I$ ) is calculated as shown below:

$$\eta = \eta_m + \sum_{i=1}^q (\eta_i - \eta_m), \quad (8)$$

where  $\eta_m$  is the total mean of the GRG,  $q$  is the number of significant parameters;  $\eta_i$  is the mean of the GRG at the optimal level. The predicted MR, TWR OC and TOC overcut and GRG for the best possible machining factors are estimated using the Eq. (8). Based on the confirmation test, GRG has improved by 0.0153 from the initial level; hence, as a whole, the performance of EDM process has been improved.

#### 3.3 TOPSIS

The TOPSIS method is used to find an ideal solution, and the following steps are followed to find the optimal parameter combination [18].

Step 1: The decision matrix consists of ‘ $n$ ’ attributes and ‘ $m$ ’ alternatives, and it is represented in Eq. (9).

$$A = \begin{bmatrix} T_{11} & T_{12} & \dots & T_{1n} \\ T_{21} & T_{22} & \dots & T_{2n} \\ \vdots & \vdots & \ddots & \vdots \\ T_{m1} & T_{m2} & \dots & T_{mn} \end{bmatrix} \quad (9)$$

Here  $T_{ij}$  is the performance of  $i^{\text{th}}$  alternative with respect to  $j^{\text{th}}$  attribute.

Step 2: Using Eq. (10), normalize decision matrix values were found.

$$r_{ij} = \frac{T_{ij}}{\sqrt{\sum_{i=1}^m T_{ij}^2}}, \quad j = 1, 2, \dots, n. \quad (10)$$

Step 3: Weight for each response are calculated, and the associated weights are multiplied with normalized decision matrix to obtain the weighted normalized decision matrix. The weighted normalized decision matrix is obtained as:

$$R_{ij} = M_i \times r_{ij}, \quad (11)$$

where  $i=1, \dots, m$  and  $j=1, \dots, n$ .  $M_j$  represents the weight of the  $j^{\text{th}}$  attribute or criteria.

Step 4: Positive ideal solution (PIS) and negative ideal solution (NIS) are determined as follows:

$$N^+ = (n_1^+, n_2^+, \dots, n_x^+) \text{ maximum values,} \quad (12)$$

$$N^- = (n_1^-, n_2^-, \dots, n_x^-) \text{ minimum values.} \quad (13)$$

Step 5: The separation of each alternative from positive ideal solution (PIS) is calculated as:

$$\alpha_i^+ = \sqrt{\sum_{j=1}^n (T_{ij} - x_j^+)^2}, \quad i = 1, 2, \dots, m. \quad (14)$$

The separation of alternatives from the negative-ideal solution is expressed in Eq. (15).

$$\alpha_i^- = \sqrt{\sum_{j=1}^n (T_{ij} - x_j^-)^2}, \quad i = 1, 2, \dots, m. \quad (15)$$

Step 6: Eq. (16) is used to find the relative proximity of the different alternative to the ideal solution.

$$P_i = \frac{\alpha_i^-}{\alpha_i^+ + \alpha_i^-}, \quad i = 1, 2, \dots, m. \quad (16)$$

Step 7: the  $P_i$  values (preference value) are ranked in descending order to find the optimal parameters combination.

### 3.4 TOPSIS Analysis

The four responses such as  $MR$ ,  $TWR$ ,  $OC$  and  $TOC$  are normalized using the Eq. (10). In this analysis, the weight criterion for  $MR$ ,  $TWR$ ,  $OC$  and  $TOC$  are 0.2154, 0.0177, 0.5644 and 0.2026, respectively. The relative normalized weight matrix has been computed using the proper weight criteria. The weight criteria are multiplied to obtain the normalized weighted matrix using Eq. (11). The ideal and the negative ideal solutions are calculated from the normalized weighted matrix table; that is,  $V_{MR}^+ = 0.0778$ ,  $V_{MR}^- = 0.0164$ ,  $V_{TWR}^+ = 0.0077$ ,  $V_{TWR}^- = 0.0002$ ,  $V_{OC}^+ = 0.5417$ ,  $V_{OC}^- = 0.2040$ ,  $V_{TOC}^+ = 0.0900$  and  $V_{TOC}^- = 0.0121$ . The separation measures of each condition from the ideal and negative ideal solutions were computed with Eqs. (14) and (15). Finally, the relative closeness coefficient (CC) value for each combination of factors of EDM process is calculated using Eq. (16), which is shown in Table 8. It is evident from Table 1 that experiment No. 1 is the best experiment and experiment No. 3 is second best alternative. According to this result, it is recommended to choose experiment No. 1, which has the highest proximity coefficient value among alternative experiments. Thus, it is evident from the TOPSIS analysis that the combination of process parameters such as 10 A, 30 V, 100  $\mu\text{s}$  and 20  $\mu\text{s}$  is suitable for the best EDM performance measures.

On comparing the grey-Taguchi and TOPSIS method results, the best level for  $I$ ,  $V$  and  $t_{off}$  are 10 A, 30 V and 20  $\mu\text{s}$ . Based on these results, the pulse on time shows two optimal levels, 100  $\mu\text{s}$  and 200  $\mu\text{s}$ , respectively. Although the levels for pulse on time are different, it will not have any significant impact on the performance since the contribution of pulse on time is very minimal, as shown in ANOVA Table 7. Hence, based on the results, it is clear that both these approaches are viable for arriving at the optimal process parameter combination with the available sparse data.

### 3.5 Analysis of Tool Wear

The tool electrode is the important factor which decides the shape accuracy of the drilled hole. In order to understand the tool wear behaviour, experiments are conducted by varying one parameter at a time. Based on Table 7, the voltage is the most influential parameters. Hence, the voltage is varied by keeping

**Table 8.** Normalized data, weighted normalized data, separation measures and closeness coefficient values

Experiment No.	Normalized data				Weighted normalized data				Separation measures		Closeness coefficient Pi
	MR	TWR	OC	TOC	MR	TWR	OC	TOC	$\alpha_i^+$	$\alpha_i^-$	
1	0.0759	0.0104	0.9598	0.1920	0.0164	0.0002	0.5417	0.0389	0.0802	0.3644	0.8196
2	0.1696	0.2235	0.6467	0.2764	0.0365	0.0039	0.3650	0.0560	0.1846	0.2062	0.5276
3	0.2605	0.0983	0.7848	0.1470	0.0561	0.0017	0.4429	0.0298	0.1178	0.2599	0.6881
4	0.2245	0.1684	0.7479	0.2138	0.0484	0.0030	0.4221	0.0433	0.1318	0.2516	0.6563
5	0.1983	0.1967	0.5269	0.1536	0.0427	0.0035	0.2974	0.0311	0.2538	0.1161	0.3138
6	0.2463	0.1521	0.5547	0.1658	0.0531	0.0027	0.3130	0.0336	0.2368	0.1365	0.3657
7	0.3610	0.4341	0.5547	0.0598	0.0778	0.0077	0.3130	0.0121	0.2415	0.1254	0.3417
8	0.2038	0.1756	0.4535	0.2408	0.0439	0.0031	0.2559	0.0488	0.2907	0.0955	0.2473
9	0.2895	0.3238	0.3614	0.1885	0.0624	0.0057	0.2040	0.0382	0.3420	0.0724	0.1747
10	0.1777	0.1780	0.5547	0.1536	0.0383	0.0031	0.3130	0.0311	0.2394	0.1303	0.3524
11	0.1565	0.2091	0.4075	0.1700	0.0337	0.0037	0.2300	0.0344	0.3197	0.0537	0.1439
12	0.1279	0.2681	0.5729	0.1907	0.0276	0.0047	0.3233	0.0386	0.2299	0.1465	0.3892
13	0.3244	0.2523	0.6098	0.1502	0.0699	0.0045	0.3442	0.0304	0.2065	0.1684	0.4493
14	0.1997	0.2187	0.5916	0.2375	0.0430	0.0039	0.3339	0.0481	0.2148	0.1686	0.4397
15	0.1717	0.1914	0.3979	0.1783	0.0370	0.0034	0.2246	0.0361	0.3242	0.0533	0.1412
16	0.2778	0.2341	0.6650	0.2578	0.0598	0.0041	0.3753	0.0522	0.1716	0.2169	0.5583
17	0.2483	0.3353	0.4900	0.4442	0.0535	0.0059	0.2765	0.0900	0.2662	0.1596	0.3747
18	0.3253	0.2187	0.7019	0.3776	0.0701	0.0039	0.3961	0.0765	0.1464	0.2639	0.6431

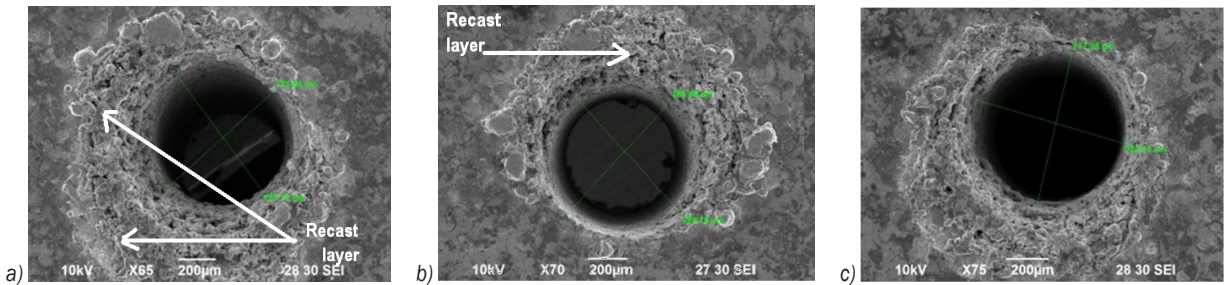


**Fig. 2.** SEM micrographs; a) 30 V, 14 A, 200 µs and 40 µs, b) 40 V, 14 A, 200 µs and 40 µs, c) 50 V, 14 A, 200 µs and 40 µs

the other parameters such  $I$ ,  $t_{on}$ , and  $t_{off}$  constant. The voltage value is varied as 30 V, 40 V, 50 V by keeping the  $I$ ,  $t_{on}$ , and  $t_{off}$  at 14 A, 200 µs, and 40 µs, respectively. Each experiment is repeated once. Based on the SEM micrograph, which is shown in Fig. 2, it is evident that the wear pattern varies with the voltage. It is evident from Fig. 2 that the recast layer pattern observed around the circumference of the hole varies with voltage. It is due to the fact that tool wear on the electrode is not even and, hence, the uneven electrode face will have different proximity towards the workface, resulting in uneven recast layer on the circumference of the hole. Further studies are required to understand the tool wear behaviour when machining Inconel 718.

#### 4 CONCLUSIONS

Machining characteristic optimization of EDM for Inconel 718 is preformed using grey-Taguchi method. The optimal machining parameters were found using GRG for multi-performance characteristics. Eighteen experimental runs based on OA have been performed. The optimal combination of input parameter to acquire better responses based on grey-Taguchi has been found to be  $I$  (10 A),  $V$  (30 V),  $t_{on}$  (200 µs) and  $t_{off}$  (20 µs). According to ANOVA, the voltage and  $t_{off}$  plays a prominent role in machining Inconel 718. The confirmation test result proves that there is a notable improvement in the GRA value from 0.6969 to 0.7122, when machining is done with the optimal parametric combination. Based on the confirmation

test, it is evident that GRA may be applied with sparse data in manufacturing industries to optimize the EDM process parameters to be competitive in the market. The best combinations identified using the TOPSIS method for better performance measures is 10 A, 30 V, 100  $\mu$ s and 20  $\mu$ s. These multi-objective optimization techniques are found to be suitable for optimizing the EDM process parameter. Tool wear behaviour is also studied through SEM images by varying the voltage. The SEM micrographs confirm that the wear pattern varies with the voltage. Hence detail analysis and optimization of electrical parameters may be considered as future work.

## 5 REFERENCES

- [1] Shen, Y., Liu, Y., Dong, H., Zhang, K., Lv, L., Zhang, X., Wu, X., Zheng, C., Ji, R. (2017). Surface integrity of Inconel 718 in high-speed electrical discharge machining milling using air dielectric. *The International Journal of Advanced Manufacturing Technology*, vol. 90, no. 1-4, p. 691-698, DOI:10.1007/s00170-016-9332-7.
- [2] Talla, G., Gangopadhyay, S., Biswas, C.K. (2016). Effect of powder-suspended dielectric on the EDM characteristics of Inconel 625. *Journal of Materials Engineering and Performance*, vol. 25, no. 2, p. 704-717, DOI:10.1007/s11665-015-1835-0.
- [3] Talla, G., Gangopadhyay, S., Biswas, C.K. (2017). Influence of graphite powder mixed EDM on the surface integrity characteristics of Inconel 625. *Particulate Science and Technology: An International Journal*, vol. 35, no. 2, p. 219-226, DOI:10.1080/02726351.2016.1150371.
- [4] Dhanabalan, S., Sivakumar, K., Sathiyaraj, Narayanan, C. (2014). Analysis of form tolerances in electrical discharge machining process for Inconel 718 and 625. *Materials and Manufacturing Processes*, vol. 29, no. 3, p. 253-259, DOI:10.1080/10426914.2013.852213.
- [5] Torres, A., Luis, C.J., Puertas, I. (2015). Analysis of the influence of EDM parameters on surface finish material removal rate and electrode wear of an Inconel 600 alloy. *The International Journal of Advanced Manufacturing Technology*, vol. 80, no. 1-4, p. 123-140, DOI:10.1007/s00170-015-6974-9.
- [6] Tanjilul, M., Ahmed, A., Senthil Kumar, A., Rahman, M. (2018). A study on EDM debris particle size and flushing mechanism for efficient debris removal in EDM-drilling of Inconel 718. *Journal of Materials Processing Technology*, vol. 255, p. 263-274, DOI:10.1016/j.jmatprotec.2017.12.016.
- [7] Rajesha, S., Sharma, A.K., Kumar, P. (2012). On electro discharge machining of Inconel 718 with hollow tool. *Journal of Materials Engineering and Performance*, vol. 21, no. 6, p. 882-891, DOI:10.1007/s11665-011-9962-8.
- [8] Kuppan, P., Rajadurai, A., Narayanan, S. (2008). Influence of EDM process parameters in deep hole drilling of Inconel 718. *The International Journal of Advanced Manufacturing Technology*, vol. 38, no. 1-2, p. 74-84, DOI:10.1007/s00170-007-1084-y.
- [9] Mohanty, A., Talla, G., Gangopadhyay, S. (2014). Experimental investigation and analysis of EDM characteristics of Inconel 825. *Materials and Manufacturing Processes*, vol. 29, no. 5, p. 540-549, DOI:10.1080/10426914.2014.901536.
- [10] Mohanty, C.P., Satpathy, M.P., Mahapatra, S.S., Singh, M.N. (2018). Optimization of cryo-treated EDM variables using TOPSIS-based TLBO algorithm. *Sadhana*, vol. 43, no. 51, DOI:10.1007/S12046-018-0829-7.
- [11] Dang, X.P. (2018). Constrained multi-objective optimization of EDM process parameters using kriging model and particle swarm algorithm. *Materials and Manufacturing Processes*, vol. 33, no. 4, p. 397-404, DOI:10.1080/10426914.2017.1292037.
- [12] Lin, M.-Y., Tsao, C.-C., Hsu, C.-Y., Chiou, A.-H., Huang, P.-C., Lin, Y.-C. (2013). Optimization of micro milling electrical discharge machining of Inconel 718 by Grey-Taguchi method. *Transactions of Nonferrous Metals Society of China*, vol. 23, no. 3, p. 661-666, DOI:10.1016/S1003-6326(13)62513-3.
- [13] Muthuramalingam, T., Mohan, B. (2013). Taguchi-grey relational based multi response optimization of electrical process parameters in electrical discharge machining. *Indian Journal of Engineering & Materials Science*, vol. 20, no. 6, p. 471-475.
- [14] Lin, M.Y., Tsao, C.C., Huang, H.H., Wu, C.Y., Hsu, C.Y. (2015). Use of the grey-Taguchi method to optimise the micro-electrical discharge machining (micro-EDM) of Ti-6Al-4V alloy. *International Journal of Computer Integrated Manufacturing*, vol. 28, no. 6, p. 569-576, DOI:10.1080/0951192X.2014.880946.
- [15] Deng, J.L. (1982). Control problems of grey systems. *System & Control Letters*, vol. 1, no. 5, p. 288-294, DOI:10.1016/S0167-6911(82)80025-X.
- [16] Nalbant, M., Altın, A., Gökkaya, H. (2007). The effect of cutting speed and cutting tool geometry on machinability properties of nickel-base Inconel 718 super alloys. *Materials & Design*, vol. 28, no. 4, p. 1334-1338, DOI:10.1016/j.matdes.2005.12.008.
- [17] Fisher, R.A. (1925). *Statistical Methods for Research Worker*, Oliver & Boyd, London.
- [18] Ramesh, S., Viswanathan, R., Ambika, S. (2016). Measurement and optimization of surface roughness and tool wear via grey relational analysis, TOPSIS and RSA techniques. *Measurement*, vol. 78, p. 63-72, DOI:10.1016/j.measurement.2015.09.036.

# Studying the Effect of Thermal Fatigue on Multiple Cracks Propagating in an SS316L Thin Flange on a Shaft Specimen Using a Multi-Physics Numerical Simulation Model

Fariha Mukhtar<sup>1</sup> – Faisal Qayyum<sup>2</sup> – Hassan Elahi<sup>3,\*</sup> – Masood Shah<sup>1</sup>

<sup>1</sup> University of Engineering and Technology, Department of Mechanical Engineering, Pakistan

<sup>2</sup> Technische Universität Bergakademie Freiberg, Institute for Metal Forming, Germany

<sup>3</sup> Sapienza University of Rome, Department of Mechanical and Aerospace Engineering, Italy

After more than a decade of research on thermal fatigue cracking in nuclear reactor components, the science remains incomplete. It is essential to understand the crack propagation behaviour and the influence of multiple cracks on the fatigue life of a component due to thermal fatigue load. Accurate numerical simulation modelling can help in better understanding the influence of different factors on failure propagation. In this research, a finite element-based numerical simulation model has been developed using ABAQUS commercial software to obtain insight into crack propagation and crack arrest in an SS316L thin flange on shaft specimen; the assembly is cooled internally, and cyclic thermal loading is applied on the flange rim. The experiment was carried out on a specially designed rig using an induction coil for heating the outer rim. Thermocouples were attached radially on the rim to collect detailed temperature profiles. Real-time temperature-dependent elastic-plastic material data was used for modelling. The boundary conditions and thermal profile used for the numerical model were matched with experimental data. The stresses responsible for crack initiation, the effect of crack number and crack lengths on stresses, energy absorbed at the crack tip after every thermal cycle and the threshold values of cracks are evaluated in the current work. The obtained simulation results were validated by comparing experimental observations. The developed simulation model helps in better understanding the evolution of stresses and strains in uncracked and cracked SS316L discs mounted on a flange due to thermal cycling. It also helped in better understanding the crack propagation behaviour and the evolution of energy release at crack tips. Such a model can help future researchers in designing components undergoing thermal fatigue loading, for example, in nuclear power plants.

**Keywords:** thermal fatigue, numerical simulation, SS316L, hoop stress, crack propagation, J-integral

## Highlights

- Thermal loads occurring in nuclear power plants were used as boundary conditions.
- A detailed temperature-dependent material model of SS316L was used during the simulation.
- Crack initiation and propagation were observed to estimate the fatigue life of the SS316L disc.
- Ratcheting behaviour of SS316L results in plastic deformation and blunting of the crack tip.
- The developed numerical simulation model predictions correspond well with experimental observations.

## 0 INTRODUCTION

Nuclear power plants are designed for more than 40 years of service life [1], but due to the aggressive operational conditions, unforeseen environmental conditions and material behaviour at elevated temperatures, the overall service life of the plant is affected [2]. One such problem was encountered in the residual heat removal system of the Civaux-1 power plant, France [3]. Due to higher toughness and superior corrosion resistance, austenitic stainless steels are used in the piping system of nuclear reactors [4]. AISI 321 is used in the secondary circuits of the water-water energetic reactor (WWER) nuclear power plants and heat exchangers. SS304 and SS304L are frequently used in pressurized water reactors [5]. SS316, SS316L, and SS316LN are mostly used in the piping system of light water reactors (LWR), and liquid metal cooled fast breeder reactors (LMFBR) [6]. Although tough, these components undergo

complex thermo-mechanical cycles during plant operations [7]. Varying temperatures in piping systems due to thermal stratifications, turbulent mixing of the hot and cold fluid and vortex penetration in different regions of the system, such as mixing tees, joints, and valves [8], result in thermal fatigue of such components [9]. Austenitic stainless steel can be primarily affected by these thermal fluctuations because of their high thermal expansion coefficient and low fatigue endurance limit [10]. The mechanism of fatigue crack initiation and propagation is similar in the case of thermal and mechanical loading conditions [11] and [12]. Though thermal fatigue damage has been proven to be more damaging than uniaxial isothermal fatigue [13] and [14], both are administered by the same fatigue mechanism. Out of these multiple cracks, only dominant cracks grow faster [15]. Cracks may nucleate from the well-developed slip bands, defects, inclusions, non-metallic impurities, or surface imperfections [16]. These geometrical discontinuities

\*Corr. Author's Address: Sapienza University of Rome, Dept. of Mechanical and Aerospace Engineering, Via Eudossiana 18, 00184 Rome, Italy; hassan.elahi@uniroma1.it

are present due to the adopted manufacturing process [17] and act as crack initiation sites during service [18] and [19]. The number of cycles to fatigue failure will significantly be decreased if the temperature is increased abruptly [20]. A fatigue crack, when initiated, grows slowly until the critical crack length is reached, after which the fatigue crack growth rate increases and leads to the failure of the component. Due to the lack of a thermal fatigue test standard, different experimental arrangements have been proposed by researchers for the thermal fatigue testing of materials [12] and [21]. Generally, researchers develop setups that are closer to actual conditions. For example, a two- and three-dimensional loading condition Splash test facility and FAT3D [22]. Other researchers for thermal fatigue testing of austenitic stainless-steel grades 304L, 316L were carried out under different temperature ranges for evaluating the crack initiation and propagation in pressurized water reactor (PWR) and LMFBR conditions using a SPLASH test facility [23].

Although several well-equipped experimental setups have been developed by researchers, it is still problematic and sometimes impossible to record critical material deformation and failure data while the test is in progress. Numerical simulation models developed in the past to study the fatigue life of metals [24], ceramics [25] and [26] and polymers [27] and [28] help understand the material deformation and failure behaviour under varying boundary and geometric conditions. They significantly contribute to reducing design cost and time.

Ullah et al. [29] showed that numerical simulation models could help in better understanding the fatigue crack propagation in material under complex thermo-mechanical loading conditions. Such models were also used to estimate the fatigue life of composite materials under dynamic loading conditions [30] and [31]. Recently, based on elastic-plastic material data and realistic boundary conditions, a method was developed by Qayyum et al. [15] to numerically model the crack propagation in complicated structures due to thermal fatigue. Such a model helps in successfully obtaining a deep insight into the complex thermal fatigue phenomena and therefore is adopted here.

In this research, a flange-shaft specimen made of SS316L is experimentally tested under thermal fatigue loading provided by induction heating and internal cooling. The simulation was developed by incorporating real-time temperature-dependent elastic-plastic material data to obtain insight into stress distribution and crack propagation in a flange rim.

## 1 EXPERIMENTATION

The specimen consisted of a hollow shaft of SS316L on which a flange was machined as an integral part. Specimen geometry and dimensions are shown in Fig. 1a. The idea behind using a thin flange is to have a plane stress condition at the crack tip for a more straightforward analysis. The experiment was carried out in collaboration with French partners at Ecole D' Mines, Albi, France. The specimen was heated rapidly by 2 MHz high-frequency induction heating and cooled internally by flowing water at room temperature. One thermal cycle lasts for 16 seconds, with 4 seconds of heating and 12 seconds of subsequent cooling. The experimental arrangement is shown in Fig. 1b.

The intended temperature profile was maintained and recorded with the help of spot-welded thermocouples at 0 mm, 2.75 mm, and 4.4 mm from the outer rim of the flange. The temperature profile obtained from experimentation is shown in Fig. 2 with the help of solid lines.

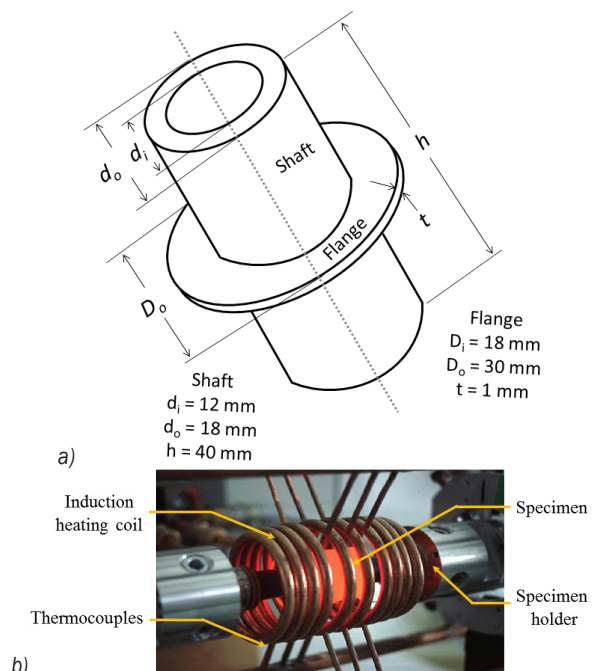


Fig. 1. Experiment; a) specimen geometry, and b) induction heating of the specimen

## 2 NUMERICAL SIMULATION

ABAQUS Standard™ is used as a finite element analysis tool for the modelling and simulation of thermal fatigue. In this analysis, a de-coupled thermo-

mechanical approach is used with a non-linear rate-independent elastic-plastic material model, as suggested by Fissolo et al. [13].

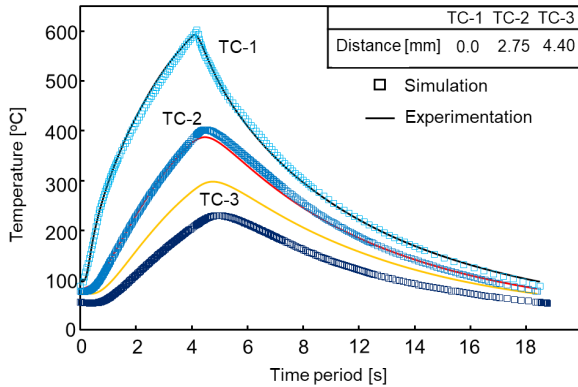


Fig. 2. Thermal profile matching the description of thermocouple positioning

2.1 Material Data

SS316L is a non-hardenable and non-magnetic grade of stainless steel. It is used where toughness and corrosion resistance are equally important [10]. The temperature-dependent material properties of SS316L, which are listed in Table 1, were incorporated in the numerical simulation model. The flow curves of the material at different temperatures are presented in Fig. 3. This temperature-dependent elastic-plastic material data was used in the numerical model definition.

Table 1. The temperature of dependent mechanical properties of SS316L [32]

Temperature [°C]	Young's modulus [GPa]	Thermal conductivity [W/(mm·K)]	Thermal expansion coefficient [ $10^{-5}/^{\circ}\text{C}$ ]	Specific heat [kJ/(kg·K)]
25	200	0.014	1.60	464.68
100	194	0.0149	1.66	-
200	185	0.016	-	-
300	177	0.0173	-	-
400	169	0.0186	-	515.6
500	160	0.0199	-	-
800	135	0.02	-	569.2
871	-	-	1.98	-

2.2 Loading and Constraints

Thermal heat flux of 2 W/mm<sup>2</sup> was applied at the rim of the disc in all simulation models. The temperature profiles at different depths in the numerical simulation model were matched with experimentally observed profiles by tuning the amplitude of heat flux and

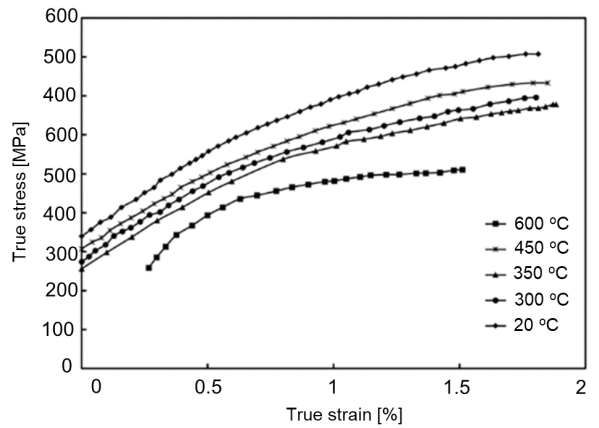


Fig. 3. Temperature-dependent plasticity data of SS316L [32]

cooling. The simulation was run for 30 fatigue cycles to obtain a stabilized stress-strain response. The boundary conditions defined for all simulation models are shown in Fig. 4a. Pinned boundary condition was applied at the internal periphery of the shaft. Element type DC2D4 (4-node linear heat transfer quadrilateral) was used to generate a total of 4260 linear quadrilateral elements on the whole assembly. The meshed assembly of disc and shaft

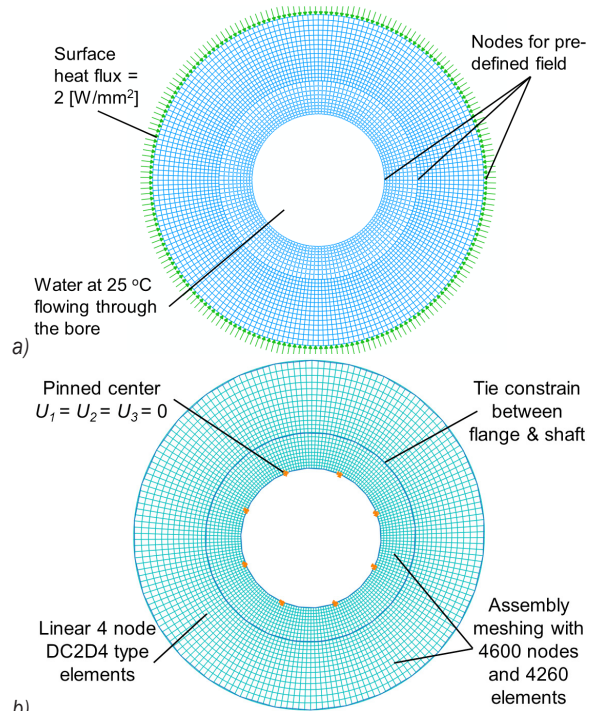


Fig. 4. Loading and constraints; a) heating model specifications, and b) mechanical model specifications

is shown in Fig. 4b. The model was checked for the mesh dependency and, during meshing, the aspect ratio (which is a measure of how well structured the mesh is, i.e., the perfect aspect ratio is 1.0) was maintained below 1.05. The readers are encouraged to refer to previous publications [33] and [34] to obtain more details about the numerical simulation model development, meshing, boundary conditions, and post-processing of data.

### 2.3 Mechanical Model

A total of 29 models were developed for this research with different crack lengths and numbers of cracks. The simulations were based on the sequence published earlier [12] and [35]. A thermal analysis was run, and the temperature evolution at each node was recorded to obtain nodal temperature distributions. A model was developed to study the effect of thermal cycling on the uncracked sample, which results in the highest hoop stresses. Twenty-seven models with different crack numbers and crack lengths were analysed to study the effect of varying crack numbers and crack lengths on evolving stresses at the periphery of the disc. The description of peripheral cracks is shown in Fig. 5.

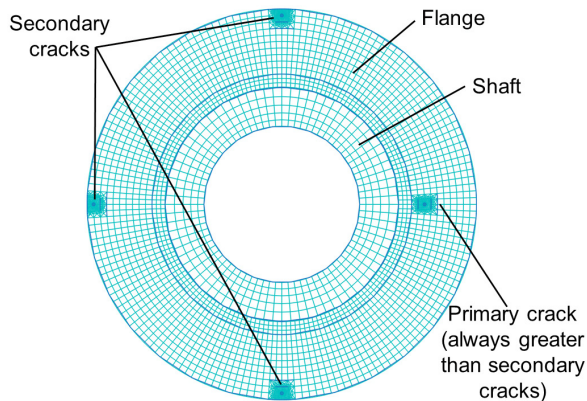


Fig. 5. Description of peripheral cracks in the specimen

## 3 RESULTS

Experimentally, it is observed that two diametrically opposite cracks initiate at the outer periphery of the flange. Cracks initiate in the flange after 6,000 thermal cycles. The two cracks originated were 180° apart from each other, the fatigue crack growth behavior of these cracks is presented in Fig. 6b. The same phenomenon of cracking was observed previously in the case of the H-11 tool steel disc [15]. In the case

of H-11 tool steel, multiple cracks originated on the periphery, out of which only eight cracks propagated throughout the experiment, which was validated through numerical simulation, whereas in this case only two noticeable cracks initiated and propagated up to 16,000 cycles. One of the cracks propagated to a crack length of 1640 μm, and the other grew up to 825 μm for the same number of cycles. The number of cycles to crack initiation and the significant crack lengths attained by the two cracks are shown in Fig. 6b.

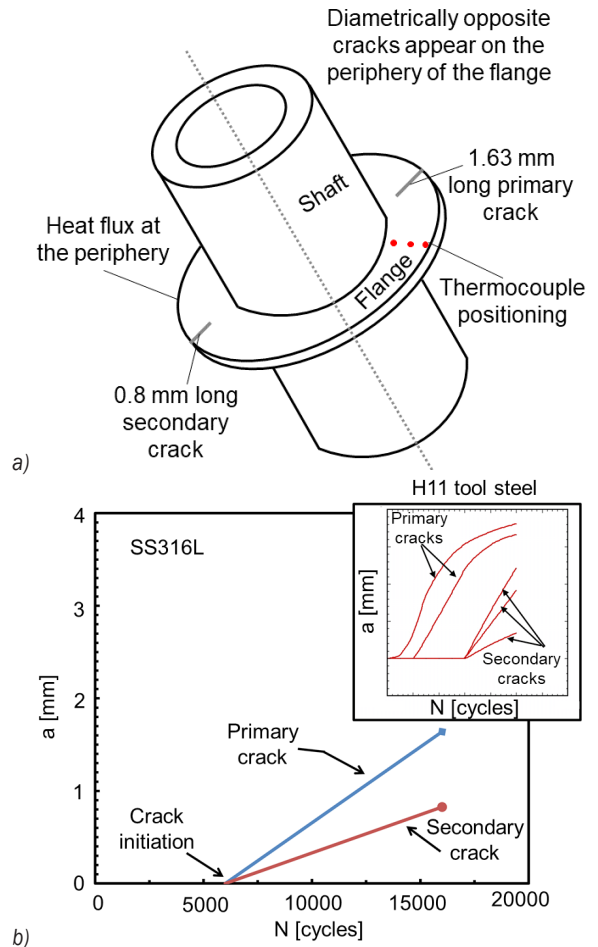


Fig. 6. Experimental results; a) no. of cycles to crack initiation, and b) diametrically opposite cracks as a result of thermal fatigue

### 3.1 Temperature- Stress Correspondence

Maximum hoops stress is observed at the rim of the flange. The change in hoop stress versus temperature when plotted forms a hysteresis loop, as shown in Fig. 7; the area under the hysteresis is representing the energy absorbed by the material itself to reach the peak stress with the increase in temperature. The

first cycle (from 0 to 1) shows a sudden increase in stress with increased temperature. Compressive stresses develop in the disc (from 1 to 2) when the temperature is raised while they start to transform into tensile stresses (from 2 to 3) during the cooling period. Tensile stress reaches a maximum magnitude of 396 MPa in the last cycle at point 4, which shows a 21 % increase in stress as compared to the 1<sup>st</sup> cycle. These stresses are responsible for the crack initiation in the disc. When the first and last cycle compressive stresses are compared, 13.4 % elevation is observed at point 2.

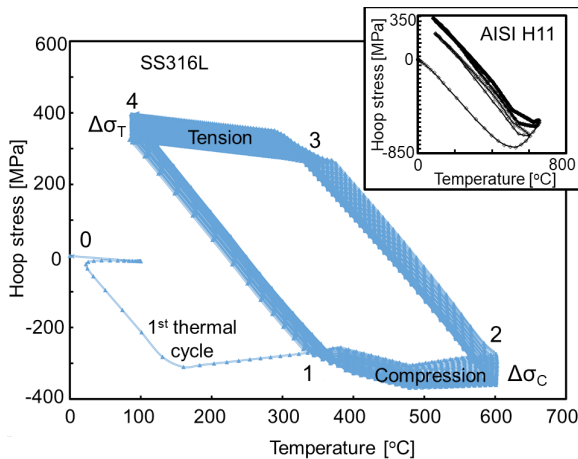


Fig. 7. Stress-temperature hysteresis of SS316L and H11 tool steel (for comparison)

### 3.2 Effect of Crack Lengths and Number of Cracks on Hoop Stress

Maximum hoops stress is observed on the rim of the flange. The variation in hoop stress on the rim due to cracking forms plateaus of hoop stresses which are presented in Fig. 8. In this figure,  $n$  is the number of cracks,  $a_p$  is the length of the primary crack,  $a_s$  is the length of the secondary crack. The graph shows that

hoop stress suddenly falls when a crack is introduced in the specimen. The initiation of the crack and its opening in the cooling cycle results in stress relief. An increasing number of cracks results in an overall decrease in hoop stress on the rim. By comparing Fig. 8a with Fig. 8b, it is observed that introducing a crack causes sudden stress relaxation at a particular point on the rim.

In the case of the SS316L disc, only two cracks initiate and propagate to significant lengths during the experimentation. This validates the numerical simulation results in which a 7 % drop in hoop stress is recorded when the crack number increases from 2 to 4, i.e., from Fig. 8b to Fig. 8c.

In Fig. 9, the secondary crack length is plotted as a function of hoop stress for different primary crack lengths. For every set of primary crack lengths, i.e., 2 mm, the hoop stress decreases with an increase in secondary crack length; the same is true for the set where primary crack length is kept at 3 mm and 4mm respectively. For a 2 mm secondary crack, hoop stress has a maximum value of 396 MPa. The minimum value of hoop stress for  $n = 4$  is recorded when the primary crack length is 4 mm, and the secondary crack length is 3 mm.

### 3.3 Crack Propagation Phenomenon

Anderson [36] has explained that either J-integral or the crack tip opening displacement (CTOD) can be used as a fracture criterion for time-independent, elastic-plastic behaviour of materials that are to be dealt with in non-linear elastic-plastic fracture mechanics. Both J-integral and CTOD give information about the crack- tip condition. Researchers have also associated the fatigue crack growth to the cyclic J-integral [37]. The time response of J-integral resulted in spikes, as shown in Fig. 10. Spikes are formed as a result of sudden rises and falls in the values of J-integral, which is governed by continuous thermal cycling of

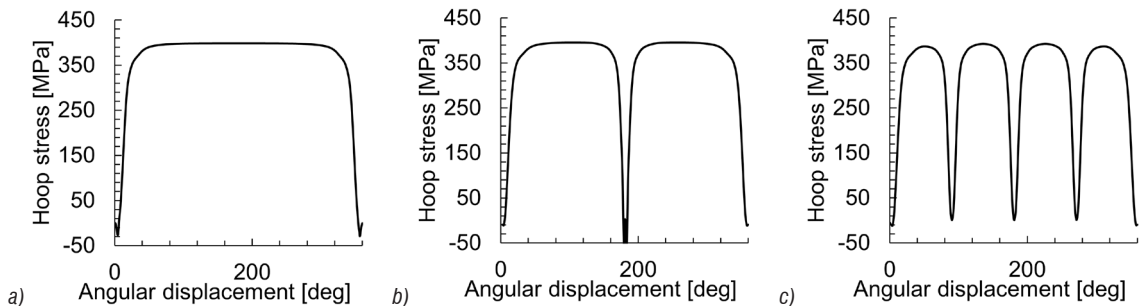


Fig. 8. Distribution of hoop stress along the periphery of the SS316L disc with different No. of cracks; a)  $n = 1, a_p = 2 \text{ mm}, a_s = 0 \text{ mm}$ , b)  $n = 2, a_p = 2 \text{ mm}, a_s = 1 \text{ mm}$ , and c)  $n = 4, a_p = 2 \text{ mm}, a_s = 1 \text{ mm}$

the flange. During the tension cycle, the crack opens, which results in the release of energy while in the compression cycle the crack remains closed; hence, no energy is being released. This release in energy results in crack propagation during the cooling cycle. The J-integral trend, in this case, is comparatively different from that observed in the case of H-11 tool steel. Although the spikes formed in the case of H-11 tool steel were comparable to that of SS316L, the J-integral does not become stabilized with subsequent thermal cycling in SS316L; the values seem shifted from the horizontal axis.

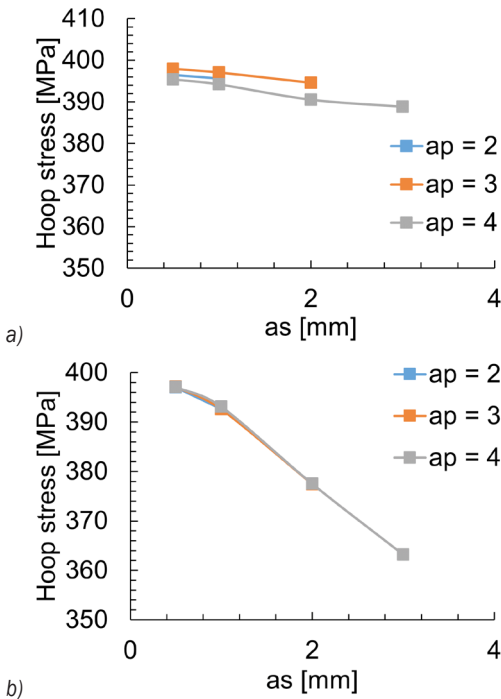


Fig. 9. Maximum hoop stress as a function of secondary crack length; a) for  $n = 2$ , and b) for  $n = 4$

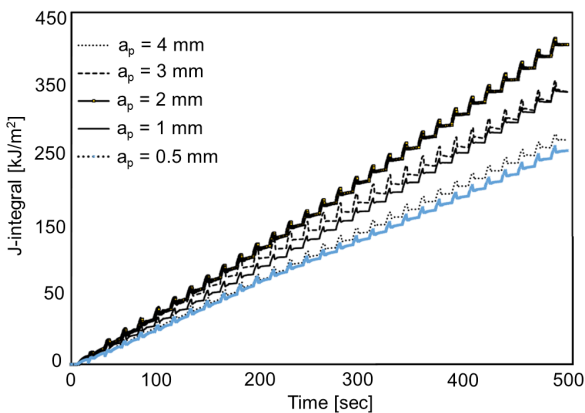


Fig. 10. J-integral vs. time; for  $n = 1$

The graph shown in Fig. 11 is the response of crack mouth opening displacement (CMOD) with respect to time. CMOD increases with time after every cycle. It is maximum at the instance at which tensile stress is maximum, i.e., at the end of every thermal cycle. The overall shift in the value of CMOD from the horizontal axis represents the cumulative plastic deformation at the crack tip, which is adding specific value to its displacement response taken for the last 12 cycles.

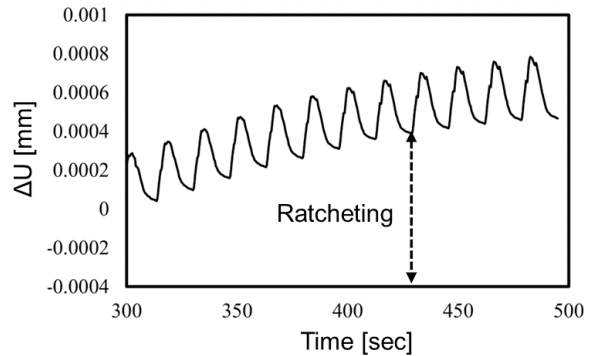


Fig. 11. CMOD vs. time for last 12 cycles,  $n = 1$ ,  $a_p = 1$  mm

#### 4 DISCUSSION

Maximum hoop stress is observed on the rim of the flange. The hoop stress is compressive during heating, reduces to zero, and eventually becomes tensile during cooling due to retained plasticity. In this research, these stresses were analysed using calibrated thermal and mechanical models, and it was observed that an energy hysteresis is observed in the case of SS316L with an increasing area. This shows that there is continuous energy absorption at the crack tip.

The crack initiation was not the main focus in this research but has been previously investigated to occur due to dislocations accumulation at grain boundaries, or inclusions or voids to form micro-cracks, which eventually join together to form a bigger crack, which grows larger under the influence of tensile stresses.

During each thermal cycle, a complex phenomenon occurs at the crack tip. This research was carried out to see and understand this phenomenon in a better way. In the first thermal cycle during heating, the material softens, and compressive hoop stresses accumulate on the rim of the flange, and the crack faces close, as shown in Fig. 12a. Tensile hoop stresses originate during cooling, which is responsible for crack opening, as can be observed in Fig. 12b.

It is observed in this research that during cyclic thermal loading, stainless steel undergoes ratcheting

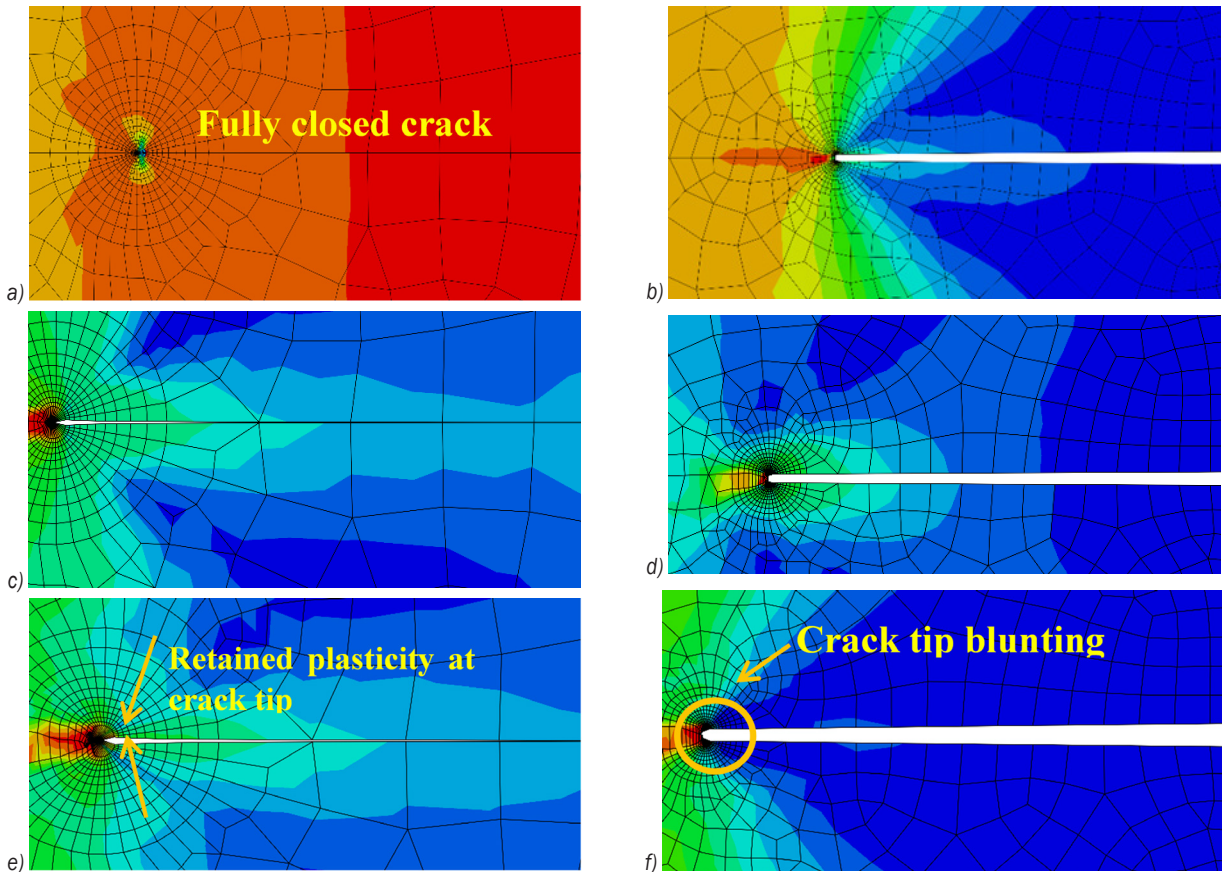


**Fig. 12.** Crack tip condition in subsequent cycles

a) 1<sup>st</sup> compression cycle, b) 1<sup>st</sup> tension cycle, c) 5<sup>th</sup> compression cycle, d) 5<sup>th</sup> tension cycle, e) 30<sup>th</sup> compression cycle, f) 30<sup>th</sup> tension cycle

behaviour. Energy absorption at crack tip results in crack tip blunting and with subsequent thermal cycles the crack tip does not close even at the highest temperature. This can be seen for the 5<sup>th</sup> cycle in Figs. 12c and d and for the 30<sup>th</sup> cycle in Figs. 12e, and f.

The J-integral shows an increasing trend with the increase in crack length in Fig. 10. The J-integral reaches its maximum value after 30 cycles. It is observed that the J-integral increases with an increase in crack length up to 2 mm. There is a 15.33 % increase in energy release rate when the crack grows from 1 mm to 2 mm. On further increasing the crack length up to 3 mm, the maximum value of the energy release rate was approximately the same as that for a crack length of 1 mm. On further increase in crack length from 2 mm to 3 mm and 4 mm, 15.34 % and 29 % drops in corresponding values of J-integral are recorded.

CMOD and CTOD are the two parameters that are also used to estimate the crack growth rate. Researchers have associated the fatigue crack propagation to the CMOD [38]. CMOD increases

with an increase in crack length, as shown in Fig. 11. 0.61 % decrease in hoop stress is observed where the number of cracks remains the same while secondary crack length increases from 1 mm to 2 mm. For both the cases, i.e.  $n = 2$  and  $n = 4$ , CMOD increases with an increase in secondary crack length. An overall decrease can be seen in Fig. 11, when  $n = 4$  which points towards the limitation of the number of cracks on the periphery. Fig. 11 shows that CMOD increases with an increase in primary crack length. The relationship curve between primary crack length and CMOD for  $n = 4$  overlaps with  $n = 2$ . It shows that for greater crack length, CMOD will be more independent of the number of cracks.

## 5 CONCLUSIONS

In this research, a cracked and un-cracked flange-shaft specimen of SS316L was numerically simulated using the elastic-plastic material model with isotropic hardening in Mode-I fracture. The simulation was based on the results obtained by the experimentation

of the disc type specimen of SS316L under cyclic thermal loading provided by the induction heating and internal cooling. The experiment resulted in two diametrically opposed cracks, which propagated to 1640  $\mu\text{m}$  and 825  $\mu\text{m}$  in length. The results of the numerical simulation give the agreeable validation of the experiment. The obtained results can be concluded as follows:

- Material permanently deforms in the first thermal cycle. During thermal cycling, stress reverses itself and results in a stress-strain hysteresis. The pair of stresses developed in the specimen exceeds the fatigue endurance limit of the material.
- Hoop stress on the flange stands responsible for crack initiation in it. When the number of cracks is increased from  $n = 2$  to  $n = 4$ , a maximum drop of 6.4 % in hoop stress is recorded, which justifies the two-crack formation phenomenon during experimentation.
- The J-integral gave us the possible range of primary crack length, which is  $0.5 \text{ mm} \leq a_p \leq 2.5 \text{ mm}$  while there is enough energy available in the specimen to drive the secondary crack up to 2 mm.
- CMOD increases regardless of the number of cracks or crack length, thus cannot be relied on as a suitable identifier of thermal fatigue damage.
- The time response of J-integral and CMOD points towards the ratcheting behaviour of SS316L and crack blunting in the specimen.

## 7 NOMENCLATURE

$n$	number of cracks
$N$	number of cycles
$a$	crack length, [mm]
$a_s$	secondary crack length, [mm]
$a_p$	primary crack length, [mm]
$U_1$	displacement in X-direction
$U_2$	displacement in Y-direction
$U_3$	displacement in Z-direction
$d_i$	pipe inner diameter, [mm]
$d_o$	pipe outer diameter, [mm]
$h$	height of pipe, [mm]
$D_i$	flange inner diameter, [mm]
$D_o$	flange outer diameter, [mm]
$t$	thickness of flange, [mm]

## 8 REFERENCES

- [1] Le Duff, J.-A., Ould, P., Bernard, J.-L. (1996). Fatigue crack initiation and propagation in austenitic stainless steels for light water reactors. *International Journal of Pressure Vessels and Piping*, vol. 65, no. 3, p. 241-253, DOI:10.1016/0308-0161(94)00135-6.
- [2] Paffumi, E., Nilsson, K.-F., Szaraz, Z. (2015). Experimental and numerical assessment of thermal fatigue in 316 austenitic steel pipes. *Engineering Failure Analysis*, vol. 47, p. 312-327, DOI:10.1016/j.engfailanal.2014.01.010.
- [3] Cipièrè, M.F., Le Duff, J.A. (2002). Thermal fatigue experience in french piping: Influence of surface condition and weld local geometry. *Welding in the World*, vol. 46, no. 1-2, p. 23-27, DOI:10.1007/BF03266362.
- [4] Avner, S.H. (1974). *Introduction to Physical Metallurgy*. McGraw-Hill, New York.
- [5] Kadlec, M., Haušild, P., Siegl, J., Materna, A., Bystrianský, J. (2012). Thermal fatigue crack growth in stainless steel. *International Journal of Pressure Vessels and Piping*, vol. 98, p. 89-94, DOI:10.1016/j.ijpvp.2012.07.005.
- [6] Prasad Reddy, G.V., Kannan, R., Mariappan, K., Sandhya, R., Sankaran, S., Rao, K.B.S. (2015). Effect of strain rate on low cycle fatigue of 316LN stainless steel with varying nitrogen content: Part-I cyclic deformation behavior. *International Journal of Fatigue*, vol. 81, p. 299-308, DOI:10.1016/j.ijfatigue.2015.07.033.
- [7] Wang, Y., Charbal, A., Hild, F., Vincent, L. (2018). High cycle thermal fatigue of austenitic stainless steel. *MATEC Web of Conferences*, p. 19009, DOI:10.1051/mateconf/201816519009.
- [8] Paffumi, E., Nilsson, K.-F., Taylor, N.G. (2008). Simulation of thermal fatigue damage in a 316L model pipe component. *International Journal of Pressure Vessels and Piping*, vol. 85, no. 11, p. 798-813, DOI:10.1016/j.ijpvp.2008.06.002.
- [9] Zhan, J., Li, M., Huang, J., Bi, H., Li, Q., Gu, H. (2019). Thermal fatigue characteristics of type 309 austenitic stainless steel for automotive manifolds. *Metals*, vol. 9, no. 2, p. 129, DOI:10.3390/met9020129.
- [10] McGuire, M.F. (2008). *Stainless Steels for Design Engineers*. ASM International, Materials Park.
- [11] Qayyum, F., Kamran, A., Ali, A., Shah, M. (2017). 3D numerical simulation of thermal fatigue damage in wedge specimen of AISI H13 tool steel. *Engineering Fracture Mechanics*, vol. 180, p. 240-253, DOI:10.1016/j.engfracmech.2017.05.020.
- [12] Elahi, H., Eugeni, M., Gaudenzi, P., Qayyum, F., Swati, R.F., Khan, H.M. (2018). Response of piezoelectric materials on thermomechanical shocking and electrical shocking for aerospace applications. *Microsystem Technologies*, vol. 24, no. 9, p. 3791-3798, DOI:10.1007/s00542-018-3856-8.
- [13] Fissolo, A., Amiabile, S., Ancelet, O., Mermaz, F., Stelmaszyk, J.M., Constantinescu, A., Robertson, C., Vincent, L., Maillot, V., Bouchet, F. (2009). Crack initiation under thermal fatigue: An overview of cea experience. Part I: Thermal fatigue appears to be more damaging than uniaxial isothermal fatigue. *International Journal of Fatigue*, vol. 31, no. 3, p. 587-600, DOI:10.1016/j.ijfatigue.2008.03.038.
- [14] Swati, R.F., Wen, L.H., Elahi, H., Khan, A.A., Shad, S. (2019). Experimental and numerical investigation of transversal damage in carbon fiber reinforced composites using X-FEM analysis. *Journal of Mechanical Science and Technology*, vol. 33, no. 1, p. 205-211, DOI:10.1007/s12206-018-1220-7.

- [15] Qayyum, F., Shah, M., Shakeel, O., Mukhtar, F., Salem, M., Rezaei-Aria, F. (2016). Numerical simulation of thermal fatigue behavior in a cracked disc of AISI H-11 tool steel. *Engineering Failure Analysis*, vol. 62, p. 242-253, DOI:10.1016/j.engfailanal.2016.01.015.
- [16] Mukhtar, F., Qayyum, F., Anjum, Z., Shah, M. (2019). Effect of chrome plating and varying hardness on the fretting fatigue life of AISI D2 components. *Wear*, vol. 418-419, p. 215-225, DOI: j.wear.2018.12.001.
- [17] Klesnil, M., Lukác, P. (1992). *Fatigue of Metallic Materials*. Elsevier, Amsterdam.
- [18] Kerezi, B.B., Price, J.W.H. (2002). Using the ASME and BSI codes to predict crack growth due to repeated thermal shock. *International Journal of Pressure Vessels and Piping*, vol. 79, no. 5, p. 361-371, DOI:10.1016/S0308-0161(02)00023-6.
- [19] Swati, R.F., Elahi, H., Wen, L.H., Khan, A.A., Shad, S., Mughal, M.R. (2018). Investigation of tensile and in-plane shear properties of carbon fiber reinforced composites with and without piezoelectric patches for micro-crack propagation using extended finite element method. *Microsystem Technologies*, vol. 25, no. 6, p. 2361-2370, DOI:10.1007/s00542-018-4120-y.
- [20] Srivastava, A., Joshi, V., Shivpuri, R. (2004). Computer modeling and prediction of thermal fatigue cracking in die-casting tooling. *Wear*, vol. 256, no. 1-2, p. 38-43, DOI:10.1016/S0043-1648(03)00281-3.
- [21] Memmolo, V., Elahi, H., Eugeni, M., Monaco, E., Ricci, F., Pasquali, M., Gaudenzi, P. (2019). Experimental and numerical investigation of pzt response in composite structures with variable degradation levels. *Journal of Materials Engineering and Performance*, vol. 28, no. 6, p. 3239-3246, DOI:10.1007/s11665-019-04011-4.
- [22] Khan, M.U., Butt, Z., Elahi, H., Asghar, W., Abbas, Z., Shoab, M., Bashir, M.A. (2018). Deflection of coupled elasticity-electrostatic bimorph PVDF material: theoretical, FEM and experimental verification. *Microsystem Technologies*, vol. 25, no. 8, p. 3235-3242, DOI:10.1007/s00542-018-4182-x.
- [23] Amiable, S., Chapuliot, S., Constantinescu, A., Fissolo, A. (2006). A comparison of lifetime prediction methods for a thermal fatigue experiment. *International Journal of Fatigue*, vol. 28, no. 7, p. 692-706, DOI:10.1016/j.ijfatigue.2005.09.002.
- [24] Wang, Y., Charbal, A., Hild, F., Roux, S., Vincent, L. (2019). Crack initiation and propagation under thermal fatigue of austenitic stainless steel. *International Journal of Fatigue*, vol. 124, p. 149-166, DOI:10.1016/j.ijfatigue.2005.09.002.
- [25] Elahi, H., Eugeni, M., Gaudenzi, P. (2019). Design and performance evaluation of a piezoelectric aeroelastic energy harvester based on the limit cycle oscillation phenomenon. *Acta Astronautica*, vol. 157, p. 233-240, DOI:10.1016/j.actaastro.2018.12.044.
- [26] Butt, Z., Anjum, Z., Sultan, A., Qayyum, F., Ali, H.M.K., Mehmood, S. (2017). Investigation of electrical properties & mechanical quality factor of piezoelectric material (PZT-4A). *Journal of Electrical Engineering & Technology*, vol. 12, no. 2, p. 846-851, DOI:10.5370/jeet.2017.12.2.846.
- [27] Najabat Ali, M., Ansari, U., Sami, J., Qayyum, F., Mir, M. (2016). To develop a biocompatible and biodegradable polymer-metal composite with good; mechanical and drug release properties. *Journal of Material Sciences & Engineering*, vol. 5, no. 5, p. 1-4, DOI:10.4172/2169-0022.1000274.
- [28] Mir, M., Ali, M.N., Ansari, U., Smith, P.J., Zahoor, A., Qayyum, F., Abbas, S. (2019). Aqua-gel pH sensor: Intelligent engineering and evaluation of pH sensor based on multi-factorial testing regimes. *Sensor Review*, vol. 39, no. 2, p. 178-189, DOI:10.1108/sr-06-2017-0104.
- [29] Ullah, M., Pasha, R.A., Chohan, G.Y., Qayyum, F. (2015). Numerical simulation and experimental verification of CMOD in CT specimens of TIG welded AA2219-T87. *Arabian Journal for Science and Engineering*, vol. 40, no. 3, p. 935-944, DOI:10.1007/s13369-015-1569-1.
- [30] Asghar, W., Nasir, M.A., Qayyum, F., Shah, M., Azeem, M., Nauman, S., Khushnood, S. (2017). Investigation of fatigue crack growth rate in CARALL, ARALL and GLARE. *Fatigue & Fracture of Engineering Materials & Structures*, vol. 40, no. 7, p. 1086-1100, DOI:10.1111/ffe.12566.
- [31] Swati, R.F., Wen, L.H., Elahi, H., Khan, A.A., Shad, S. (2019). Extended finite element method (XFEM) analysis of fiber reinforced composites for prediction of micro-crack propagation and delaminations in progressive damage: A review. *Microsystem Technologies*, vol. 25, no. 3, p. 747-763, DOI:10.1007/s00542-018-4021-0.
- [32] Kim, J.-B., Lee, H.-Y., Park, C.-G., Lee, S.-H., Lee, J.-H. (2005). The temperature dependent inelastic material characteristics of cold worked 316L for NONSTA. *Proceedings of the Korean Nuclear Society Conference*, p. 1-2.
- [33] Anjum, Z., Qayyum, F., Khushnood, S., Ahmed, S., Shah, M. (2015). Prediction of non-propagating fretting fatigue cracks in Ti6Al4V sheet tested under pin-in-dovetail configuration: Experimentation and numerical simulation. *Materials & Design*, vol. 87, p. 750-758, DOI:10.1016/j.matdes.2015.08.070.
- [34] Qayyum, F., Shah, M., Manzoor, S., Abbas, M. (2015). Comparison of thermomechanical stresses produced in work rolls during hot and cold rolling of cartridge brass 1101. *Materials Science and Technology*, vol. 31, no. 3, p. 317-324, DOI:10.1179/1743284714Y.0000000523.
- [35] Khan, F., Qayyum, F., Asghar, W., Azeem, M., Anjum, Z., Nasir, A., Shah, M. (2017). Effect of various surface preparation techniques on the delamination properties of vacuum infused carbon fiber reinforced aluminum laminates (CARALL): Experimentation and numerical simulation. *Journal of Mechanical Science and Technology*, vol. 31, no. 11, p. 5265-5272, DOI:10.1007/s12206-017-1019-y.
- [36] Anderson, T.L. (2005). *Solutions Manual for Fracture Mechanics: Fundamentals and Applications*. Taylor & Francis, Abingdon-on-Thames.
- [37] Sadananda, K., Shahinian, P. (1980). *Fracture Mechanics*, ASTM International, West Conshohocken.
- [38] Schweizer, C., Seifert, T., Nieweg, B., von Hartrott, P., Riedel, H. (2011). Mechanisms and modelling of fatigue crack growth under combined low and high cycle fatigue loading. *International Journal of Fatigue*, vol. 33, no. 2, p. 194-202, DOI:10.1016/j.ijfatigue.2010.08.008.

# Buckling of Joined Composite Conical Shells Using Shear Deformation Theory under Axial Compression

Mohammad Hadi Izadi – Shahrokh Hosseini Hashemi\* – Moharam Habibnejad Korayem  
Iran University of Science and Technology, Department of Mechanical Engineering, Iran

*This paper investigates critical buckling loads in joined conical shells under axial compression. An analytical approach has been applied to study classical linear buckling of joined cones that are made of cross-ply fiber reinforced laminates. The governing equations have been extracted using first-order shear deformation theory (FSDT), and an analytical solution has been applied to extract critical buckling loads. Accordingly, the system of partial differential equations has been solved via separation of variables using Fourier expansion and power series method. The effects of the number of layers, lamination sequences, semi-vertex angles, shell thicknesses, shell lengths and boundary conditions on the stability of joined cones have been examined. For validation, the specific examples of present study have been compared to previous studies. Using ABAQUSE/CAE software (a FEM-based software), the results of finite element have been extracted. The present method is in good agreement with the finite element and other research results. Finally, the differences of classical shell theory (CST) of Donnell type and first-order shear deformation theory have been discussed for different shell thicknesses.*

**Keywords:** buckling, joined laminated conical shell, first-order shear deformation, power series

## Highlights

- The effect of shear deformation on the buckling of joined cross-ply laminated conical shells has been theoretically investigated.
- The usage of two joined conical shells instead of a single cone has been discussed.
- The critical buckling loads have been evaluated for various parameters of joined cones.
- The differences between FEM and analytical solution results have been expressed.
- The effects of different lamination sequences have been studied.
- The differences between CST and FSDT have been discussed for different shell thicknesses.

## 0 INTRODUCTION

Conical shells are structures with a broad spectrum of applications in many contexts including hydrocarbon storage tanks, refinery structures, cooling towers, body and interface of missiles, hull of aircrafts, nozzle of missiles and jet engines, liquid transmission pipelines and tankers, power plant structures, turbines and pressurized vessels, hull of submarines and various types of constructional structures and silos. In general, the strength of a shell highly depends on its form rather than its mass, so that the best structural result can be obtained by using minimal amounts of material. This high load-bearing capacity of shells has made them particularly useful.

In 1993, Leissa [1] compiled the proposed methods for analysing free vibration of isotropic conical shells under different boundary conditions. Tani and Yamaki [2] examined elastic stability of conical shells with simple and pinned supports under axial load. Regarding power series method, Tong [3] and [4] presented an exact solution method for the free vibration of thin and thick conical shells. Wu and Chiu [5] analysed the dynamic stability of composite conical shells under time-variable loading using the

perturbation theory. Using DSC method, Civalek [6] and Civalek and Ülker [7] studied free vibrations of circular panels and thin shells and compared their analytic results to experimental tests. Wisvantan et al. [8] studied the application of function approximation technique and spline method for analysing layered cylindrical and conical shells with variable thickness. They further studied vibrations of symmetric and asymmetric composite shells using the first-order shear deformation theory. The stability of functionally graded truncated conical shells under a periodic impulsive loading, non-uniform lateral pressure and combined loads was investigated by Sofiyev [9] and Sofiyev et al. [10] and [11]. The buckling of axially compressed conical and stiffened conical shells was studied by Spagnoli [12] and [13]. Ross et al. [14] and [15] studied inelastic and plastic buckling of thick-walled and ring-stiffened conical shells under external hydrostatic pressure.

Numerous papers have been proposed on the analysis of shells and plates. However, most of the previously cited studies were focused on the analysis of plates and cylindrical, spherical, and conical shells, with fewer resources available on joined shells. In their initial research works, Hu and Raney [16]

followed an experimental and analytical approach using finite element method (FEM) and modal test to determine mode shapes and natural frequencies of a joined cylinder-cone set. Rose et al. [17] analysed elastic wave function in a joined cylindrical-conical-cylindrical shell. Irie et al. [18] used a transformation matrix method to analyse free vibrations of joined conical-cylindrical shells. Tavakoli and Singh [19] utilized the space of state to present an Eigenvalue solution for joined shells. Flores and Godoy [20] studied post-buckling behaviour of conical-cylindrical and cylindrical-spherical shells. Performing different types of research, researchers [21] to [24] investigated the effects of axial, local, and concentrated loading on buckling and post-buckling behaviour of isotropic joined conical and cylindrical shells. They further analysed reinforced conical-cylindrical shells and studied the influence of reinforcement rings on buckling. Benjeddou [25] used Love's approximation theory for classic shells and considered finite-element strip elements to analyse joined conical-cylindrical shells. Dynamic instability of joined conical-cylindrical shells under periodic loading was examined via FEM by Kamat et al. [26]. Zhao [27] investigated, both theoretically and experimentally, the buckling of joined reinforced cylindrical and conical shells under internal compressive loading and particularly considered the effect of reinforcing rings.

Moreover, Caresta and Kessissoglou [28] studied the vibratory characteristics of joined isotropic conical and cylindrical shells; comparing Donnell's and Flügge's methods while employing power series method, they investigated free vibrations of the shells. They used FEM to verify their work. Niloufari et al. [29] investigated the effect of weld on buckling of joined conical-cylindrical shells. Among the latest research works on joined shells, one may refer to the analysis of free and forced vibrations of joined thin cylindrical-conical shells under various boundary conditions using Ritz-Fourier method by Ma et al. [30]. The linear and non-linear elastic buckling response of the conical panel is studied for a wide range of shell and stiffening parameters by means of an appropriate finite element model by Spagnoli and Chryssanthopoulos [31].

Many other research studies have been performed to present a finite element solution of shells. Rezaiee-Pajand et al. [32] to [34] develop a mixed interpolated formulation for nonlinear analysis of plates and shells using equivalent single layer (ESL) theory. They presented two triangular shell element having three and six nodes for geometrically nonlinear analysis of thin and thick shell structures. Also, they proposed

a geometrically nonlinear formulation for a six-node triangular shell element. Bucalem and Bathe [35] presented two mixed-interpolated general finite element methods for nonlinear analysis of a 9-node element and a 16-node element. Also, a formulation of general shell elements using mixed interpolation of tensorial components is discussed by Bathe and Dvorkin [36]. Petrolo and Carrera [37] and Li et al. [38] present a novel methodology to construct refined finite shell elements. An adaptable two-level mathematical refinement approach was proposed for refined curvilinear finite shell elements based on Carrera unified formulation (CUF). Schuß et al. [39] formulate a methodology to enforce interface conditions preserving higher-order continuity across the interface using isogeometric methods (IGA).

Considering the review of related previous research studies thus far, the stability analysis of joined conical shells under axial compression was studied using classical shell theory of Donnell type by Kouchakzadeh and Shakouri [40] and [41] and Shakouri and Kouchakzadeh [42]. Also, they presented an analytical solution for axisymmetric joined conical shells under axial compression and analysed free vibrations of cross-ply joined conical shells. They did not consider the effect of shear deformation on critical buckling loads and natural frequencies.

Furthermore, Shadmehri et al. [43] and [44] presented a first-order shear deformation shell theory to study buckling behaviour of a single composite conical and cylindrical shell. They used Ritz method and Levy type solution to study buckling under axial and bending loads. Sarkhail et al. [45] and [46] studied the free vibrations of a shell made of  $n$  cone segments joined together. Their governing equations were obtained by applying the classic Sanders type shell theory. Also, the shells were made from a linearly elastic isotropic homogeneous material. In the latest research studies, Izadi et al. [47] investigated analytical and FEM solutions on free vibration of joined cross-ply laminated conical shells using first-order shear deformation shell theory.

The literature survey reveals a clear indication that the studies on the joined shells are very few in numbers. Most of these research studies were about joined cylindrical-conical shells and limited to thin shells. Also, the used shell materials are frequently an elastic isotropic homogeneous material.

The goal of the present study is to investigate the buckling specifications of a joined conical shell under axial compression, considering the effects of shear deformation. Also, the conical shells are made from fibre-reinforced laminates. Hence, first-

order shear deformation theory is used to extract governing equations of two joined conical shells. An analytical solution based on Fourier expansion along the circumferential direction and power series method along the meridian direction is developed to separate variables of equilibrium equations and establish a system of eigenvalue problems. The continuity and boundary conditions are also applied to extract eigenvalues and examine the critical buckling loads of joined cones. The influences of the number of layers, lamination sequences, semi-vertex angles, shell thicknesses, shell lengths and boundary conditions on buckling load are examined as parametric studies.

1 METHODS

The coordinate system for two conical shells can be observed in Fig. 1. On this basis and first-order shear deformation theory FSDT, the displacement field for each conical shell is defined as follows:

$$\begin{aligned} u(s, \theta, z) &= U(s, \theta) + z\beta_s(s, \theta), \\ v(s, \theta, z) &= V(s, \theta) + z\beta_\theta(s, \theta), \\ w(s, \theta, z) &= W(s, \theta), \end{aligned} \tag{1}$$

where  $U$ ,  $V$ , and  $W$  refer to displacements of the middle surface along  $s$ -axis,  $\theta$ -axis, and normal to the surface, respectively, and  $\beta_s$  and  $\beta_\theta$  denote rotation changes of normal vector to middle surface around  $\theta$  and  $s$ -axes, respectively.

It should be mentioned that all relations are expressed for a single conical shell. The 1 and 2 indices in all parameters of Fig. 1 are referred to as the first and second cone, respectively. Furthermore, using FSDT, strain-displacement relationships for a single conical shell can be written as follows [44]:

$$\begin{aligned} \varepsilon_s &= \varepsilon_s^0 + z\kappa_s, \quad \varepsilon_\theta = \varepsilon_\theta^0 + z\kappa_\theta, \\ \gamma_{s\theta} &= \gamma_{s\theta}^0 + z\kappa_{s\theta}, \quad \gamma_{sz} = \gamma_{sz}^0, \quad \gamma_{\theta z} = \gamma_{\theta z}^0, \end{aligned} \tag{2}$$

where

$$\begin{aligned} \varepsilon_s^0 &= \frac{\partial U}{\partial x}, \quad \kappa_s = \frac{\partial \beta_s}{\partial s}, \quad \gamma_{sz}^0 = \beta_s + \frac{\partial W}{\partial s}, \\ \varepsilon_\theta^0 &= \frac{1}{R(s)} \left( U \sin \alpha + W \cos \alpha + \frac{\partial V}{\partial \theta} \right), \\ \gamma_{s\theta}^0 &= \frac{1}{R(s)} \left( \frac{\partial U}{\partial \theta} - V \sin \alpha \right) + \frac{\partial V}{\partial s}, \\ \kappa_\theta &= \frac{1}{R(s)} \left( \beta_s \sin \alpha + \frac{\partial \beta_\theta}{\partial \theta} \right), \\ \kappa_{s\theta} &= \frac{1}{R(s)} \left( \frac{\partial \beta_s}{\partial \theta} - \beta_\theta \sin \alpha \right) + \frac{\partial \beta_\theta}{\partial s}, \\ \gamma_{\theta z}^0 &= \frac{1}{R(s)} \left( \frac{\partial W}{\partial \theta} - V \cos \alpha \right) + \beta_\theta. \end{aligned} \tag{3}$$

In which  $\varepsilon_s$ ,  $\varepsilon_\theta$ ,  $\gamma_{s\theta}$ ,  $\gamma_{sz}$  and  $\gamma_{\theta z}$  represent the strains of each point of the shell. Also,  $\varepsilon_s^0$ ,  $\varepsilon_\theta^0$ ,  $\gamma_{s\theta}^0$ ,  $\gamma_{sz}^0$  and  $\gamma_{\theta z}^0$  are the strains of the middle surface of shell and  $\kappa_s$ ,  $\kappa_\theta$  and  $\kappa_{s\theta}$  are the curvatures of the middle surface of shell. In addition,  $R(s)$  is the curvature radius of each point on the conical shell and can be expressed as follows:

$$R(s) = R_0 + s \sin \alpha. \tag{4}$$

Below is the stress-strain relationship for the cross-ply joined composite conical shell [48]

$$\begin{aligned} \begin{Bmatrix} N \\ M \end{Bmatrix} &= \begin{bmatrix} [A] & [B] \\ [B] & [D] \end{bmatrix} \begin{Bmatrix} \varepsilon \\ \kappa \end{Bmatrix}, \\ \begin{Bmatrix} Q_{\theta\theta} \\ Q_{ss} \end{Bmatrix} &= K_s \begin{bmatrix} A_{44} & 0 \\ 0 & A_{55} \end{bmatrix} \begin{Bmatrix} \gamma_{\theta z}^0 \\ \gamma_{sz}^0 \end{Bmatrix}, \end{aligned} \tag{5}$$

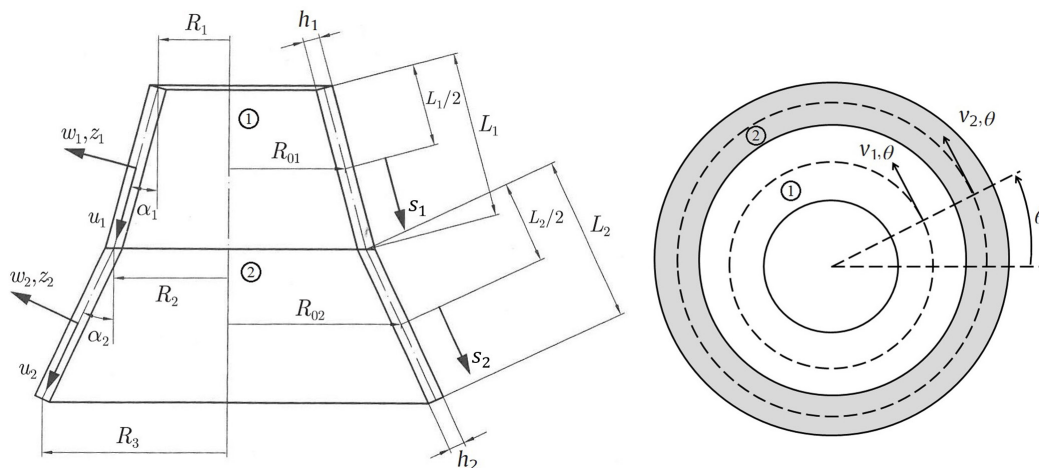


Fig. 1. Coordinate systems of two joined conical shells

where  $N$  and  $M$  are the force and moment resultants, which are expressed:

$$\begin{Bmatrix} N \\ M \end{Bmatrix} = \int_{-h/2}^{h/2} \begin{Bmatrix} \sigma \\ z\sigma \end{Bmatrix} dz, \quad (6)$$

moreover,

$$\begin{aligned} A_{ij} &= \sum_{k=1}^{N_k} (\bar{Q}_{ij})_k (z_{k+1} - z_k), \\ B_{ij} &= \frac{1}{2} \sum_{k=1}^{N_k} (\bar{Q}_{ij})_k (z_{k+1}^2 - z_k^2), \\ D_{ij} &= \frac{1}{3} \sum_{k=1}^{N_k} (\bar{Q}_{ij})_k (z_{k+1}^3 - z_k^3), \end{aligned} \quad (7)$$

in which  $k$  represents the  $k^{\text{th}}$  layer of laminated shell, and  $A_{ij}$ ,  $B_{ij}$  and  $D_{ij}$  are the laminated stiffness coefficients.

$$\begin{aligned} \bar{Q}_{11} &= Q_{11} \cos^4 \varphi + Q_{22} \sin^4 \varphi, \\ \bar{Q}_{12} &= Q_{12} (\cos^4 \varphi + \sin^4 \varphi), \\ \bar{Q}_{22} &= Q_{11} \sin^4 \varphi + Q_{22} \cos^4 \varphi, \\ \bar{Q}_{66} &= Q_{66} (\cos^4 \varphi + \sin^4 \varphi), \\ \bar{Q}_{44} &= Q_{44} \cos^2 \varphi + Q_{55} \sin^2 \varphi, \\ \bar{Q}_{55} &= Q_{55} \cos^2 \varphi + Q_{44} \sin^2 \varphi, \\ \frac{\nu_{12}}{E_1} &= \frac{\nu_{21}}{E_2}, \quad Q_{11} = \frac{E_1}{1 - \nu_{12}\nu_{21}}, \\ Q_{12} &= \frac{\nu_{12}E_2}{1 - \nu_{12}\nu_{21}}, \quad Q_{22} = \frac{E_2}{1 - \nu_{12}\nu_{21}}, \\ Q_{66} &= G_{12}, \quad Q_{44} = G_{23}, \quad Q_{55} = G_{13}, \end{aligned} \quad (8)$$

where  $\varphi$  is the fiber angle of laminated shell. The principle of minimum potential energy shall be derived as follows:

$$\delta(\hat{U} - \hat{W}_s - \hat{W}_e) = 0, \quad (9)$$

in which  $\hat{U}$  is the strain energy,  $\hat{W}_s$  is the work of body and surface forces and  $\hat{W}_e$  is the work of external loading. These parameters are presented as:

$$\begin{aligned} \delta\hat{U} &= \int_{\theta}^{\frac{L}{2}} \int_{-\frac{L}{2}}^{\frac{h}{2}} (\sigma_s \delta\varepsilon_s + \sigma_\theta \delta\varepsilon_\theta + \sigma_{s\theta} \delta\gamma_{s\theta} \\ &\quad + \sigma_{sz} \delta\gamma_{sz} + \sigma_{\theta z} \delta\gamma_{\theta z}) R d\theta ds dz, \\ \delta\hat{W}_s &= \int_{\theta}^{\frac{L}{2}} \int_{-L/2}^{L/2} (q_s \delta u + q_\theta \delta v - q_z \delta w) R d\theta ds, \\ \hat{W}_e &= \frac{1}{2} \int_{\theta}^{\frac{L}{2}} \int_{-L/2}^{L/2} \frac{1}{2} \hat{N} \left( \frac{\partial w}{\partial s} \right)^2 R d\theta ds, \end{aligned} \quad (10)$$

where  $\hat{N}$  is the in-plane compressive axial buckling force resultant. By integrating around the circumstances of one conical shell, the relation between the axial buckling load ( $P_{cr}$ ) and  $\hat{N}$  can be calculated as below:

$$\hat{N} = \frac{P_{cr}}{2\pi R \cos \alpha}. \quad (11)$$

By substituting the displacement field in strain-displacement and stress-strain relationships, the general form of equilibrium equations for each conical shell based on FSDT can be extracted in terms of  $U(s, \theta)$ ,  $V(s, \theta)$ ,  $W(s, \theta)$ ,  $\beta_s(s, \theta)$  and  $\beta_\theta(s, \theta)$  as follows:

$$[L] \{U, V, W, \beta_s, \beta_\theta\}^T = \{q\}. \quad (12)$$

$[L]$  is the matrix of the partial differential operators with partial derivatives with respect to  $s$  and  $\theta$ , given in the Appendix. Additionally, using integration by parts, hereby, following is the extracted general form of boundary conditions:

$$\begin{aligned} \int \{ (N_s - \bar{N}_s) \delta u + (M_s - \bar{M}_s) \delta \beta_s + (N_{s\theta} - \bar{N}_{s\theta}) \delta v \\ + (M_{s\theta} - \bar{M}_{s\theta}) \delta \beta_\theta + (Q_{ss} - \bar{Q}_{ss}) \delta w \} r d\theta. \end{aligned} \quad (13)$$

Upon this basis, various sets of boundary conditions were obtained from the above relationship, such as five boundary conditions at each end. Besides, at the interface of the two cones, displacements and forces would be equal; these continuity conditions ensure that all displacements and forces at the interface are equal; consequently, no distortion is possible at the interface (i.e., the connection is rigid).

Due to the satisfaction of the continuity constraint at the interface of the cones, relationships should be considered equally for the two cones in general and common coordinates. In this regard, the relationships for displacements and forces are equal along the cone's axis and normal to cone's axis then related to each other. Accordingly, continuity conditions at interface of the two shells are as follows.

$$\begin{aligned} U_1 \cos \alpha_1 - W_1 \sin \alpha_1 &= U_2 \cos \alpha_2 - W_2 \sin \alpha_2, \\ U_1 \sin \alpha_1 + W_1 \cos \alpha_1 &= U_2 \sin \alpha_2 + W_2 \cos \alpha_2, \\ V_1 = V_2, \quad \beta_{s1} = \beta_{s2}, \quad \beta_{\theta 1} = \beta_{\theta 2}, \\ N_{s1} \cos \alpha_1 - Q_{s1} \sin \alpha_1 &= N_{s2} \cos \alpha_2 - Q_{s2} \sin \alpha_2, \\ N_{s1} \sin \alpha_1 + Q_{s1} \cos \alpha_1 &= N_{s2} \sin \alpha_2 + Q_{s2} \cos \alpha_2, \\ N_{s\theta 1} = N_{s\theta 2}, \quad M_{s1} = M_{s2}, \quad M_{s\theta 1} = M_{s\theta 2}. \end{aligned} \quad (14)$$

2 SOLUTION METHOD

To solve the extracted equations, firstly, the Fourier expansions were performed along the circumferential direction as follows:

$$\begin{aligned}
 U(s, \theta) &= \bar{u}(s) \cos n\theta, & V(s, \theta) &= \bar{v}(s) \sin n\theta, \\
 W(s, \theta) &= \bar{w}(s) \cos n\theta, & & \\
 \beta_s(s, \theta) &= \bar{\beta}_s(s) \cos n\theta, & \beta_\theta(s, \theta) &= \bar{\beta}_\theta(s) \sin n\theta.
 \end{aligned}
 \tag{15}$$

Secondly, the solution of the problem along *s*-axis was considered in terms of a power series (PS):

$$\begin{aligned}
 \bar{u}(s) &= \sum_{m=0}^{\infty} a_m s^m, & \bar{v}(s) &= \sum_{m=0}^{\infty} b_m s^m, & \bar{w}(s) &= \sum_{m=0}^{\infty} c_m s^m, \\
 \bar{\beta}_s(s) &= \sum_{m=0}^{\infty} d_m s^m, & \bar{\beta}_\theta(s) &= \sum_{m=0}^{\infty} e_m s^m.
 \end{aligned}
 \tag{16}$$

Now, by substituting the above-mentioned series into Eq. (12) and sorting similar powers regarding *s*, one may end up with recursive relationships in terms of other coefficients. Using such relationships, one can obtain all constant coefficients in the series, except *a*<sub>0</sub>, *a*<sub>1</sub>, *b*<sub>0</sub>, *b*<sub>1</sub>, *c*<sub>0</sub>, *c*<sub>1</sub>, *d*<sub>0</sub>, *d*<sub>1</sub>, *e*<sub>0</sub>, *e*<sub>1</sub> as well. Therefore, these 10 coefficients shall be derived by applying the boundary conditions and continuity constraints on the joined shells. The boundary conditions used in the present paper as the following forms:

- Clamped(C):  $u = v = w = \beta_\theta = \beta_s = 0$ ,
- Simply-Supported(S):  $v = w = \beta_\theta = N_s = M_s = 0$ , (17)
- Free(F):  $N_s = M_s = N_{s\theta} = M_{s\theta} = Q_s = 0$ .

Evaluation of the above relationships for each conical shell under the boundary conditions and subject to the continuity conditions can be led to a system of 20 algebraic equations in terms of the coefficients of the series. By setting the determinant of coefficients matrix to zero, the value of critical buckling load for any given value of *n* can be extracted. For this purpose, 30 terms of power series have been used.

3 RESULTS AND DISCUSSION

First, the dimensionless buckling parameters are presented in Table 1 for cross-ply cylindrical shells. If  $\alpha_1$  and  $\alpha_2$  are equal to zero, the conical shells change to cylinders. So, the buckling load of structure can be compared to the buckling load of cylinders in other researches. Hence, the results of the present study have been compared to Khdeir et al. [49] as well as

Shadmehri et al. [43] studies. In Table 1,  $L/R=1$ ,  $h/R=0.1$ ,  $E_1/E_2=40$ ,  $\nu_{12}=0.25$ ,  $G_{23}=0.5E_2$  and  $G_{12}=G_{13}=0.6E_2$  have been assumed as the geometric and material properties of cylindrical shells. The present results are in good agreement with other research results.

**Table 1.** Dimensionless critical buckling parameters ( $\tilde{N} = \tilde{N}L^2 / (100 h^3 E_2)$ ) for cross-ply cylindrical shells

BC	Lamination sequences	CST& Levy [49]	FSDT& Levy [43]	Present FSDT & Present study
		Single shell	Single shell	Joined Shells
SS	[0/90/0]	0.2765	0.2813	0.2763
	[0/90]	0.1525	0.1670	0.1629
CC	[0/90/0]	0.4168	0.4197	0.4145
	[0/90]	0.2406	0.2508	0.2454
SC	[0/90/0]	0.3411	0.3452	0.3409
	[0/90]	0.1851	0.1969	0.1923

In continue, to come up with comparable results to other references, dimensionless buckling load is defined as follows:

$$\bar{P}_{cr} = P_{cr} / P_{cyl\infty}, \tag{18}$$

where  $P_{cr}$  is critical buckling load, denotes dimensionless buckling load, and  $P_{cyl\infty}$  is defined as follows [50]:

$$P_{cyl\infty} = \frac{2\pi E_1 h^2 \cos^2 \alpha}{\sqrt{3(1-\nu_{12}^2)}}. \tag{19}$$

To undertake comparisons, the results of two joined cones at identical semi vertex-angles are compared to a single conical shell.

Tong and Wang [51], Abediokchi et al. [52] and Sharghi et al. [53], using Donnell-type shell theory, present a procedure for buckling analysis of laminated conical shells. The composite considered in those researches is an asymmetrically cross-ply laminated shell made from carbon/epoxy.

$$\begin{aligned}
 E_2 &= 10 \text{ GPa}, & E_1/E_2 &= 40, \\
 \nu_{12} &= 0.25, & G_{12}/E_2 &= 0.5.
 \end{aligned}
 \tag{20}$$

The obtained results in Table 2 are for a constant thickness ratio of shells ( $h/R=0.01$ ) and different length of shells ( $L/R$ ), number of composite layers ( $N_L$ ) and semi-vertex angles ( $\alpha$ ), which falls within the scope of thin shells. The results are extracted for simply-supported boundary conditions at both ends. The results show a good agreement between the present and other results.

**Table 2.**  $\bar{P}_{cr}$  for S-S anti-symmetric laminated cross-ply conical shells ( $h/R = 0.01, \alpha = 45^\circ$ )

$L/R$	$N_L$	Tong and Wang [51]	Sharghi et al. [53]	Abediokchi et al. [52]	Present study
		CST & PS	CST & PS	CST & GDQ	FSDT & PS
0.2	2	0.1146(8)	0.1146(8)	0.1146(8)	0.1129(8)
	4	0.2488(7)	0.2487(7)	0.2488(7)	0.2438(7)
	6	0.2732(7)	0.2732(7)	0.2733(7)	0.2664(7)
	$\infty$	0.2927(7)	0.2927(7)	0.2927(7)	0.2857(7)
0.5	2	0.06751(6)	0.06735(6)	0.06734(6)	0.06581(6)
	4	0.1054(6)	0.1054(6)	0.1053(6)	0.1033(6)
	6	0.1117(5)	0.1117(5)	0.1117(5)	0.1079(5)
	$\infty$	0.1158(5)	0.1158(5)	0.1158(5)	0.1129(5)
1	2	0.06743(6)	0.06757(6)	0.06748(6)	0.06582(6)
	4	0.1063(5)	0.1065(5)	0.1064(5)	0.1036(5)
	6	0.1122(5)	0.1122(5)	0.1121(5)	0.1082(5)
	$\infty$	0.1165(5)	0.1165(5)	0.1165(5)	0.1118(5)

Table 3 demonstrates the results using FSDT by assuming identical thickness, length, and material for both cones. The non-dimensional critical buckling load of two joined cross-ply laminated conical shells is expressed for two orders of lamination sequences. As shown in Table 3, in all cases, the minimum values occurred when the lower shell is very similar to circular plate. The results illustrate that the order of lamination sequence is not very effective on the critical buckling load of joined asymmetrically cross-ply laminated shell. However, the use of [90, 0] lamination sequence obtains lower values than [0, 90].

Using the finite element (FE) and analytical methods, Table 3 presents the effects of the lamination

stacking sequence on the critical buckling load of joined cross-ply laminated cones. The finite element modelling is implemented using the finite element method (FEM)-based software (ABAQUS/CAE). As an appropriate choice, a 4-nodes element with 24 degrees of freedom (DOFs) for each element (three rotational and three translational DOFs at each node) is used for FE analyses. This type of element reveals the effect of FSDT. Also, the effects of mesh refinement and mesh convergence on the FEM solution have been surveyed. The percentage differences shown in Table 4, expresses the difference between FEM and analytical solution results.

The results indicate an acceptable amount of difference of approximately 1.2561% to 1.8484%. The effect of ordering of the layers on non-dimensional critical buckling load can be calculated with the following expression

$$LSD = \frac{\bar{P}_{cr[90]} - \bar{P}_{cr}}{\bar{P}_{cr[90]}} \times 100 \%, \quad (21)$$

where *LSD* stands for lamination sequence differences. As is obvious from Table 4, the values of the axial buckling loads are minimum for the single-layer [0], whereas single layer [90] values are maximum. The impact of the lamination sequence on the critical axial load increases when the number of [90] layers grows, especially in outer layers.

Fig. 2 investigates the influence of changes in  $\alpha_1$  on dimensionless buckling load.

**Table 3.** Non-dimensional buckling load ( $\bar{P}_{cr}$ ) for simply-supported laminated cross-ply conical shells ( $L/R = 0.1, h/R = 0.1$ )

$\alpha_1$	$\alpha_2$	[0, 90]			[90, 0]		
		$N_L$			$N_L$		
		2	4	Sym.	2	4	Sym.
0	0	0.2697	0.3749	0.3109	0.2650	0.3714	0.4101
	30	0.4030	1.0305	0.8455	0.3963	1.0217	1.1494
	60	0.2863	0.6916	0.6527	0.2805	0.6801	0.7718
	90	0.0049	0.0125	0.0167	0.0048	0.0124	0.0217
30	0	0.4355	1.0593	0.8523	0.4324	1.0502	1.1506
	30	0.2522	0.3507	0.2952	0.2438	0.3435	0.3805
	60	0.2673	0.6689	0.5763	0.2634	0.6643	0.7350
	90	0.0048	0.0126	0.0170	0.0047	0.0125	0.0221
60	0	0.2970	0.6831	0.6163	0.2871	0.6757	0.7821
	30	0.2715	0.6658	0.5410	0.2665	0.6519	0.7173
	60	0.1216	0.1690	0.1456	0.1155	0.1651	0.1799
	90	0.0047	0.0127	0.0171	0.0047	0.0126	0.0222

**Table 4.** Effects of lamination sequences on  $\bar{P}_{cr}$  for S-S cross-ply conical shells ( $\alpha_1=30^\circ$ ,  $\alpha_2=75^\circ$ ,  $N_L=4$ ,  $L/R_1=0.1$ ,  $h/R_1=0.1$ )

Stacking sequences	FEM	Present study	Difference [%]	LSD [%]
[0]	0.3491	0.3440	1.4609	83.594
[0/90/0]	0.3787	0.3717	1.8484	82.273
[0/0/90]S	0.4086	0.4022	1.5663	80.818
[0/90/0/90]	0.4427	0.4363	1.4457	79.192
[0/0/90/0]	0.6774	0.6689	1.2548	68.099
[0/0/90]	0.7482	0.7357	1.6707	64.913
[0/90/0]S	0.8290	0.8178	1.3510	60.998
[0/90/90]S	0.8859	0.8720	1.5690	58.413
[0/0/90/90]	0.9076	0.8962	1.2561	57.259
[0/90/90]	1.1197	1.1001	1.7505	47.534
[90/90/0]	1.1318	1.1138	1.5904	46.881
[90]	2.1319	2.0968	1.6464	-

As can be seen, with increasing the  $\alpha_2$  angle from negative values toward zero (cylindrical shell), the value of buckling load goes up, and given the short length of the shells, critical buckling load decreases abruptly as semi-vertex angles of the two shells get closer to one another. In other words, a sharp decrease in buckling load occurs when the semi-vertex angles come close together. If two joined conical shells have the same semi-vertex angles, one cone could be shaped with a longer length. Accordingly, the buckling of the longer cone under axial compression occurs sooner and critical buckling load decreases. Furthermore, the minimum buckling load varies with semi-vertex angles. Increasing the semi-vertex angles decreases the minimum buckling load.

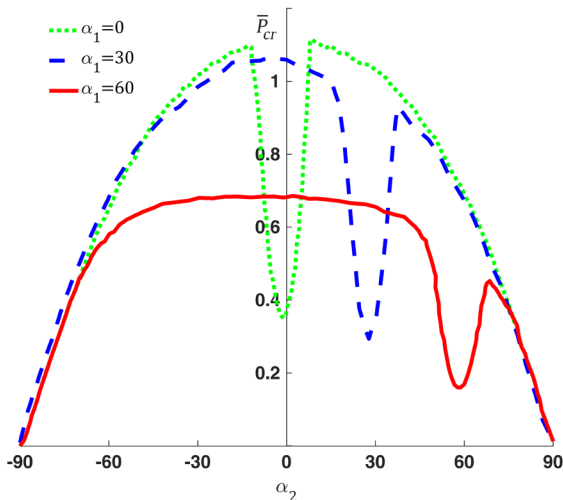


Fig. 2. Effect of changes in  $\alpha_1$  on buckling load ( $h/R_1=0.1$ ,  $N_L=4$ ,  $L/R_1=0.1$ )

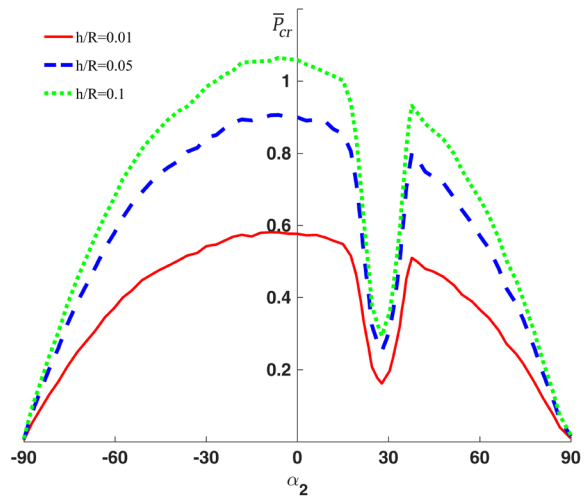


Fig. 3. Effect of changes in  $h/R_1$  ratio on buckling load ( $\alpha_1=30^\circ$ ,  $N_L=4$ ,  $L/R_1=0.1$ )

Fig. 3 demonstrate the effect of changes in  $L/R_1$  ratio at different values of semi-vertex angle that considers a case where  $\alpha_1=30^\circ$ ,  $L/R_1=0.1$ , and the number of layers is four. Upon increasing the  $h/R_1$  ratio, the value of the dimensionless buckling load increases.

In Fig. 4, the effects of variations in  $L/R_1$  on dimensionless buckling load have been shown.

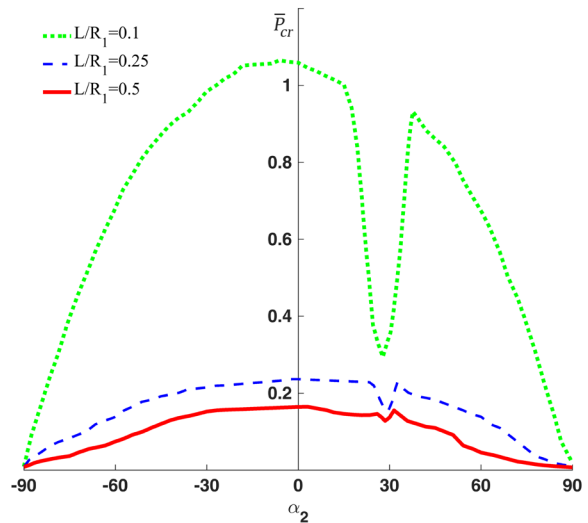


Fig. 4. Effect of changes in  $L/R_1$  ratio on buckling load ( $\alpha_1=30^\circ$ ,  $N_L=4$ ,  $L/R_1=0.1$ )

As mentioned before, in shorter shells, as semi-vertex angles of the two shells come closer to one another, a significant decrease occurs in buckling load; however, this rarely happens in longer shells.

Fig. 5 presents the influence of changes in  $N_L$  on a dimensionless buckling load. It is observed that the buckling load is very low in the case of being two layers. Due to the asymmetry of the shell at the low number of layers, it is rising by increasing the number of layers. Also, the minimum point changes by the number of layers and reaches to  $\alpha_2$ .

As shown in Fig. 6, for a special case, dimensionless buckling load was calculated for different thicknesses using classical shell theory (CST) of Donnell type based on the solution approach proposed by Shakoori and Kouchazadeh [31], and the obtained results were compared to those of the present research where FSDT was implemented.

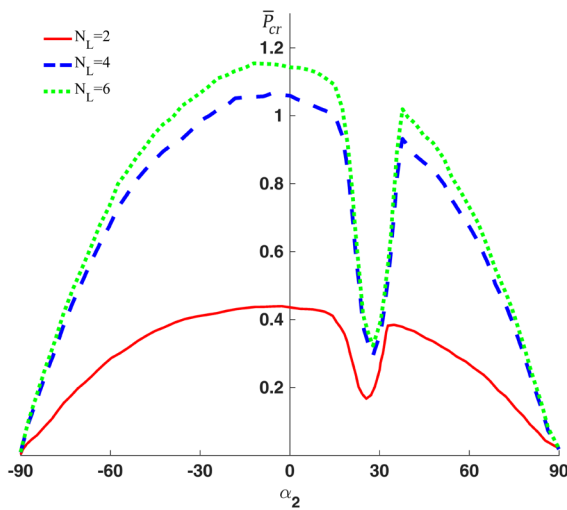


Fig. 5. Effect of changes in  $N_L$  on buckling load ( $h/R_1=0.1$ ,  $\alpha_1=30^\circ$ ,  $L/R_1=0.1$ )

As observed in Fig. 6, with increasing the thickness, the differences between classic theory and FSDT grow; i.e. the effects of shear force cannot be neglected, and the classic theory no longer provides acceptable results. The provoking point is that, in all cases, the results of FSDT are lower than those from the classic theory, and differences are presented even in the scope where the classic theory applies to thin shells ( $h/R_1 \leq 0.05$ ), although those can be neglected adequately.

Fig. 7 presents the influence of boundary conditions on dimensionless buckling load. The value of dimensionless buckling load decreased as one moved from C-C, S-C, F-C and S-S to F-S state. The clamped condition at each end of shell raises the value of dimensionless buckling loads because of the increasing rigidity of the structure.

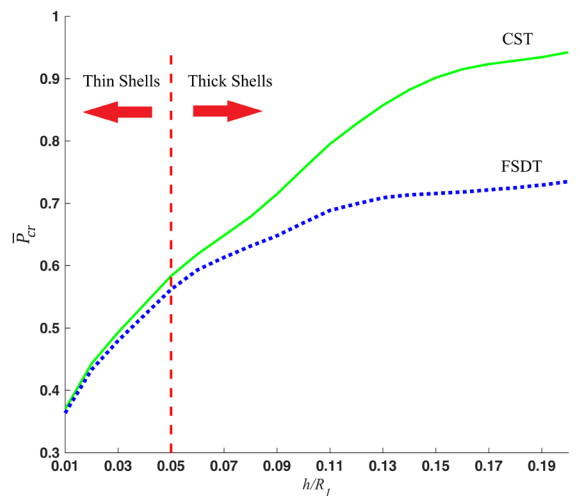


Fig. 6. Comparison between the results of classic theory and FSDT at different thicknesses

The results reveal that the value of  $\bar{P}_{cr}$  in simply-supported conditions is slightly near to free conditions. In addition, it is necessary to explain that the critical buckling loads decrease abruptly when two joined conical shell have the same semi-vertex angles in all boundary conditions.

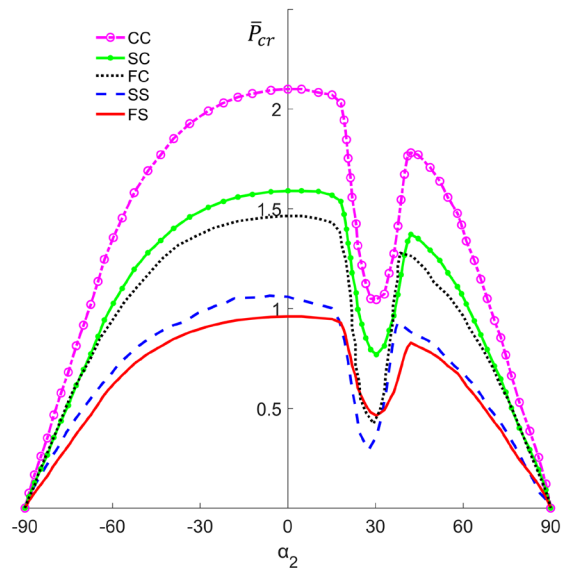


Fig. 7. Effect of boundary conditions on buckling load ( $\alpha_1=30^\circ$ ,  $L/R_1=0.1$ ,  $h/R_1=0.1$ )

#### 4 CONCLUSIONS

In this research, the buckling of two joined composite conical shells has been investigated using FSDT and CST, and the following general conclusions have been achieved. Effect of shear deformation is

negligible in thin shells. In thick shells; however, the results will be considerably different from real values in which shear deformation is ignored.

In all cases, the results of FSDT are lower than those of classic theory, and differences are present even in the scope where the classic theory applies to thin shells ( $h/R \leq 0.05$ ), though those can be neglected adequately. Therefore, the usage of classic shell theory is not suggested in thick shells.

A sharp decrease in buckling load occurs where the semi-vertex angles come close together. In other words, in shorter shells, as semi-vertex angles of the two shells come closer to each other, buckling load decreases at a high rate. In conclusion, it is highly recommended to use two joined shells with appropriate semi-vertex angles instead of a single cone.

In thin shells, the highest rigidity of the structure occurs at nearly identical semi-vertex angles. However, in thicker shells, the rigidity of shells from thickness is more effective than semi-vertex angle of the shells resulted from geometry. Finally, the minimum buckling load occurs when the lower shell is very similar to plate.

## 5 REFERENCES

- [1] Leissa, A.W. (1993). *Vibration of shells*. US Government Printing Office, Washington D.C., Acoustical Society of America, Originally issued by NASA 1973.
- [2] Tani, J., Yamaki, N. (1970). Buckling of truncated conical shells under axial compression. *AIAA Journal*, vol. 8, no. 3, p. 568-571, DOI:10.2514/3.5709.
- [3] Tong, L. (1993). Free vibration of composite laminated conical shells. *International Journal of Mechanical Sciences*, vol. 35, no. 1, p. 47-61, DOI:10.1016/0020-7403(93)90064-2.
- [4] Tong, L. (1993). Free vibration of orthotropic conical shells. *International Journal of Mechanical Science*, vol. 31, no. 5, p. 719-733, DOI:10.1016/0020-7225(93)90120-J.
- [5] Wu, C.-P., Chiu, S.-J. (2002). Thermally induced dynamic instability of laminated composite conical shells. *International Journal of Solids and Structures*, vol. 39, no. 11, p. 3001-3021, DOI:10.1016/S0020-7683(02)00234-2.
- [6] Civalek, Ö. (2005). Geometrically nonlinear dynamic analysis of doubly curved isotropic shells resting on elastic foundation by a combination of harmonic differential quadrature-finite difference methods. *International Journal of Pressure Vessels and Piping*, vol. 82, no. 6, p. 470-479, DOI:10.1016/j.ijpvp.2004.12.003.
- [7] Civalek, O., Ulker M. (2005). HDQ-FD integrated methodology for nonlinear static and dynamic response of doubly curved shallow shells. *Structural Engineering and Mechanics*, vol. 19, no. 5, p. 535-550, DOI:10.12989/sem.2005.19.5.535.
- [8] Viswanathan, K.K., Aziz, Z.A., Javed, S., Yaacob, Y., Pullepu, B. (2015). Free vibration of symmetric angle ply truncated conical shells under different boundary conditions using spline method. *Journal of Mechanical Science and Technology*, vol. 29, no. 5, p. 2073-2080, DOI:10.1007/s12206-015-0428-z.
- [9] Sofiyev, A.H. (2004). The stability of functionally graded truncated conical shells subjected to aperiodic impulsive loading. *International Journal of Solids and Structures*, vol. 41, no. 13, p. 3411-3424, DOI:10.1016/j.ijsolstr.2004.02.003.
- [10] Sofiyev, A.H., Zerín, Z., Korkmaz, A. (2008). The stability of a thin three-layered composite truncated conical shell containing an FGM layer subjected to non-uniform lateral pressure. *Composite Structures*, vol. 85, no. 2, p. 105-115, DOI:10.1016/j.compstruct.2007.10.022.
- [11] Sofiyev, A.H., Alizada, A.N., Akin, Ö., Valiyev, A., Avcar, M., Adiguzel, S. (2012). On the stability of FGM shells subjected to combined loads with different edge conditions and resting on elastic foundations. *Acta Mechanica*, vol. 223, no. 1, p. 189-204, DOI:10.1007/s00707-011-0548-1.
- [12] Spagnoli, A. (2001). Different buckling modes in axially stiffened conical shells. *Engineering Structures*, vol. 23, no. 8, p. 957-965, DOI:10.1016/S0141-0296(00)00112-7.
- [13] Spagnoli, A. (2003). Koiter circles in the buckling of axially compressed conical shells. *International Journal of Solids and Structures*, vol. 40, no. 22, p. 6095-6109, DOI:10.1016/S0020-7683(03)00369-x.
- [14] Ross, C.T.F., Sawkins, D., Johns, T. (1999). Inelastic buckling of thick-walled circular conical shells under external hydrostatic pressure. *Ocean Engineering*, vol. 26, no. 12, p. 1297-1310, DOI:10.1016/S0029-8018(98)00066-3.
- [15] Ross, C.T.F., Little, A.P.F., Adeniyi, K.A. (2005). Plastic buckling of ring-stiffened conical shells under external hydrostatic pressure. *Ocean Engineering*, vol. 32, no. 1, p. 21-36, DOI:10.1016/j.oceaneng.2004.05.007.
- [16] Hu, W.C.L., Raney, J.P. (1976). Experimental and analytical study of vibrations of joined Shells. *AIAA Journal*, vol. 5, no. 5, p. 976-980, DOI:10.2514/3.4111.
- [17] Rose, J.L., Mortimer, R.W., Blum, A. (1973). Elastic-wave propagation in a joined cylindrical-conical-cylindrical shell. *Experimental Mechanics*, vol. 13, no. 4, p. 150-156, DOI:10.1007/BF0322668.
- [18] Irie, T., Yamada, G., Muramoto, Y. (1984). Free vibration of joined conical-cylindrical shells. *Journal of Sound and Vibration*, vol. 95, no. 1, p. 31-9, DOI:10.1016/0022-460X(84)90256-6.
- [19] Tavakoli, M.S., Singh, R. (1989). Eigen solutions of joined/hermetic shell structures using the state space method. *Journal of Sound and Vibration*, vol. 130, no. 1, p. 97-123, DOI:10.1016/0022-460X(89)90522-1.
- [20] Flores, F.G., Godoy, L.A. (1991). Post buckling of elastic cone-cylinder and sphere-cylinder complex shells. *International Journal of Pressure Vessels and Piping*, vol. 45, no. 2, p. 237-258, DOI:10.1016/0308-0161(91)90095-J.
- [21] Zhao, Y., Teng, J.G. (2003). A stability design proposal for cone-cylinder intersections under internal pressure. *International Journal of Pressure Vessels and Piping*, vol. 80, no. 5, p. 297-309, DOI:10.1016/S0308-0161(03)00048-6.
- [22] Teng, J.G. (1996). Elastic buckling of cone-cylinder intersection under localized circumferential compression. *Engineering Structures*, vol. 18, no. 1, p. 41-48, DOI:10.1016/0141-0296(95)00114-3.

- [23] Teng, J.G., Barbagallo, M. (1997). Shell restraint to ring buckling at cone-cylinder intersections. *Engineering Structures*, vol. 19, no. 6, p. 425-431, DOI:10.1016/S0141-0296(96)00087-9.
- [24] Teng, J.G., Ma, H.-W. (1999). Elastic buckling of ring-stiffened cone-cylinder intersections under internal pressure. *International Journal of Mechanical Sciences*, vol. 41, no. 11, p. 1357-1383, DOI:10.1016/S0020-7403(98)00097-6.
- [25] Benjeddou, A. (2000). Vibration of complex shells of revolution using B-spline finite elements. *Computers and Structures*, vol. 74, no. 4, p. 429-440, DOI:10.1016/S0045-7949(99)00060-7.
- [26] Kamat, S., Ganapathi, M., Patel, B.P. (2001). Analysis of parametrically excited laminated composite jointed conical-cylindrical shells. *Computers and Structures*, vol. 79, no. 1, p. 65-76, DOI:10.1016/S0045-7949(00)00111-5.
- [27] Zhao, Y. (2005). Buckling behavior of imperfect ring-stiffened cone-cylinder intersections under internal pressure. *International Journal of Pressure Vessels and Piping*, vol. 82, no. 7, p. 553-564, DOI:10.1016/j.ijpvp.2005.01.008.
- [28] Caresta, M., Kessissoglou, N.J. (2010). Free vibrational characteristics of isotropic coupled cylindrical-conical shells. *Journal of Sound and Vibration*, vol. 329, no. 6, p. 733-751, DOI:10.1016/j.jsv.2009.10.003.
- [29] Niloufari, A., Showkati, H., Maali, M., Mahdi Fatemi S. (2014). Experimental investigation on the effect of geometric imperfections on the buckling and post buckling behavior of steel tanks under hydrostatic pressure. *Thin-Walled Structures*, vol. 74 p. 59-69, DOI:10.1016/j.tws.2013.09.005.
- [30] Ma, X., Jin, G., Xiong, Y., Liu, Z. (2014). Free and forced vibration analysis of coupled conical-cylindrical shells with arbitrary boundary conditions. *International Journal of Mechanical Sciences*, vol. 88, p. 122-137, DOI:10.1016/j.ijmecsci.2014.08.002.
- [31] Spagnoli, A., Chryssanthopoulos, M.K. (1999). Elastic buckling and postbuckling behaviour of widely-stiffened conical shells under axial compression. *Engineering Structures*, vol. 21, no. 9, p. 845-855, DOI:10.1016/S0141-0296(98)00036-4.
- [32] Rezaiee-Pajand, M., Arabi, E., Masoodi, A.R. (2018). A triangular shell element for geometrically nonlinear analysis. *Acta Mechanica*, vol. 229, no. 1, p. 323-342, DOI:10.1007/s00707-017-1971-8.
- [33] Rezaiee-Pajand, M., Masoodi, A.R., Arabi, E. (2018). On the shell thickness-stretching effects using seven-parameter triangular element. *European Journal of Computational Mechanics*, vol. 27, no. 2, p. 163-185, DOI:10.1080/17797179.2018.1484208.
- [34] Rezaiee-Pajand M., Arabi E., Masoodi A.R. (2019). Nonlinear analysis of FG-sandwich plates and shells. *Aerospace Science and Technology*, vol. 87, p. 178-189, DOI:10.1016/j.ast.2019.02.017.
- [35] Bucelem M.L., Bathe, K.J., (1993). Higher-order MITC general shell elements. *Numerical Methods in Engineering*, vol. 36, no. 21, p. 3729-3754, DOI:10.1002/nme.1620362109.
- [36] Bathe, K.J., Dvorkin, E.N. (1986). A formulation of general shell elements-the use of mixed interpolation of tensorial components. *Numerical Methods in Engineering*, vol. 22, no. 3, p. 697-722, DOI:10.1002/nme.1620220312.
- [37] Petrolo, M., Carrera, E. (2019). Best theory diagrams for shell finite elements. *AIAA SciTech Forum*, DOI:10.2514/6.2019-1765.
- [38] Li, G., Carrera, E., Cinefra, M., de Miguel, A.G., Pagani, A., Zappino, E. (2019). An adaptable refinement approach for shell finite element models based on node-dependent kinematics. *Composite Structures*, vol. 210, p. 1-19, DOI:10.1016/j.compstruct.2018.10.111.
- [39] SchuB, S., Dittmann, M., Wohlmuth, B., Klinkel, S., Hesch, C. (2019). Multi-patch isogeometric analysis for Kirchhoff-Love shell elements. *Computer Methods in Applied Mechanics and Engineering*, vol. 349, p. 91-116, DOI:10.1016/j.cma.2019.02.015.
- [40] Shakouri, M., Kouchakzadeh, M.A. (2013). Stability analysis of joined isotropic conical shells under axial compression. *Thin-Walled Structures*, vol. 72, p. 20-27, DOI:10.1016/j.tws.2013.06.012.
- [41] Kouchakzadeh, M.A., Shakouri, M. (2015). Analytical solution for axisymmetric buckling of joined conical shells under axial compression. *Structural Engineering and Mechanics*, vol. 54, no. 4, p. 649-664, DOI:10.12989/sem.2015.54.4.649.
- [42] Shakouri, M., Kouchakzadeh, M.A. (2014). Free vibration analysis of joined conical shells: Analytical and experimental study. *Thin-Walled Structures*, vol. 85, p. 350-358, DOI:10.1016/j.tws.2014.08.022.
- [43] Shadmehri, F., Hoa, S.V., Hojjati, M. (2012). Buckling of conical composite shells. *Composite Structures*, vol. 94, no. 2, p. 787-792, DOI:10.1016/j.compstruct.2011.09.016.
- [44] Shadmehri, F., Hoa, S.V., Hojjati, M. (2014). The effect of displacement field on bending, buckling, and vibration of cross-ply circular cylindrical shells. *Mechanics of Advanced Materials and Structures*, vol. 21, no. 1, p. 14-22, DOI:10.1080/15376494.2012.677102.
- [45] Sarkheil, S., Foumani, M.S., Navazi, H.M. (2016). Theoretical and experimental analysis of the free vibrations of a shell made of n cone segments joined together. *Thin-Walled Structures*, vol. 108, p. 416-427, DOI:10.1016/j.tws.2016.08.022.
- [46] Sarkheil, S., Foumani, M.S., Navazi, H.M. (2017). Free vibrations of a rotating shell made of p joined cones. *International Journal of Mechanical Sciences*, vol. 124-125 p. 83-94, DOI:10.1016/j.ijmecsci.2017.02.003.
- [47] Izadi, M.H., Hosseini-Hashemi, S., Korayem, M.H. (2018). Analytical and FEM solutions for free vibration of joined cross-ply laminated thick conical shells using shear deformation theory. *Archive of Applied Mechanics*, vol. 88, no. 12, p. 2231-2246, DOI:10.1007/s00419-018-1446-y.
- [48] Reddy, J.N. (2004). *Mechanics of Laminated Composite Plates and Shells: Theory and Analysis*, CRC Press, Boca Raton.
- [49] Khdeir A.A., Reddy, J.N., Frederick, D. (1989). A study of bending, vibration and buckling of cross-ply circular cylindrical shells with various shell theories. *International Journal of Engineering Science*, vol. 27, no. 11, p. 1337-1351, DOI:10.1016/0020-7225(89)90058-X.
- [50] Seide, P. (1956). Axisymmetrical buckling of circular cones under axial compression. *Journal of Applied Mechanics*, vol. 23, no. 4, p. 625-628.
- [51] Tong, L., Wang, T.K. (1992). Simple solutions for buckling of laminated conical shells. *International Journal of Mechanical*

Sciences, vol. 34, no. 2, p. 93-111, DOI:10.1016/0020-7403(92)90076-S.

- [52] Abediokhchi, J., Kouchakzadeh, M.A., Shakouri, M. (2013). Buckling analysis of cross-ply laminated conical panels using GDQ method. *Composites Part B: Engineering*, vol. 55, p. 440-446, DOI:10.1016/j.compositesb.2013.07.003.
- [53] Sharghi, H., Shakouri, M., Kouchakzadeh, M.A. (2016). An analytical approach for buckling analysis of generally laminated conical shells under axial compression. *Acta Mechanica*, vol. 227, no. 4, p. 1181-1198, DOI:10.1007/s00707-015-1549-2.

6 APPENDIX

The partial differential operators:

$$L_{11} = A_{11}\partial_{ss} + \frac{A_{11}\sin\alpha}{R(s)}\partial_s - \frac{A_{22}\sin^2\alpha}{R^2(s)} + \frac{A_{33}}{R^2}\partial_{\theta\theta},$$

$$L_{12} = \frac{A_{12} + A_{33}}{R(s)}\partial_{s\theta} - \frac{(A_{22} + A_{33})\sin\alpha}{R^2(s)}\partial_{\theta},$$

$$L_{13} = \frac{A_{12}\cos\alpha}{R(s)}\partial_s - \frac{A_{22}\sin\alpha\cos\alpha}{R^2(s)},$$

$$L_{14} = B_{11}\partial_{ss} + \frac{B_{11}\sin\alpha}{R(s)}\partial_s - \frac{B_{22}\sin^2\alpha}{R^2(s)} + \frac{B_{33}}{R^2}\partial_{\theta\theta},$$

$$L_{15} = \frac{(B_{12} + B_{33})}{R(s)}\partial_{s\theta} - \frac{(B_{22} + B_{33})\sin\alpha}{R^2(s)}\partial_{\theta},$$

$$L_{21} = \frac{(A_{12} + A_{33})}{R(s)}\partial_{s\theta} + \frac{(A_{22} + A_{33})\sin\alpha}{R^2(s)}\partial_{\theta},$$

$$L_{22} = A_{33}\left[\partial_{ss} + \frac{\sin\alpha}{R(s)}\partial_s - \frac{\sin^2\alpha}{R^2(s)}\right] + \frac{A_{22}}{R^2(s)}\partial_{\theta\theta} - \frac{A_{44}\cos^2\alpha}{R^2(s)},$$

$$L_{23} = \frac{(A_{22} + A_{44})\cos\alpha}{R^2(s)}\partial_{\theta},$$

$$L_{24} = \frac{(B_{12} + B_{33})}{R(s)}\partial_{s\theta} + \frac{(B_{22} + B_{33})\sin\alpha}{R^2(s)}\partial_{\theta},$$

$$L_{25} = B_{33}\left[\partial_{ss} + \frac{\sin\alpha}{R(s)}\partial_s - \frac{\sin^2\alpha}{R^2(s)}\right] + \frac{B_{22}}{R^2(s)}\partial_{\theta\theta} + \frac{A_{44}\cos\alpha}{R(s)},$$

$$L_{31} = -\frac{A_{12}\cos\alpha}{R(s)}\partial_s - \frac{A_{22}\sin\alpha\cos\alpha}{R^2(s)},$$

$$L_{32} = -\frac{(A_{22} + A_{44})\cos\alpha}{R^2(s)}\partial_{\theta},$$

$$L_{33} = A_{55}\left[\partial_{ss} + \frac{\sin\alpha}{R(s)}\partial_s\right] + \frac{A_{44}}{R^2(s)}\partial_{\theta\theta} - \frac{A_{22}\cos^2\alpha}{R^2(s)} + \frac{P_{cr}}{2\pi R(s)\cos\alpha}\partial_{ss},$$

$$L_{34} = \left(A_{55} - \frac{B_{12}\cos\alpha}{R(s)}\right)\partial_s + \frac{A_{55}\sin\alpha}{R(s)} - \frac{B_{22}\sin\alpha\cos\alpha}{R^2(s)},$$

$$L_{35} = \left(\frac{A_{44}}{R(s)} - \frac{B_{22}\cos\alpha}{R^2(s)}\right)\partial_{\theta},$$

$$L_{41} = B_{11}\partial_{ss} + \frac{B_{11}\sin\alpha}{R(s)}\partial_s - \frac{B_{22}\sin^2\alpha}{R^2(s)} + \frac{B_{33}}{R^2(s)}\partial_{\theta\theta},$$

$$L_{42} = \frac{(B_{12} + B_{33})}{R(s)}\partial_{s\theta} - \frac{(B_{22} + B_{33})\sin\alpha}{R^2(s)}\partial_{\theta},$$

$$L_{43} = -\left(A_{55} - \frac{B_{12}\cos\alpha}{R(s)}\right)\partial_s - \frac{B_{22}\sin\alpha\cos\alpha}{R^2(s)},$$

$$L_{44} = D_{11}\partial_{ss} + \frac{D_{11}\sin\alpha}{R(s)}\partial_s - \frac{D_{22}\sin^2\alpha}{R^2(s)} + \frac{D_{33}}{R^2(s)}\partial_{\theta\theta} - A_{55},$$

$$L_{45} = \frac{(D_{12} + D_{33})}{R(s)}\partial_{s\theta} - \frac{(D_{22} + D_{33})\sin\alpha}{R^2(s)}\partial_{\theta},$$

$$L_{51} = \frac{(B_{12} + B_{33})}{R(s)}\partial_{s\theta} + \frac{(B_{22} + B_{33})\sin\alpha}{R^2(s)}\partial_{\theta},$$

$$L_{52} = B_{33}\left[\partial_{ss} + \frac{\sin\alpha}{R(s)}\partial_s - \frac{\sin^2\alpha}{R^2(s)}\right] + \frac{B_{22}}{R^2(s)}\partial_{\theta\theta} + \frac{A_{44}\cos\alpha}{R(s)},$$

$$L_{53} = -\left(\frac{A_{44}}{R(s)} - \frac{B_{22}\cos\alpha}{R^2(s)}\right)\partial_{\theta},$$

$$L_{54} = \frac{(D_{12} + D_{33})}{R(s)}\partial_{s\theta} + \frac{(D_{22} + D_{33})\sin\alpha}{R^2(s)}\partial_{\theta},$$

$$L_{55} = D_{33}\left[\partial_{ss} + \frac{\sin\alpha}{R(s)}\partial_s - \frac{\sin^2\alpha}{R^2(s)}\right] + \frac{D_{22}}{R^2(s)}\partial_{\theta\theta} - A_{44}.$$

# Study of Influential Parameters of the Sphere Indentation Used for the Control Function of Material Properties in Forming Operations

Roman Satošek<sup>1</sup> – Michal Valeš<sup>2</sup> – Tomaž Pepelnjak<sup>1,\*</sup>

<sup>1</sup>University of Ljubljana, Faculty of Mechanical Engineering, Slovenia

<sup>2</sup>Czech Technical University in Prague, Faculty of Mechanical Engineering, Czech Republic

*The uncertainties of modern, adaptable sheet metal forming systems are classified into model errors and disturbances. To improve the control of production, disturbances in the forming process need to be reduced. For this purpose, a new data flow system was introduced. It connected the data flow of all influencing material parameters into the "material property control function". To control on-line the forming production line and acquire necessary material data, an indentation test was implemented. The main parameters to follow in this test are pile-up or sink-in values after the embossing of the ball-shaped tool into the material where the innovative approach of fully anisotropic material description was used. To set-up an optimal indentation test, parametric studies were performed with material data of AW 5754-H22. Finite element simulations were used to evaluate the influences of indenter diameter, contact friction and forming history of used the material. Fully anisotropic material behaviour was considered. Novel to this approach were a) the linking of the linear correlation of pile-up with the indentation depth described by gradient  $k$ , and b) the linking of gradient  $k$  with different pre-strains by a new power function.*

**Keywords:** indentation test, anisotropy, on-line control system, forming process, parametric study

## Highlights

- A new set-up of the control function influenced by the material properties, which is intended for the direct control of the sheet metal-forming production process via on-line indentation testing.
- Influential parameters of indentation testing at different indentation depths shows following scientific innovations:
  - The pile-up effect is dominant when the spherical indenter is embossed into AW 5754-H22.
  - A linear relationship exists between pile-up and indentation depth at different indenter diameters, in which the pile-up value has a smaller gradient in the case of a bigger indenter diameter and vice versa.
  - If no elastic region exists under indentation, the observed relationship between indenter diameter and pile-up value is not linear.
  - The relationship between Coulomb friction coefficient  $\mu$  and pile-up value expresses larger values of the linear gradient at a smaller value of friction coefficient  $\mu$ .
  - A linear relationship exists between the pile-up and indentation depth at various values of normal anisotropy. Examining the cold roller anisotropic material, it was found that the pile-up at  $\theta = 45^\circ$  has the nearest slope to the isotropic one while at  $\theta = 0^\circ$  the slope is increased and, vice versa, at  $\theta = 90^\circ$  it is lower as in the case of isotropic material..
- The most important contribution to the research of indentation is a novel definition of power function correlations among strain hardening, anisotropy and pile-up.

## 0 INTRODUCTION

The autonomous operation of modern metal-forming processes is essential. An appropriate response of the flexible sheet metal forming lines can only be provided if the properties of the incoming material can be identified online. All deviations of the finished part from the design are coming from the uncertainties of the forming process. Allwood et al. [1] have described in an overview paper of this research field those uncertainties in metal forming processes and divided them into model errors and disturbances. According to this classification, the model errors include all process design errors (necessary forces, friction, etc.) while disturbances include all those uncertainties that are not included in model errors

(variations in input material thickness, equipment vibration, temperature differences, differences in the material forming properties, etc.). One of the major goals in designing modern metal forming processes is to have the majority of all influential parameters described as model errors and to minimize the amount of disturbances. To follow major goals in designing the modern metal forming processes, we need to move uncertainties caused by the changes of metal forming properties from disturbance to model errors. This transition can be made with the implementation of the indentation test.

A spherical indentation test is commonly used for determining the hardness of the material. However, with special approaches, we can also make evaluations with its constitutive properties, fracture toughness,

\*Corr. Author's Address: University of Ljubljana, Faculty of Mechanical Engineering, Aškerčeva 6, 1000 Ljubljana, Slovenia, tomaz.pepelnjak@fs.uni-lj.si

residual stresses, and creep properties. The indentation test is classified as a non-destructive [2] or quasi-non-destructive [3] localized test that can be used for non-standard specimens. Indentation test is a simple test but extracting the aforementioned properties from a specimen is far from easy. The biggest challenge is non-uniform strain beneath the indenter. This paper evaluates the constitutive properties of the material based on the indentation test. Such evaluations with similar methods have been done by several authors [4] to [17], and they have used the strain-hardening coefficient  $n$  based on the Hollomon hardening power law (Eq. (1)).

$$\sigma_f = C \cdot \varepsilon_{e,p}^n, \quad (1)$$

where  $C$  and  $\varepsilon_{e,p}$  are Hollomon material constant and true equivalent plastic strain, respectively.

The first comprehensive study of the correlation between indentation test and material flow stress was done by Tabor [4], which proposed the proportionality between the mean contact pressure, the product of the flow stress, and the factor of the plastic material constant with values in the range between 2.6 and 3. Sonmez et al. [5] demonstrated analytical relations between hardness and strain for cold-forming parts. Their model requires only flow curve constants, which can be obtained through a simple compression test, and effective strain distribution, which can be obtained through a finite element (FE) analysis of the cold-forming process. Determining the plastic properties of the structural steel using spherical indentation with a reverse algorithm was studied by Pham et al. [6]. Fig. 1 shows geometrical relations between indenter and material's embossing during the indentation test. In the Fig. 1, the expansion cavity model (ECM) and the pile-up or sink-in effect are also presented. The basis of the ECM was set by Hill [7] based on Lamé's solution, while Johanson [8] added the relation of the mean contact pressure regarding the observed plastic strain. Pile-up and sink-in was investigated by Hill et al. [9] determining the so-called  $c^2$  function to relate the Hollomon hardening exponent and pile-up or sink-in effect. Yonezu et al. [10] proposed an indentation method to estimate the out-of-plane plastic anisotropy, with the aid of dimensional analysis and the representative strain concept. In their proposed method, the material is assumed to obey the work-hardening law and has out-of-plane anisotropy of plasticity governed by Hill's yield criterion. With the help of the finite element simulation. Taljat et al. [11] have shown that pile-up and sink-in during spherical indentation of elastoplastic materials

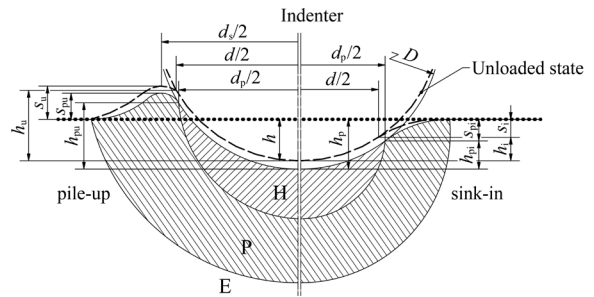


Fig. 1. Indentation test with ECM model: a pile-up, and sink-in

depend not only on the strain hardening exponent, but also on the relative amount of elastic and plastic deformation as characterized by the non-dimensional material parameter  $E/\sigma_f$ , the non-dimensional depth of penetration,  $h/(D/2)$ , and the friction coefficient. In Fig. 1, the horizontal dotted line represents the material condition before conducting the indentation test. The first step of the indentation test is the loading process. During this step, the force  $F$  to the indenter is applied (also known as contact force) which presses the indenter into the material. At indenter depth  $h_p$ , the equilibrium of forces is achieved. The contact edge between indenter and material define the projected contact diameter  $d_p$ . The next step is the material unloading where indenter moved upwards. Due to the elasticity of the indenter and material, the contact between them persists and can be measured with indenter force. At the separation, the contact force drops to the value of 0. The location of the indenter at this moment is marked in Fig. 1 by dashed lines. Now the indentation depth  $h$  and corresponding diameter  $d$  can be measured. During the penetration of the indenter into the material, material flows in the indenter's vicinity. If the extruded material forms a hill, then this is considered to be the pile-up ( $s_u$ ) effect. In the opposite situation, the phenomenon is described as "sink-in" ( $s_i$ ) (Fig. 1). Pile-up (sink-in) is influenced by the area under the indentation that consists of three characteristic zones. The hydrostatic region (H) lies directly below the contact surface and is not subject to the plastic strain, but it significantly affects the plastic strain of the next region (P) being plastic deformed. The furthest distance from the indentation is the region being only elastically loaded (E).

With the indentation test, we can collect all needed input data ( $F$ ,  $d$  or  $d_p$ ,  $h$  or  $h_p$ ,  $s_u$  or  $s_i$ ) to define the material properties. If the material property is assumed to be isotropic, then the true stress versus true equivalent plastic strain ( $\sigma_f - \varepsilon_{e,p}$ ) curve is obtained

from the indenter force versus indenter depth diagram ( $F-h_p$ ). This transformation was studied by Karthik et al. [12] and described in an ISO/TR 29381 standard [13]. The determination of the anisotropic material properties demands, additionally to the  $F-h_p$  curve, the measurement of the indentation-surrounding region, especially the areas with maximum pile-up (or sink-in) values. Yonezu et al. [10] have proposed a method with contour mapping on the indentation's surrounding area. Alternatively to this method, the residual imprint was introduced by Wang et al. [14]. Shen et al. [15] have demonstrated a novel method for measuring residual stresses both in uniaxial and biaxial stress states. Petryk et al. [16] developed a method to estimate the power-law hardening exponent of an anisotropic fcc single crystal from the spherical indentation test. The focus of their method was on residual pile-up/sink-in topography without the need to solve the relevant inverse problem afterwards. Wu et al. [17] used 3D roughness measurement equipment for scanning of the indentation's surrounding. For rolled materials used in sheet metal forming, Banabic [18] described the anisotropy as orthotropic, with the following orientations: longitudinal (rolling direction), transversal (perpendicular to rolling direction) and normal direction. The best way to describe this phenomenon is Langford  $r$ -values, which can be obtained by the uniaxial tension test [19]. During testing, force as well as strain in all three directions (longitudinal, transversal and normal) have to be acquired.

In the numerical program ABAQUS, a material's anisotropy can be described with Hill's yield criterion [17] and [20], as expressed in Eq. (2).

$$\sigma_f = \sqrt{\left( \begin{array}{l} F \cdot (\sigma_{22} - \sigma_{33})^2 + G \cdot (\sigma_{33} - \sigma_{11})^2 + \\ H \cdot (\sigma_{11} - \sigma_{22})^2 + 2 \cdot L \cdot \tau_{23}^2 + \\ 2 \cdot M \cdot \tau_{31}^2 + 2 \cdot N \cdot \tau_{12}^2 \end{array} \right)}, \quad (2)$$

where  $F, G, H, L, M$  and  $N$  are anisotropic parameters. They describe the current state of the anisotropy of used sheet metal material and are calculated as follows:

$$\begin{aligned} F &= \frac{1}{2} \cdot \left( \frac{1}{R_{22}^2} + \frac{1}{R_{33}^2} - \frac{1}{R_{11}^2} \right), & G &= \frac{1}{2} \cdot \left( \frac{1}{R_{33}^2} + \frac{1}{R_{11}^2} - \frac{1}{R_{22}^2} \right), \\ H &= \frac{1}{2} \cdot \left( \frac{1}{R_{11}^2} + \frac{1}{R_{22}^2} - \frac{1}{R_{33}^2} \right), & L &= \frac{3}{2 \cdot R_{23}^2}, \\ M &= \frac{3}{2 \cdot R_{13}^2}, & N &= \frac{3}{2 \cdot R_{12}^2}, \end{aligned} \quad (3)$$

where  $R$  are parameters of the stress ratios. In Eq. (3),  $R_{ii}$  are ratios of normal stresses while  $R_{ij}$  represent anisotropic yield ratios for shear stresses (Eq. (4)):

$$\begin{aligned} R_{11} &= \frac{\sigma_{11}}{\sigma_0}, & R_{22} &= \frac{\sigma_{22}}{\sigma_0}, & R_{33} &= \frac{\sigma_{33}}{\sigma_0}, \\ R_{12} &= \frac{\sigma_{12}}{\tau_0}, & R_{13} &= \frac{\sigma_{13}}{\tau_0}, & R_{23} &= \frac{\sigma_{23}}{\tau_0}, \end{aligned} \quad (4)$$

where  $\sigma_0$  is used normal stress considered as flow stress at the rolling direction implemented in the FE simulation and as the corresponding shear stress.

The majority of modern sheet metal-forming lines are automated and have several control functions [21] and [22] implemented into the production processes in order to assure quality of the products [1]. However, the spherical indentation test is a novel approach used for the on-line control of forming parameters directly on the production lines. Therefore, a new set-up of the control function data-flow presented in next chapter is to be determined. It has to be emphasized that the ball indentation, as known in various hardness testers, is the only design basis for the present study. The main purpose of the analyzed indentation here is entirely distinct from common hardness measurements.

## 1 DATA FLOW OF MATERIAL PROPERTY CONTROL FUNCTION (DFMCF)

The data flow control function necessary to implement the indentation test into the production line as on-line material control for evaluation of changes in material properties is presented in Fig. 2. The data flow is divided into three groups: *knowledge build-up*, *process set-up* and *control function generator*. Each of these groups includes one or more influential modules. The group *knowledge build-up* consists of *material property*, *material property database*, *forming process knowledge database*, *FE simulation*, and *FE database*. The *knowledge build-up* is external operation and can be done outside of the sheet metal-forming process. This paper concentrates mainly on the *FE simulation* module to evaluate material response to various indenter loads and influential parameters of this experiment. The topics presented in this paper are emphasised with orange blocks in Fig. 2. The main advantage in comparison to known close-loop controls of forming lines [1] is that other authors represent the control systems according to the measured results of the forming process itself while the main input parameters of the system presented in this paper are the material data. These material data

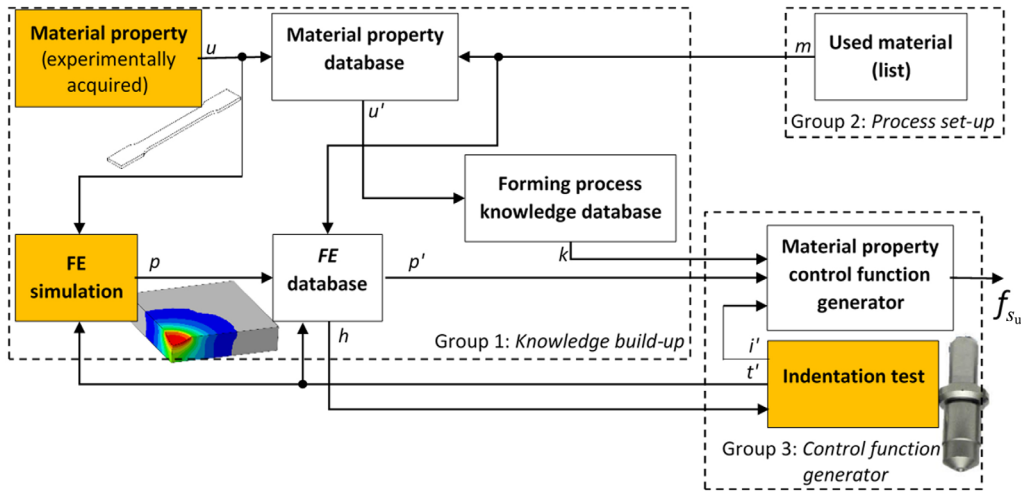


Fig. 2. Data flow for material properties control function at the forming process

are measured before the forming process, using the proposed indentation test. Such a concept is similar to some newly developed feed-forward control loops, as presented by Heingärtner et al. [23] however, the mechanical properties of the input material are not defined by the on-line measurements of those authors.

At the beginning of each production, the setting-up of the process is needed. During this period, all relevant equipment and necessary information (including the material's properties) have to be inserted into the sheet metal forming line. In DFMCF, the material properties are selected in the module *used material* in the *process set up* group. Inside of this module is the database with a list of all materials for which the relations between FE simulation and forming process knowledge is known. Output information from this module is material designation  $m$  (Fig. 2), and it goes into the *material property database* and *FE database*.

After material selection, all relevant data from the *forming process knowledge database* and *FE database* are transferred into the *control function generator* group. This group consists of *material property control function generator* and *indentation test*. The group is integrated into the sheet metal-forming process, and it is constantly active. The function of the *indentation test* is to emboss the indenter into the material and measure in case of analysed AW 5754-H22 the value of the pile-up. In this article, the influence of indenter diameter and material parameters on pile-up was studied. The main design rule for the indentation test is to find a suitable indenter diameter to obtain the highest pile-up value. However, the influence of the material thickness and coefficient of friction between

both objects in contact also has to be considered. The design rule is stored in the *FE database*, and, during setting-up, the process is transferred to the *indentation test* module as indentation design parameters  $h$  (Fig. 2). It can be observed that the pile-up value and gradient of it are small and so the immense challenge is how to measure the pile-up. This is even more complex in the case of anisotropic material properties. The output from the *indentation test* is indentation test parameter  $t'$  and pile-up measurement  $i'$  (Fig. 2). The pile-up measurement  $i'$  is plugged into the *material property control function generator* module. Other inputs for this module are *forming process knowledge database* and *FE database*. In the module *control function generator*, all inputs are compared. The output from the *control function generator* is control function (Fig. 2) being integrated into the control function of the sheet metal-forming process.

The *knowledge build-up* group can be run independently from the sheet metal forming process. The purpose of this group is to build-up knowledge about material properties, the relationship between material forming properties and embossing of the indenter, the relationship between material forming properties and forming processes, etc. The *knowledge build-up* consists of *material property*, *material property database*, *forming process knowledge base*, *FE simulation*, and *FE database* modules. The function of the *material property* module is to experimentally collect the data of material properties. In the present article, the uniaxial tension test was used. Data set  $u$  (Fig. 2) consist of Young's modulus, Poisson's ratios, flow curve  $\sigma_f - \varepsilon_{e,p}$ , Lankford's  $r$ -values, material thickness, material description.

2 MATERIALS AND METHODS

2.1 Material Data

In the *material property module* of the *knowledge build-up group* are included all needed experiments to describe the material-forming properties [24] and [25]. In the presented paper, the uniaxial tension test was conducted. The selected material is cold-rolled 3 mm thick strain-hardened sheet aluminium alloy AW 5754-H22 with basic mechanical properties (Table 1) in line with the standard EN 485-2 [26].

**Table 1.** The basic mechanical properties of the AW 5754-H22 [26]

$\rho$ [kg/m <sup>3</sup> ]	$E$ [GPa]	$R_{p0.2,min}$ [MPa]	$R_m$ [MPa]
2700	68	130	220 to 270

To obtain the true stress  $\sigma_f$  versus true plastic strain  $\epsilon_{e,p}$  relationship, we have conducted the uniaxial tension test according to ISO 6892-1 [27] for three typical rolling directions (0°, 45°, and 90°). The material was tested using an AMSLER universal testing machine with 30 kN nominal force, an Applied Measurement Systems transducer with 25 kN nominal load for force measurement, and optical strain data acquisition system. Since high strains are to be expected with ball indentation, the difference between the Hollomon and Swift hardening power laws was examined for the stress flow in the rolling direction. The maximum achieved values of tensile test at rolling direction 0° were for true stress 274.3 MPa at 0.108 true plastic strain, respectively. If we are using the Hollomon hardening power law (Eq. (1), then both parameters  $C$  and  $n$  are obtained by fitting the curve in  $\sigma_f-\epsilon_{e,p}$  diagram or using  $\log(\sigma_f)-\log(\epsilon_{e,p})$  approach [28]. In our case, the Hollomon power law (Eq. (1)) is not the best material hardening approximation. As an alternative to the Hollomon power law approximation, the Swift hardening power law can be used [29] (Eq. (5)):

$$\sigma_f = K \cdot (\epsilon_0 + \epsilon_{e,p})^{n_s}, \tag{5}$$

where  $K$  is Swift material constant,  $\epsilon_0$  pre-strain, and  $n_s$  hardening exponent, respectively. Those material parameters can be obtained by curve fitting. Tested aluminium alloy AW 5754-H22 has a good fit with Swift hardening power law with parameters listed in Table 2 therefore, in the present study, the Swift hardening power law was used.

However, the forming limit diagram, chemical composition, crystallographic composition, as well as thermal data, have to be considered in the extended version of this data set. The material property data set is stored in the *material property database* and also used as input for FE analyses. During setting-up of the process in *material property database* module, the collection of needed data according to selected material  $m$  is done, and this set of data is sent as selected material property data set  $u'$  (Fig. 2) to the *forming process knowledge base* module. This module is a storage for all relationships between material-forming properties and forming process parameters collected during the forming history, dedicated FE simulations, and other studies. Now that the selected material property data set  $u'$  is received into the *forming process knowledge base* module, the module collects proper forming relationship data and sent it as selected forming process parameter  $k$  (Fig. 2) to the *control function generator*. From the *knowledge build-up* module, the FE simulation data set  $p'$  (Fig. 2) is also going as input into the *material property control function generator* module. This data set is coming from *FE database* that store all FE simulation data. When material designation  $m$  (Fig. 2) comes into the *FE database* as input module collect needed data and sent into the *material property control function generator* module.

In the presented article, into the *FE simulation* module, the function to find the relationship between pile-up values and all influential parameters ( $D$ ,  $\mu$ ,  $s$ ,  $\sigma_f-\epsilon_{e,p}$ , Lankford's  $r$ -values) is included. The *FE simulation* module needs two parameters: material property data  $u$  and indentation test parameter  $t'$ . Material property data  $u$  is here needed for material and its thickness and indentation test parameter  $t'$  for boundary conditions of the FE simulation. In the first phase, the optimal indentation test is unknown. In this phase, the indenter diameter, its embossing speed, and support surface are determined. The second phase is dedicated to the evaluation of material influence at fixed parameters of the indentation test. Finally, the influence of contact friction is to be evaluated as well. In the literature overview, it was presented that material properties are determined by using  $F-h_p$  or/and  $s_u-h_p$  curves, and the main purpose of the FE simulations is to find the relationship between these curves and material properties. The output from the *FE simulation* module is the FE simulation data set  $p$  (Fig. 2).

**Table 2.** AW 5754-H22 forming parameters

Tested direction [°]	$K$ [MPa]	$\varepsilon_0$ [-]	$n_s$ [-]	$r$ [-]
0	403.4	0.009	0.174	0.565
45	383.4	0.009	0.171	0.677
90	383.2	0.007	0.163	0.794

## 2.2 FE Simulation

The second important module in the *knowledge build-up* group is the *FE simulation* module. To define the material parameters of the anisotropic materials with an indentation test, we need to analyse the material response under indenter load and define needed measurements after embossing the indenter into the material.

Each performed FE simulation [24] consists of geometry, mesh, material mechanical and formability properties, contact interactions between indenter and material, boundary conditions and applied load. The material parameters have already been discussed, and for the majority of the FE simulations, the isotropic material properties were used.

If the anisotropic material is simulated, Hill's potential function has to be considered (Eq. (2)).

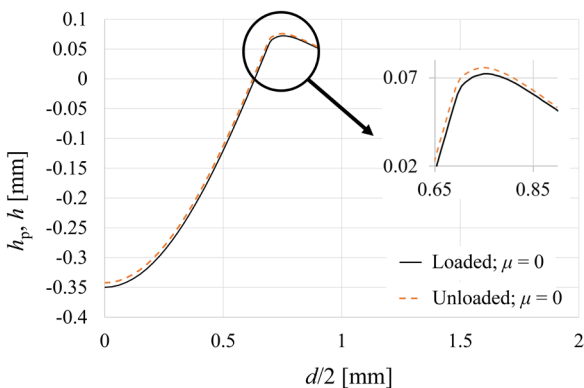


**Fig. 3.** Difference between loaded state ( $h_p$  versus  $d$ ) and unloaded state ( $h$  versus  $d$ ) at frictionless contact conditions ( $\mu = 0$ )

Preliminary FE simulations of the indentation were addressed to the understanding of material response under the indenter load. It was noticed that for aluminium alloy AW 5754-H22, the dominant effect is pile-up. FE simulation shows that at the unloaded state, the value of pile-up  $s_u$  is 5 % higher than in the loaded state (Fig. 3). On the other side, the pile-up diameter after unloading  $d_s$  is 1 % smaller in comparison to the loaded state. Furthermore, the

difference between indenter depth  $h_p$  and indentation depth  $h$  is only 2 %. Consequently, all our studies were validated to the amount of pile-up at the unloaded state, which will also can be measured in future research work.

### 2.2.1 Model, Mesh and Loads

The FE model of sheet metal during the indentation process was described with 3D elastic-plastic elements. To shorten the computer time required for the numerical FE simulation of the indentation test, a model symmetry with one-quarter of the entire analysed problem was used. For the majority of performed FE simulations, an indenter diameter of 1 mm and 3 mm thick AW 5754-H22 deformable sheet material was used. The cross-section with a size of 4.5 mm  $\times$  4.5 mm is sufficiently large that at maximum indenter depth  $h_p$  is an elastic region supporting the plastic one after the embossing with the indenter is present.

The selected mesh density has 79405 linear hexahedral (C3D8R) elements describing the elastic-plastic sheet metal while the indenter consists of 1852 linear quadrilateral (R3D4) and 10 linear triangular (R3D4) elements, respectively. The mesh size ranges from 0.007 mm  $\times$  0.007 mm  $\times$  0.01 mm to 0.2 mm  $\times$  0.2 mm  $\times$  0.2 mm.

Decreasing the numerical model of the indentation test to one quarter only [20] requires double-sided axis-symmetry (Fig. 4), which was used to shorten the computer calculation times. For the "x" symmetry (left surface of the model in Fig. 4), the surface nodes were fixed with movement restriction in "x" direction and rotation restrictions around "y" and "z" direction while for the "y" symmetry (front surface of the model in Fig. 4), the surface nodes were fixed with movement restriction in "y" direction and rotation restrictions around "x" and "z" direction. The bottom surface was fixed in the "z" direction to simulate the supporting surface. The indenter could move only in the "z" direction towards the top surface of the sheet metal with a speed of 0.05 mm/s, which is equal to the experimental indenter speed. At such speed, the static material behaviour can be assumed, neglecting the influence of the strain rate on material behaviour. Therefore, the strain rate-dependant material behaviour was not introduced into the simulation. Preliminary evaluations of the heat generated due to the work hardening and friction between the tool and the specimen have shown that the temperature rise at the adiabatic process as a worst case of heat generation during the forming does not

exceed 0.1 degrees. At the indentation speed of 0.05 mm/s, the heat conduction dominates the thermal state during the indentation, leading it towards isothermal conditions. Through this, the heat generation and corresponding temperature rise due to work hardening and friction among both objects in contact were neglected in the selected constitutive model.

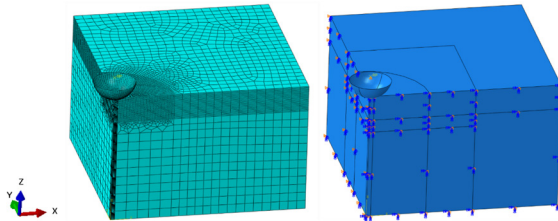


Fig. 4. Mesh and boundary conditions

### 3 EXPERIMENT

To design the *indentation test module* properly in the proposed *control function generator*, first the indentation test needs to be experimentally performed (Fig. 5). Through this, the indenter load for the selected AW 5754-H22 material at known tool displacements are to be acquired. These measurements are indispensable for the determination of the friction coefficient among both objects in contact. To indent the spherical shape into the AW 5754-H22 aluminium alloy, the LaborTech Lab Test 5.100SP1 100 kN uniaxial testing machine was used (Fig. 5a). The spherical indenter was mounted in a specially designed indentation tool, enabling the flexible mounting of different indenters. On both parts of the indentation tool, reflective tape was placed to enable the laser measurement of the indenter displacement in the vertical direction. The measurement was done with an LE-05 laser extensometer from Electronic Instrument Research the accuracy of this device is 1  $\mu\text{m}$ .

A Brinell spherical indenter with a 1 mm diameter was mounted into the indentation tool. A specimen of AW 5754-H22 aluminium alloy was polished with 3  $\mu\text{m}$  polishing paste to obtain an optimal flat measurement surface. After polishing, the specimen was placed into the indentation tool. During the indentation test, the indenter vertical speed was set to 50  $\mu\text{m/s}$ , while the tool's position was monitored with the laser extensometer. The initial contact between the spherical indenter and specimen was defined at the contact force of 5 N where the laser extensometer was set to 0. The selected indenter displacements for particular tests were from 100  $\mu\text{m}$  to 350  $\mu\text{m}$  with step

increments of 50  $\mu\text{m}$ . At this point, the force  $F$  acting on indenter and indentation depth  $h_p$  were acquired.

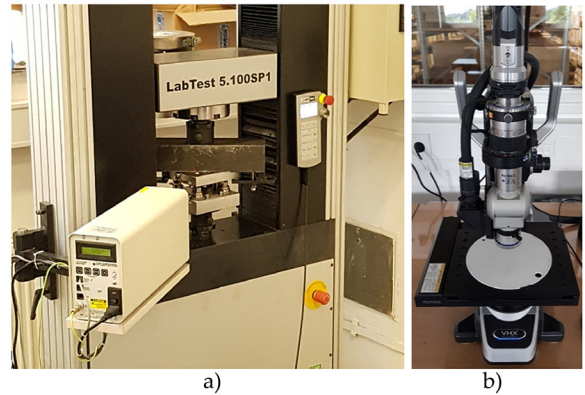


Fig. 5. Equipment used to perform a) indentation test, and b) measurement of the indentation

The formed cavity and its vicinity were measured with a Keyence VHX-6000 optical microscope (Fig. 5b). The microscope was set to 300 $\times$  magnification, and the samples were scanned with a pitch of 2  $\mu\text{m}$ . Based on the conducted measurement, the indentation depth  $h$  and pile-up value  $s_u$  were determined, and correlations with indenting forces were evaluated for further comparison with numerical results.

### 4 RESULTS AND DISCUSSION

The usability of the DFMCF depends on proper design of each module inside the groups of the DFMCF (Fig. 2). With the plotting of different diagrams and analyzing the corresponding correlations at the indentation process, its optimal set-up parameters were determined.

#### 4.1 Indenter Diameter $D$

The decision of the dimension and geometry of the indenter represents a crucial step in designing the indentation test. The sheet metal has stretched grain structure in the rolling direction, also known as textured grain structure. When the indentation test integration into the sheet metal forming process is analysed, the aim is to deform as many crystal grains as possible. It is not sufficient to evaluate the grain structure at the projected surface the size and shape on the material's cross-section are also important. The dimensions of the crystal grains define the minimal indenter diameter and its indenter depth while its maximal dimensions are limited by the material thickness. Fig. 6 shows the relationship between

pile-up and indentation depth for different indenter diameters at the material thickness of 3 mm. Four different indenter diameters ranging from 1.0 mm to 2.5 mm were numerically simulated. The influence of the thickness is measured by the curve deviation from the line. At straighter curves, lower influence can be expected, being the smallest in the case of linear correlation.

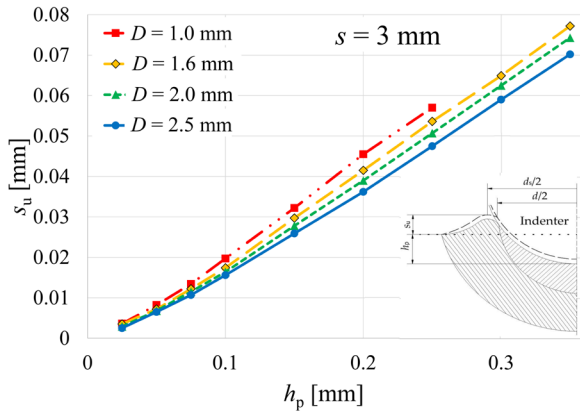


Fig. 6. Relations between the indenter diameter and the material thickness (s)

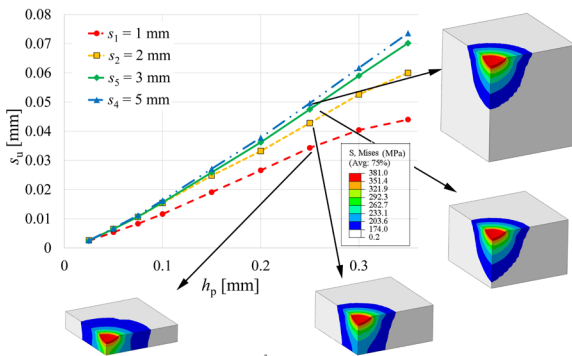


Fig. 7. Correlation of the indenter diameter versus material thickness (s) at diameter  $D = 2.5$  mm

To explain into the detail the behaviour of the material at indentation into different sheet thicknesses, the indentation diameter of 2.5 mm was selected. The diagram  $s_u-h_p$  (Fig. 7) was plotted at an unloaded state. Additional to the  $s_u-h_p$  relationship, von Mises stresses at loaded state are plotted (Fig. 7). To distinguish the difference between elastics and plastic regions, the minimum at the stress scale was set to yield stress of the observed AW 5754-H22 material.

The elastic region is shown as grey in Fig. 7, and the coloured area is the plastic region. At indenter depth of 0.25 mm, the elastic region of the sheet metal below the plastic one can be observed only in the case of 5 mm thick material. In the case of 1 mm thick

material, the curve on the diagram in Fig. 7 deviates from the line due to the fully plastic deformed sheet metal in the vicinity of the embossed shape across its entire thickness. However, the sheet thickness also influences the inclination of the observed line or curve. In the case of material thicknesses of 3 mm and 5 mm, the correlation is linear up to  $h_p = 0.35$  mm, and the difference between gradients of these lines are small. By decreasing the material thickness down to 1 mm and 2 mm, the plotted curve has a visible deviation from linear correlation and the inclination is smaller than in the case of the 3 mm thick material. The optimal value of indenter diameter at the dedicated material thickness and planned indenter depth is when these two rules are followed:

- The plotted trend line of the  $s_u-h_p$  relationship is linear at the observed thickness  $s_i$
- If the plotted trend line of the  $s_u-h_p$  relationship at  $s_{u,i}(s_i) \approx s_{u,i+1}(s_{i+1}) \approx s_{u,i+n}(s_{i+n})$  ( $s_{i+1}$  is thicker material) then the indenter diameter is selected properly.
- The difference among two consecutive lines at the observed value of the indenter depth  $h_p$  is less than the accuracy of used measurement equipment.

#### 4.2 Friction Coefficient

Syngellakis et al. [30] have analysed influence of friction coefficient on the pile-up effect however, they used a rotational-symmetric FE model and isotropic material, and they have analysed the influence of friction coefficient on one pile-up value only. The interaction between the friction coefficient and the pile-up as a function over a range of various indenter depths has not yet been found in the literature. Therefore, the friction influence on pile-up values at unloaded state has been numerically simulated for five different Coulomb friction coefficients ( $\mu=0, 0.05, 0.1, 0.2$  and  $0.45$ ). From the diagram in Fig. 8, it is evident that friction influences the pile-up value. Through all points of the diagram (Fig. 8) with the same friction coefficient, a line can be drawn. The relationship between friction coefficient and pile-up value results in an increase of pile-up at lower friction coefficients. Fig. 8 shows the values of pile-up regarding different friction coefficients with the values presented in Table 3, and at friction  $\mu=0.45$ , the pile-up value is 49 % lower as in the case of frictionless contact.

It can also be stated that friction has a similar effect on the pile-up or sink-in as the strain-hardening exponent. At frictionless contact, the pile-up or sink-in

effect is determined by the strain-hardening exponent. In the case of material delivering a dominant pile-up effect, the increase of friction coefficient diminishes, the pile-up and can shift it even towards the sink-in.

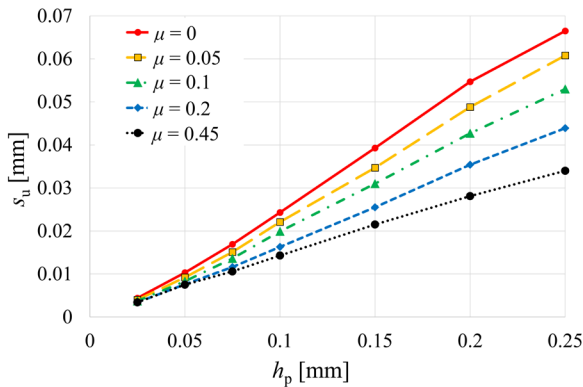


Fig. 8. Influence of the contact friction

Table 3. Different pile-up value at different coefficient of the friction

$h_p = 0.25 \text{ mm}$	$\mu = 0$	$\mu = 0.05$	$\mu = 0.1$	$\mu = 0.2$	$\mu = 0.45$
pile-up $s_u$ [mm]	0.0665	0.0608	0.0530	0.0439	0.0340

### 4.3 Experimental Calibration of Friction Coefficient $\mu$ Used in FE Models

The relationship between the force  $F$  acting on the indenter versus indenter depth  $h$  as well as value of the pile-up versus indentation depth  $h$  were plotted and presented in the discussion about FE indentation tests and experimentally obtained shapes of the cavities.

To determine the real friction among the indenter and the specimen, it is necessary to implement the measured values of force  $F$  and indenter depth  $h$  onto the calibration curves obtained with the FE simulations, as shown in the Fig. 9. The relationship  $F$  versus  $h$  shows that the measured values of indentation test fits well with the FE data using the friction coefficient of  $\mu=0.20$ . The so-defined coefficient of the friction is aligned with Trzepieciński and Lemu [31] and slightly lower value as defined by Duran [32]. The limiting values of the diagram in Fig. 9a are  $\mu=0.45$  and  $\mu=0.10$ , respectively. A slight deviation among the FE-obtained curves and experimental results, which may be caused due measurement accuracy of the used experimental equipment at low indentation depths, may be observed.

The same procedure was used for the  $s_u-h$  relationship (Fig. 9b). The comparison among numerical and experimental results also interact in this case at most for the friction coefficient of  $\mu=0.20$ .

Therefore, in the FE simulations described in chapters *Influence of the strain history of used material and Anisotropic material*, the coefficient of the friction with the value of  $\mu=0.20$  was selected.

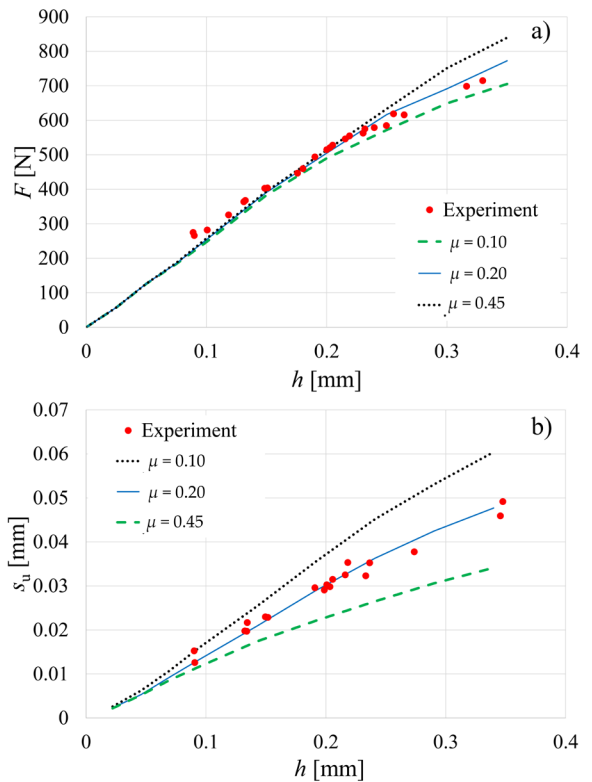


Fig. 9. Relationship between FE simulation and experiment: a) according to the  $F-h$  diagram and b) according to the  $s_u-h$  diagram both with various friction coefficients

### 4.4 Anisotropic Material

If we are simulating the indentation test of the isotropic material, all six Hill's ratios are equal to 1. Yonezu et al. [10] and Wu et al. [17] have analysed anisotropy of material in two perpendicular directions only ( $\sigma_0$  and  $\sigma_{90}$ ). They used in their simulations of the indentation test the material properties with five equal Hill's ratios having the value 1 and only the parameter  $R_{22}$  differed from 1. Considering the material's anisotropy, the Hill's ratios based on Lankford's coefficients are calculated according to Eq. (6) [33]. The remaining three Hill's ratios are equal to 1.

Taking into account the literature about the indentation test and how the anisotropy of the material is described with Hill's ratios, four different anisotropy descriptions were determined (Table 4): isotropic material, anisotropic material with  $R_{22}$  none-

equal to 1, and two anisotropic material with different parameters  $R_{22}$ ,  $R_{33}$  and  $R_{12}$ . The differences among anisotropic materials “II” and “III” are described below.

$$R_{22} = \sqrt{\frac{r_{90} \cdot (r_0 + 1)}{r_0 \cdot (r_{90} + 1)}}, \quad R_{33} = \sqrt{\frac{r_{90} \cdot (r_0 + 1)}{(r_0 + r_{90})}},$$

$$R_{12} = \sqrt{\frac{3 \cdot r_{90} \cdot (r_0 + 1)}{(2 \cdot r_{45} + 1) \cdot (r_0 + r_{90})}}. \quad (6)$$

**Table 4.** Hill’s ratios of selected materials\*

Name	$R_{22}$	$R_{33}$	$R_{12}$	Source
Iso	1	1	1	well known
Aniso I	1.254	1	1	[17]**
Aniso II	1.107	0.956	1.079	AW 5754-H22
Aniso III	1.077	1.017	1.198	[34]***

\* Ratios  $R_{11}$ ,  $R_{12}$  and  $R_{23}$  are in all cases equal to 1  
 \*\* Wu et al. [17] used bulk material  
 \*\*\* Inal et al. [34] analysed deep drawing process, not ball indentation

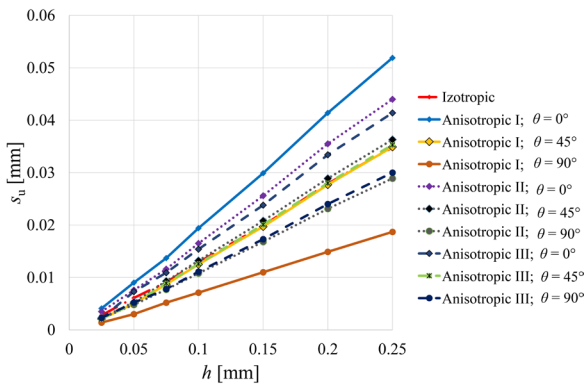


**Fig. 10.** Diagram  $s_u-h$  for different angles to rolling directions and with different anisotropic material properties

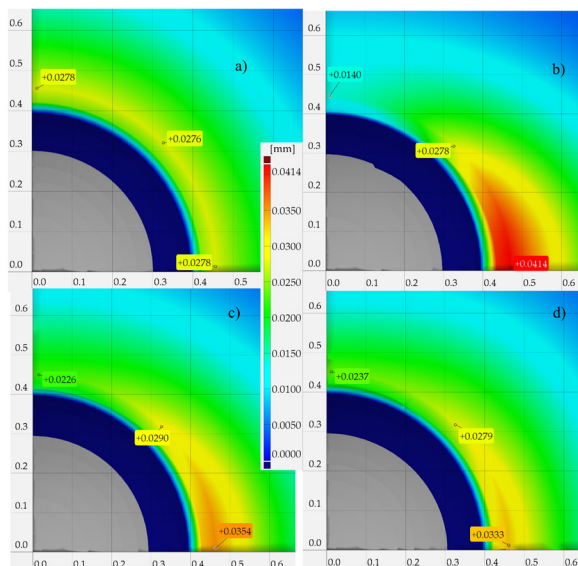


**Fig. 11.** Pile-up  $s_u$  for different materials: a) Iso, b) Aniso I, c) Aniso II and d) Aniso III

The differences among all four materials and, in particular, the influence of anisotropy on the level of the pile-up versus indentation depth were visualised with simulations of ball indentation, as shown in Figs. 10 and 11, respectively. For all simulations, Young’s modulus, Poisson’s ratio, density, coefficient of friction, and flow curve were fixed. The variable parameters among performed simulations are Hill’s ratios values, according to Table 4. In the case of material designated “aniso I”, anisotropic properties were taken from Wu et al. [17]. Hill’s ratios for the material “aniso II” is calculated from the set of anisotropic Lankford’s  $r$ -values  $r_0=0.565$ ,  $r_{45}=0.677$  and  $r_{90}=0.794$  being measured on actual AW-5754-H22 material. The material designated as “aniso III” is an example of rolled sheet metal [34] used for deep drawing. In this case, Lankford’s  $r$ -values are  $r_0=0.81$ ,  $r_{45}=0.58$ , and  $r_{90}=1.08$ . The main difference between the material “aniso III” and the material “aniso II” is the consecutive rising values of Lankford’s coefficients from  $r_0$  over  $r_{45}$  to  $r_{90}$  by the later one.

Fig. 11 shows pile-up value at indenter depth 0.2 mm and at different main direction  $\theta$ . Fig. 10 shows  $s_u-h$  relationships for all three main directions  $\theta=0^\circ$ ,  $\theta=45^\circ$ , and  $\theta=90^\circ$ . For isotropic material properties, the  $s_u-h$  relationships for all three main directions are aligned. The  $s_u-h$  relationships at  $\theta=45^\circ$  direction of “aniso I”, “aniso III” and the isotropic are aligned. In case of the “aniso II” material, the  $s_u-h$  curve is slightly higher regarding other lines at  $\theta=45^\circ$ . This may be caused due to the steadily increasing values of Lankford’s coefficients. Furthermore, with the material “aniso III”, the  $s_u-h$  relationships at  $\theta=0^\circ$  and  $\theta=90^\circ$  are not aligned with the  $\theta=45^\circ$  curve. Observing the gradients  $k$  of linear relationship in the  $s_u-h$  diagram (Fig. 10), the differences between  $k_0$  and  $k_{90}$  are the largest with material “aniso I”, while they are the smallest with the material “aniso III”..

#### 4.5 Influence of the Strain History of Used Material

To reduce disturbances defined by Allwood et al. [1] and to enable the feed-forward controls in a manner similar to those described by Heingärtner et al. [23] during sheet metal forming, the indentation test can

be used for the evaluation of the strain history of the material used, as represented in Fig. 12a. The light gray flow curve represents the material properties for annealed material (e.g. AW 5754-O condition) in the entire range from  $R_p$  to  $\sigma_{f100}$  reached at  $\varepsilon_{e,max}$ . After sheet metal rolling of such material, the initial value of flow stress  $R_p$  is raised to  $\sigma_{fi}$  (beginning of the continuous curve). The same flow stress changes are also expected to happen during the deep draw forming process however, the flow stress after the forming is  $\sigma_{fi+1}$  (end of the continuous curve). The values of flow stress at  $\sigma_{fi}$  are important for setting-up the forming process, while the stresses after the forming process and all subsequential forming operations can be digitally determined with FEM simulations. However, on automated production lines, the process uncertainties causing variation of material flow stress at particular part areas after the forming operation are to evaluate on-line in the future. For this purpose, the indentation test is to integrate into the process lines.

To understand the influential testing parameters and to design optimal indentation test, FE simulations of different pre-hardened material states were performed. As already discussed, for this study, the as-delivered AW 5754-H22 material is used. Therefore, the entire flow stress range  $\Delta\sigma_f$  from yield stress  $R_p = 174.9$  MPa up to true stress  $\sigma_f = 274.3$  MPa at  $\varepsilon_{e,max}$  (Eq.7) was experimentally acquired. In this step, each executed FE simulation was done with different starting true stress  $\sigma_{fi}$  (Eq.8) representing the rise of flow stress due to various cold rolling operation in the production of sheet metal. Index  $i$  is the percentage of flow stress range rise before the sheet metal forming stage where the values of  $i = 15\%$ ,  $30\%$ ,  $45\%$ ,  $60\%$ ,  $70\%$ , and  $85\%$  were used. For the purpose of analysis, the unknown pre-strain shifting of initial coordinate point of strain axis (virtual shift) as shown in Fig. 12b for the case of  $\varepsilon_{i45}$  is performed. Fig. 13 shows the  $\sigma_f$ - $\varepsilon_{e,p}$  flow curves of virtual pre-hardened material used in FE simulations of the indentation test compared to the flow curve of initial material.

$$\Delta\sigma_f = \sigma_{f100} - R_p, \quad (7)$$

$$\sigma_{fi} = R_p + i \cdot \Delta\sigma_f. \quad (8)$$

As mentioned, when defining material properties of the AW 5754-H22, the presented paper uses the Swift approximation power law due to better fitting of its material properties. Finally, no indentation test method considering the Swift hardening power law was found in the literature.

The indentation test at different forming steps  $i$  was simulated using the Swift hardening law. Since at

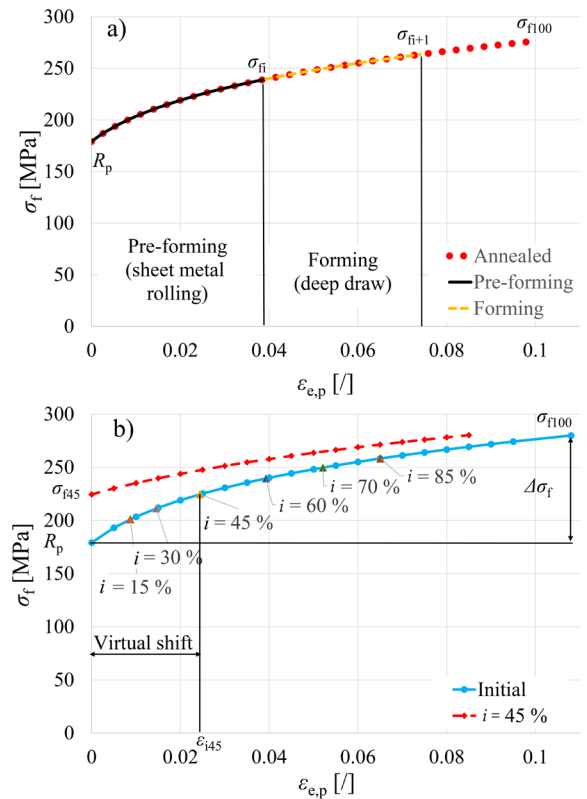


Fig. 12. Material property  $\sigma_f$ - $\varepsilon_{e,p}$  curve: a) production life cycle b) usage in FE simulation

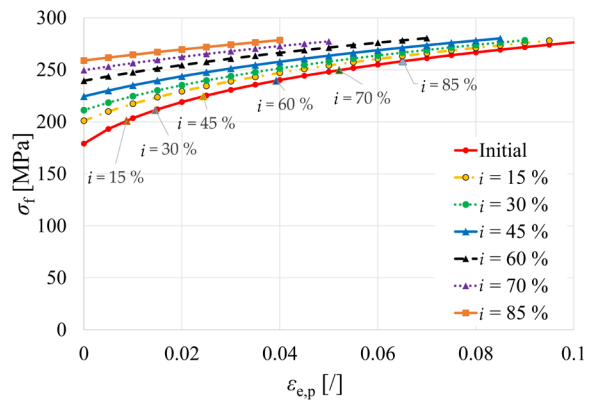


Fig. 13. Material property history described with  $\sigma_f$ - $\varepsilon_{e,p}$  curves

compression loading significantly higher strains can be reached prior to material failure, as in the case of tensile loading, the maximal plastic strain of the initial material in all FE simulations of indentation test were set to  $\varepsilon_{e,p,max} = 1$ . The  $s_u$  versus  $h$  correlations at rolling direction ( $\theta = 0^\circ$ ) obtained from FE simulations are presented in Fig. 14a. The maximum values of each obtained line correspond to the obtained value of selected maximal plastic strain. However, the factors

$i$  are connected to the percentage of pre-strain values presented in Fig. 14a for these pre-strain values, the maximal attainable plastic strain was decreased, as shown in Fig. 14a. It can be observed that the indenter depth depends on percentage  $i$  of the pre-strain, where at higher forming percentages  $i$  lower indentation depth  $h$  is reached. The present study shows that percentage of the pre-strain  $i$  increases the gradient of the linear correlation describing the  $s_u-h$  relationship (steeper slope). Fig. 14b is an example of the increased gradient of the  $s_u-h$  line due to the pre-strain difference between initial and  $i = 45\%$  pre-strained material. It is also evident that anisotropy does not influence the gradient increase if pile-up in different directions ( $\theta = 0^\circ$ ,  $\theta = 45^\circ$  and  $\theta = 90^\circ$ ) was observed (Fig. 14b).

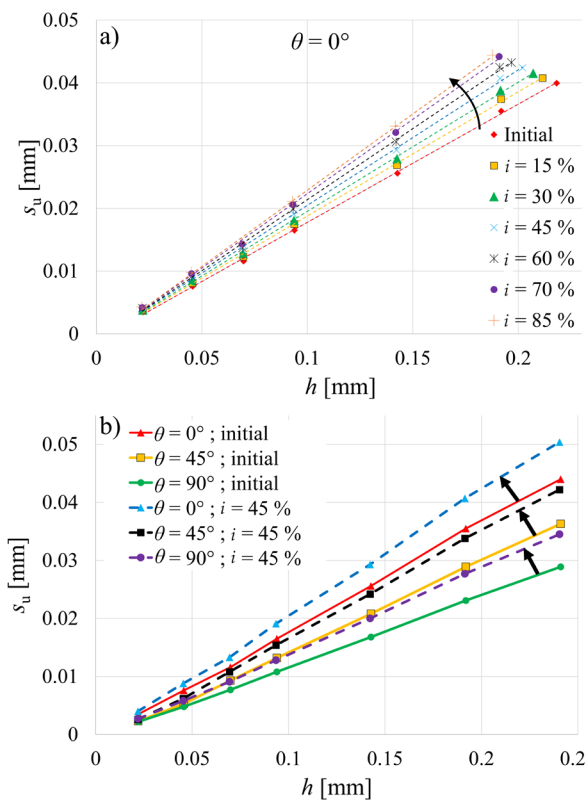


Fig. 14. Influence of strain history on ball indentation test a) complete pre-strain range and b) only initial and  $i = 45\%$

For each FE simulated set of data points at particular pre-strain, the linear trendline was approximated in order to obtain the parameters of linear correlation, and the gradient  $k$  was extracted. Fig. 15 presents the relationship between gradient  $k$  and pre-strain values. It is evident that the relationship  $k$  versus  $\varepsilon_{e,p}$  can also be described with a power

function. An entirely new correlation is introduced, as shown in the Eq. (9):

$$k = a \cdot (f_0 + \varepsilon_{e,p})^b, \quad (9)$$

where  $a$  is the constant of the introduced power function,  $f_0$  initial shift regarding the coordinate system and  $b$  the function's exponent. Particular parameters of the determined power function are shown in Table 5 for all three directions regarding the material rolling. The introduced function is valid for the AW 5754-H22 material and its generalization needs to be further analysed. However, this function can be introduced into the DFMCf system.

Table 5. Power function parameters

$\theta$ [°]	$a$ [-]	$f_0$ [-]	$b$ [-]
0	0.372	0.0214	0.186
45	0.339	0.0239	0.222
90	0.3	0.0211	0.242

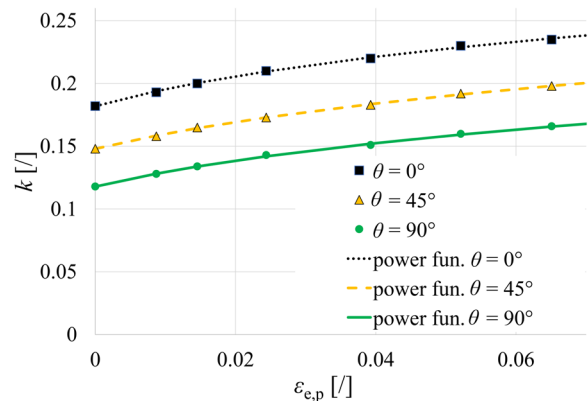


Fig. 15. Relations between the  $k$  (gradient of the linear trendline) and true strain  $\varepsilon_{e,p}$

## 5 CONCLUSIONS

The following conclusions can be stated from the presented study:

- To reduce disturbances (Allwood classification) in the sheet metal-forming process we, introduce the concept of *DFMCf* aimed for the feed-forward controls of sheet metal production lines. This data flow has three groups of modules among which one is designated as *knowledge build-up*. The present study focuses on the *FE simulation* module as a part of *knowledge build-up* group. If we are following the *material properties control function* data flow for FE simulation, the material properties have to be experimentally acquired. In the presented work, the uniaxial tension test for

aluminium alloy AW 5754-H22 was conducted and approximated with Swift hardening power law.

- b) The pile-up effect is influenced by indenter diameter  $D$  and corresponding indenter depth  $h_p$ . The combination of indenter diameter  $D$ , indenter depth  $h_p$  and material thickness  $s$  was analysed to select proper dimension  $D$  for experimental work, for which the existence of the elastic area under the indenter must be present. The relation between indenter depth  $h_p$  and the value of the pile-up  $s_u$  have to be linear for quality measurements. The slope of the linear relationship  $s_u-h_p$  depends on indenter diameter  $D$  its smaller value leads to a steeper line. In the case of the missing elastic area under the contact surface (e.g., when the material thickness  $s$  is too small), the relationship between indenter depth  $h_p$  and pile-up value  $s_u$  becomes non-linear, and the gradient of the curve starts to decrease. Material AW 5754-H22 with a thickness of  $s = 3$  mm and the indenter with diameter  $D = 1$  mm were selected for experimental verification.
- c) Friction has significant influence on the pile-up effect, and it decreases the pile-up value  $s_u$ . Therefore, for the numerical simulations a proper friction coefficient needs to be inserted into the FE models. Comparative analyses among FE simulations of the indentation process and experimental work have shown good fit for friction coefficient of  $\mu = 0.2$  being used for all consecutive numerical analyses.
- d) The anisotropic behaviour of material properties plays a significant role in pile-up mapping. In the case of anisotropic material, the pile-up values are directional dependent. Evaluating the relationship  $s_u-h$ , it was found that the pile-up at  $\theta = 45^\circ$  has the nearest slope to the isotropic one while at  $\theta = 0^\circ$  the slope is increased and, vice versa, at  $\theta = 90^\circ$  it is lower as in the case of isotropic material. In the future research work, the indentation test will be integrated into the sheet metal forming process, and the relation between pile-up values and Lankford's  $r$ -values will be determined.
- e) The forming history can be recorded with the indentation test shown on the case of aluminium alloy AW 5754-H22. Various material pre-strains caused by cold rolling deliver steeper  $s_u-h$  lines, and the target true equivalent plastic strain  $\varepsilon_{e,p}$  is reached at smaller indentation depth  $h$ .
- f) An entirely new correlation of the slope of the linear relationship of  $s_u$  versus  $h$  as a function of pre-strain was introduced, leading the AW 5754-

H22 material to the potential equation correlating the factors  $k$ ,  $\varepsilon_{e,p}$  and new introduced parameters  $a$ ,  $f_0$  and  $b$ .

- g) Further research work is oriented towards the design of an experiment to establish the connection between the *knowledge build-up* group and *control function generator* group and experimentally prove the presented on-line forming process feed-forward control function.

## 6 ACKNOWLEDGMENTS

This paper is part of research work within the program Nr. P2-0248 entitled Innovative Production Systems financed by the Slovene Ministry of Education, Science and Sport. The authors are very grateful for the financial support. The authors express also thanks to the CEEPUS programme, which enabled the authors' mobility in the frame of the network Nr. CEEPUS III - HR 0108.

## 7 REFERENCES

- [1] Allwood, J.M., Duncan, S.R., Cao, J., Groche, P., Hirt, G., Kinsey, B., Kuboki, T., Liewald, M., Sterzing, A., Tekkaya, A.E. (2016). Closed-loop control of product properties in metal forming. *CIRP Annals - Manufacturing Technology*, vol. 65, no. 2, p. 573-596, DOI:10.1016/j.cirp.2016.06.002.
- [2] Kim, M., Marimuthu, K.P., Lee, J.H., Lee, H. (2016). Spherical indentation method to evaluate material properties of high-strength materials. *International Journal of Mechanical Sciences*, vol. 106, p. 117-127, DOI:10.1016/j.ijmecsci.2015.12.008.
- [3] Schindler, H.-J. (2005). On quasi-non-destructive strength and toughness testing of elastic-plastic materials. *International Journal of Solids and Structures*, vol. 42, no. 2, p. 717-725, DOI: 10.1016/j.ijsolstr.2004.06.029.
- [4] Tabor, D. (2000). *The hardness of metals*. Clarendon Press.
- [5] Sonmez, F.O., Demir, A. (2007). Analytical relations between hardness and strain for cold formed parts. *Journal of Materials Processing Technology*, vol. 186, no. 1-3, p. 163-173, DOI:10.1016/j.jmatprotec.2006.12.031.
- [6] Pham, T.-H., Phan, Q.-M., Kim, S.-E., (2018). Identification of the plastic properties of structural steel using spherical indentation. *Materials Science and Engineering: A*, vol. 711, p. 44-61, DOI:10.1016/j.msea.2017.10.097.
- [7] Hill, R. (1998). *The Mathematical Theory of Plasticity*. Clarendon Press, Oxford.
- [8] Johnson, K.L. (1985). *Contact Mechanics*. Cambridge University Press, Cambridge.
- [9] Hill, R., Storakers, B., Zdunek, A. B. (1989). A Theoretical Study of the Brinell Hardness Test. *Proceedings of the Royal Society A Mathematical, Physical and Engineering Sciences*, vol. 423, p. 301-330, DOI:10.1098/rspa.1989.0056.
- [10] Yonezu, A., Tanaka, M., Kusano, R., Chen, X. (2013). Probing out-of-plane anisotropic plasticity using spherical indentation:

- A numerical approach. *Computational Materials Science*, vol. 79, p. 336-344, DOI:10.1016/j.commatsci.2013.05.020.
- [11] Taljat, B., Pharr, G.M. (2004). Development of pile-up during spherical indentation of elastic-plastic solids. *International Journal of Solids and Structures*, vol. 41, no. 14, p. 3891-3904, DOI:10.1016/j.ijsolstr.2004.02.033.
- [12] Karthik, V., Visweswaran, P., Bhushan, A., Pawaskar, D. N., Kasiviswanathan, K. V., Jayakumar, T., Raj, B. (2012). Finite element analysis of spherical indentation to study pile-up/sink-in phenomena in steels and experimental validation. *International Journal of Mechanical Sciences*, vol. 54, p 74-83, DOI:10.1016/j.ijmecsci.2011.09.009.
- [13] ISO / TR 29381.2008. *Metallic materials – Measurement of Mechanical Properties by an Instrumented Indentation Test – Indentation Tensile Properties*. International Organization for Standardization, Geneva.
- [14] Wang, M., Wu, J., Hui, Y., Zhang, Z., Zhan, X., Guo, R. (2017). Identification of elastic-plastic properties of metal materials by using the residual imprint of spherical indentation. *Materials Science and Engineering: A*, vol. 679, p. 143-154, DOI:10.1016/j.msea.2016.10.025.
- [15] Shen, L., He, Y., Liu, D., Gong, Q., Zhang, B., Lei, J. (2015). A novel method for determining surface residual stress components and their directions in spherical indentation. *Journal of Materials Research*, vol. 30, no. 8, p. 1078-1089, DOI:10.1557/jmr.2015.87.
- [16] Petryk, H., Stupkiewicz, S., Kucharski, S. (2017). On direct estimation of hardening exponent in crystal plasticity from the spherical indentation test. *International Journal of Solids and Structures*, vol. 112, p. 209-221, DOI:10.1016/j.ijsolstr.2016.09.025.
- [17] Wu, J., Wang, M., Hui, Y., Zhang, Z., Fan, H. (2018). Identification of anisotropic plasticity properties of materials using spherical indentation imprint mapping. *Materials Science and Engineering: A*, vol. 679, p. 143-154, DOI:10.1016/j.msea.2018.02.001.
- [18] Banabic, D. (2010). *Sheet Metal Forming Processes*. Springer, Berlin, Heidelberg.
- [19] Aleksandrović, S., Stefanović, M., Dragan, A., Lazić, V. (2009). Variation of normal anisotropy ratio "r" during plastic forming. *Strojniški vestnik - Journal of Mechanical Engineering*, vol. 55, no. 6, p. 392-399.
- [20] Starman, B., Vrh, M., Halilović, M., Štok, B. (2014). Advanced modelling of sheet metal forming considering anisotropy and young's modulus evolution. *Strojniški vestnik - Journal of Mechanical Engineering*, vol. 60, no. 2, p. 84-92, DOI:10.5545/sv-jme.2013.1349.
- [21] Gusel, L., Boskovic, V., Domitner, J., Ficko, M., Brezocnik, M. (2018). Genetic programming method for modelling of cup height in deep drawing process. *Advances in Production Engineering & Management*, vol. 13, no. 3, p. 358-365, DOI:10.14743/apem2018.3.296.
- [22] Senveter, J., Balic, J., Ficko, M., Klančnik, S. (2016). Prediction of technological parameters of sheet metal bending in two stages using feed forward neural network. *Tehnički vjesnik - Technical Gazette*, vol. 23, no. 4, p. 1155-1161, DOI:10.17559/TV-20141201225004.
- [23] Heingärtner, J., Fischer, P., Harsch, D., Renkci, Y., Hora, P. (2017). Q-Guard – an intelligent process control system. *Journal of Physics: Conference Series*, vol. 896, p. 012032, DOI:10.1088/1742-6596/896/1/012032.
- [24] Balasubramanian, M., Ganesh, P., Ramanathan, K., Kumar, V.S.S. (2017). An Experimental Investigation and Numerical Simulation in SPF of AA 5083 Alloy using Programming Logic Control Approach. *Strojniški vestnik - Journal of Mechanical Engineering*, vol. 63, no. 4, p. 255-264, DOI:10.5545/sv-jme.2016.3721.
- [25] Keran, Z., Kondić, Ž., Piljek, P., Runje, B. (2018). Accuracy of model force prediction in closed die coining process. *Strojniški vestnik - Journal of Mechanical Engineering*, vol. 64, no. 4, p. 225-232, DOI:10.5545/sv-jme.2017.5103.
- [26] EN 485-2.2016. *Aluminium and Aluminium Alloys - Sheet, Strip and Plate - Part 2. Mechanical Properties*. European Standards, Brussels.
- [27] ISO 6892-1.2016. *Metallic Materials - Tensile Testing - Part 1. Method of Test at Room Temperature*. International Organization for Standardization, Geneva.
- [28] EN ISO 10275.2014. *Metallic Materials - Sheet and strip - Determination of Tensile Strain Hardening Exponent*. European Standards, Brussels.
- [29] Atzema, E.H. (2016). *Formability of Auto Components*. Elsevier, Amsterdam.
- [30] Syngellakis, S., Habbab, H., Mellor, B.G. (2017). Finite element simulation of spherical indentation experiments. *International Journal of Computational Methods and Experimental Measurements*, vol. 6, no. 4, p. 749-763, DOI:10.2495/CMEM-V6-N4-749-763.
- [31] Trzepieciński, T., Lemu, H.G. (2014). Frictional conditions of AA5251 aluminium alloy sheets using drawbead simulator tests and numerical methods. *Strojniški vestnik - Journal of Mechanical Engineering*, vol. 60, no. 1, p. 51-60, DOI:10.5545/sv-jme.2013.1310.
- [32] Duran, D., Karadogan, C. (2016). Determination of Coulomb's friction coefficient directly from cylinder compression tests. *Strojniški vestnik - Journal of Mechanical Engineering*, vol. 62, no. 4, p. 243-251, DOI:10.5545/sv-jme.2015.3141.
- [33] Yamashita, T. (1996). *Analysis of Anisotropic Material*. Russ College of Engineering and Technology, Ohio University, Athens.
- [34] Inal, K., Mishra, R.K., Cazacu, O. (2010). Forming simulation of aluminum sheets using an anisotropic yield function coupled with crystal plasticity theory. *International Journal of Solids and Structures*, vol. 47, no. 17, p. 2223-2233, DOI:10.1016/j.ijsolstr.2010.04.017.

# Suppression of Self-Excited Vibrations in Rotating Machinery Utilizing Leaf Springs

Chang Wang<sup>1</sup> – Jun Liu<sup>1,2,\*</sup> – Zhiwei Luo<sup>3</sup>

<sup>1</sup>Tianjin Key Laboratory for Advanced Mechatronic System Design and Intelligent Control,  
Tianjin University of Technology, China

<sup>2</sup>National Demonstration Centre for Experimental Mechanical and Electrical Engineering Education,  
Tianjin University of Technology, China

<sup>3</sup>Organization of Advanced Science and Technology, Kobe University, Japan

*When rotating machinery is operated above the major critical speed, self-excited vibrations appear due to internal friction of the shaft. Internal frictions are classified into hysteretic damping due to the friction in the shaft material and structural damping due to the dry friction between the shaft and the mounted elements. In this paper, a method to suppress the self-excited vibration using leaf springs are proposed. The structural damping is considered as the internal damping. The characteristics of a rotor with leaf springs are investigated systematically by using simulative and theoretical analyses. The validity of the proposed method is also proved by experiments.*

**Keywords:** self-excited vibration, internal damping, vibration suppression, leaf spring, experiment

## Highlights

- A rotor system with internal frictions and leaf springs is analysed by using numerical simulations and theoretical analyses systematically, and self-excited vibrations occur above the major critical speed.
- The self-excited vibrations can be suppressed by using leaf springs on the rotor system with internal frictions.
- The effectiveness of the proposed suppressing method is verified by experiments, simulations, and theoretical analyses.

## 0 INTRODUCTION

In rotor systems, the friction created between a rotational part and a stationary part, such as a rotating disk and the surrounding air, is called external friction, and another friction that works within two rotating parts is called internal friction. In addition, the internal friction is further classified into hysteretic damping, which works in the inside part of the shaft material, and structural damping, which occurs due to the sliding between the shaft and mounted elements such as bearings and gears. It is well known that the self-excited vibration occurs above the major critical speed when the internal friction works in the rotor system [1]. Regarding the self-excited vibration caused by internal friction, many scholars have conducted extensive research. Queiroz [2] studied flow-induced instabilities known as “whirl” and “whip” on the lightly-loaded shaft supported by fluid-film bearings and analysed self-excited vibrations. Bonello and Pham [3] presented a generic technique for the transient nonlinear dynamic analysis (TNDA) and the static equilibrium stability analysis (SESA) of a turbomachine running on foil air bearing (FABs). Their research revealed stabilities and self-excited vibrations of the rotor system. Boyaci et al. [4] carried out an investigation of the stability and bifurcation phenomena of the rotor-bearing system and found

self-excited vibrations with very high amplitudes. Bykov and Tovstik [5] studied synchronous whirling and asynchronous self-excited vibrations on the statically imbalance rotor under action conditions of external and internal damping forces. Because the nonlinear characteristics of the internal friction are very complicated, obtaining succinct expression of the theory is very difficult. The mechanism of self-excited vibrations caused by the internal friction was understood [1] to [5]. Ishida and Yamamoto [6] investigated characteristics of the subharmonic resonance of the order of 1/2 on the rotor-bearing system with a nonlinear spring-restoring force and an internal damping force. The phenomena were understood that self-excited vibrations occurred under the forced autonomous system. In addition, many researchers studied self-excited vibrations due to other causes on the rotor system. Coudeyras et al. [7] presented a novel nonlinear method called the Constrained Harmonic Balance Method (CMBM), which is applied to solve the specific problem of disc brake squeal with extensive parameters and to predict self-excited vibrations. Han et al. focused on the experimental study for the dynamic characteristics of a permanent magnet (PM) disk-type motor rotor supported by an aerostatic gas bearing and analysed low-frequency vibrations caused by self-excited gas films [8]. Vljajic et al. [9] studied dynamic

\*Corr. Author's Address: Tianjin University of Technology, No. 391 Bin Shui Xi Dao Road, Tianjin, China, liujunjp@tjut.edu.cn

characteristics of a modified Jeffcott rotor with the torsional deformation and the rotor-stator contact and investigated self-excited backward whirling motions with the continuous stator contact. Hua et al. [10] presented the basic excitation mechanism and vibration characteristics on the coupled bending and torsional nonlinear dynamic model of a rotor system with a nonlinear friction, and the results revealed multiform complex nonlinear dynamic responses of the rotor system under rubbing. Nishimura et al. [11] explained self-excited vibrations in the vertical pump with a journal bearing and demonstrated the nonlinear steady-state vibration analysis of self-excited vibrations. Tadokoro et al. [12] focused on self-excited vibrations induced by the velocity-weakening friction in rotary contact systems. Chouchane and Amamou [13] analysed the bifurcation of the steady-state equilibrium point of the journal centre and predicted stable or unstable limit cycles from the equilibrium point at the major critical speed. Peletan et al. [14] proposed a quasi-periodic harmonic balance method (HBM) to deal with self-excited vibrations of the steady-state dynamic behaviour of rotor-stator contact problems.

It is well known that harmonic resonances can be avoided by controlling rotational speeds. However, since the self-excited vibrations occur within a wide range of rotational speeds, it is difficult to escape the occurrence of self-excited vibrations. In addition, the amplitude of vibrations increases with exponential growth if there is no limit cycle. Based on the two characteristics mentioned above, it is concluded that self-excited vibrations are more dangerous than the harmonic resonance. Some methods of suppressing self-excited vibrations have been proposed. Kligerman et al. [15] investigated the nonlinear behaviour of shaft supports at the boundaries and stability of a rotating system with an electromagnetic noncontact damper, and a closed-form solution for the radius of the limit cycle and the frequency of self-excited vibrations are obtained. Inoue et al. [16] researched the occurrence region and vibration characteristics of self-excited vibrations caused by the ball balancer. The results are also validated experimentally. However, the theoretical analyses of self-excited vibrations have been less commonly proposed.

In this paper, based on self-excited vibrations by causing the structural damping, a suppressing method by using leaf springs is proposed. The vibration characteristics of a rotor with leaf springs are systematically investigated using theoretical analyses and numerical simulations. The validity of proposed method is also verified by experiments.

## 1 THEORETICAL MODEL

### 1.1 Dynamic Equations

The theoretical model of the rotor system with leaf springs is shown in Fig. 1. The two degrees of freedom (2DOF) inclination model with the gyroscopic moment is adopted, and a rigid disk is mounted at the centre of a massless elastic shaft. To suppress self-excited vibrations due to the internal damping, a bearing is fitted to the shaft, and four groups of leaf springs are placed to contact with the outer race of the bearing in four directions shown in Fig. 1. The rectangular coordinate system  $O-xyz$  is established, and the  $z$ -axis coincides with the bearing centreline. The point  $O$  is the geometrical centre of the disk. The line  $OA$  is the centreline of the disk, and the line  $OB$  is the tangent of the shaft at Point  $O$ .  $\tau$  is the angle between lines  $OA$  and  $OB$ , which represents the imbalance of the rotor system.  $\theta$  is the angle between lines  $Oz$  and  $OB$ , and it is the inclination angle of the shaft at the position of the disk.  $\theta_x$  and  $\theta_y$  are projections of  $\theta$  on planes  $xz$  and  $yz$ , respectively.

It is assumed that the internal damping caused by the sliding between the disk and the shaft works in this system. In addition, the sliding here means that the inclined elastic rotor whirls with an angular velocity different from the rotational speed  $\omega$ , and the disk cannot move torsionally on the shaft. The dimensionless dynamic equations of the 2DOF rotor system can be obtained by reference to the study [1]. Considering effects of the internal damping and leaf springs, the dimensionless equations of motion of the rotor system are shown as follows:

$$\begin{cases} \ddot{\theta}_x + i_p \omega \dot{\theta}_y + c \dot{\theta}_x + \theta_x + k_L \theta_x - D_{ix} - D_{Lx} = F \cos \omega t \\ \ddot{\theta}_y - i_p \omega \dot{\theta}_x + c \dot{\theta}_y + \theta_y + k_L \theta_y - D_{iy} - D_{Ly} = F \sin \omega t \end{cases}, \quad (1)$$

where  $F = (1 - i_p) \tau \omega^2$ ,  $c$  is the coefficient of the external damping, and  $i_p$  is the ratio of the principal axis of the polar moment of inertia of the disk and the diametrical moment of inertia of the disk.  $D_{ix}$  and  $D_{iy}$  represent the internal damping force in  $x$  and  $y$  directions, and  $D_{Lx}$  and  $D_{Ly}$  represent the damping force of leaf springs in  $x$  and  $y$  directions.  $k_L$  is the increase of spring stiffness of the rotor due to leaf springs. They will be illustrated later in this paper.

### 1.2 Internal Damping (Structural Damping)

The pre-tightening force needs to be large enough to mount the disk on the shaft. When the deflection

of the shaft is comparatively large, the fibres of the shaft elongate or contract with the changes of the shaft orbit, which causes the pre-tightening force to be insufficient. Thus, the static friction cannot prevent the sliding between the shaft and the disk, and the type of friction has been transformed into dry friction. The dry friction, as internal friction, will cause structural damping. In addition, a large deflection of the shaft means that there is hysteretic internal damping due to frictions in the shaft material. In order to discuss influences of the structural damping on self-excited vibrations, it is necessary to eliminate the effects of the hysteretic internal damping caused by the deflection motion, which is the reason that the 2DOF model with an inclination motion is adopted.

Here, the Coulomb friction is applied to approximate the dry friction between the shaft and the disk. The internal damping force is determined by the difference in the whirling angular velocity and rotational speed.

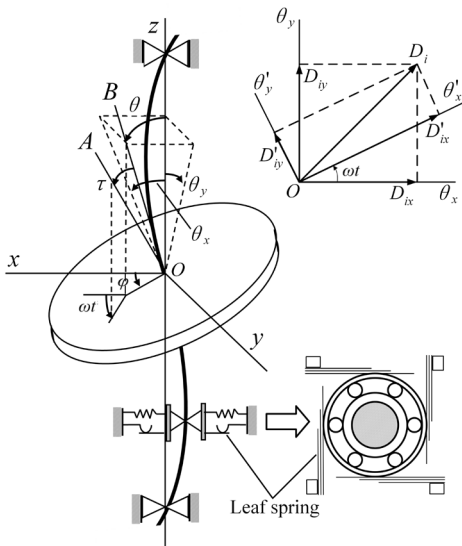


Fig. 1. Rotor model with leaf springs and coordinate system

Therefore, the internal damping force is discussed in the rotational coordinate system  $O-\theta'_x\theta'_y$  shown in Fig. 1. For simplicity of representation, complex variables  $z = \theta_x + i\theta_y$  in the coordinate system  $O-\theta_x\theta_y$  and  $z' = \theta'_x + i\theta'_y$  in the coordinate system  $O-\theta'_x\theta'_y$  are introduced. Based on the previous studies [1], the expression of the internal damping force in the rotational coordinate system  $O-\theta'_x\theta'_y$  is obtained as follows:

$$D'_i = D'_{ix} + iD'_{iy} = -h \frac{\dot{z}'}{|z'|} \quad (2)$$

The expression of the internal damping force is converted to the expression in the stationary coordinate system  $O-\theta_x\theta_y$  as follows:

$$\begin{cases} D_i = D'_i e^{i\omega t} = -h \frac{(\dot{\theta}_x + \omega\theta_y) + i(\dot{\theta}_y - \omega\theta_x)}{\sqrt{(\dot{\theta}_x + \omega\theta_y)^2 + (\dot{\theta}_y - \omega\theta_x)^2}} \\ D_{ix} = -h \frac{(\dot{\theta}_x + \omega\theta_y)}{\sqrt{(\dot{\theta}_x + \omega\theta_y)^2 + (\dot{\theta}_y - \omega\theta_x)^2}} \\ D_{iy} = -h \frac{(\dot{\theta}_y - \omega\theta_x)}{\sqrt{(\dot{\theta}_x + \omega\theta_y)^2 + (\dot{\theta}_y - \omega\theta_x)^2}} \end{cases}, \quad (3)$$

where  $h$  is a constant coefficient.

### 1.3 Damping Force and Elastic Force of the Leaf Spring

The damping force and elastic force of leaf springs work on the elastic shaft by the contact between the bearing and leaf springs shown in Fig. 1.

Under the condition with effects of the elastic force of leaf springs, the spring stiffness of the rotor system becomes larger. It is considered that the change of the spring stiffness is linear, and the increase of the restoring force of the rotor system are as follows:

$$\begin{cases} F_{Lx} = -k_L \theta_x \\ F_{Ly} = -k_L \theta_y \end{cases} \quad (4)$$

The leaf springs periodically deform with the motion of the rotor system. The dry friction of leaf springs is not negligible in the system. The restoring force has a hysteresis characteristic due to the dry friction, as shown in Fig. 2. The damping forces of leaf springs can be approximately described as follows:

$$D_{Lx} = -h_L \frac{\dot{\theta}_x}{|\dot{\theta}_x|}, D_{Ly} = -h_L \frac{\dot{\theta}_y}{|\dot{\theta}_y|} \quad (5)$$

where  $h_L$  is a function of the magnitude of a relative velocity  $|\dot{\theta}_x|$  or  $|\dot{\theta}_y|$ .

This damping force increases with the increase of the preload between leaves, and the viscous damping force increases in proportion to the velocity of the movement. Here, the dry friction is also approximated by the Coulomb friction. With the above approximation,  $h_L$  is considered as a constant coefficient, and coulomb damping force is independent of the velocity.

### 1.4 Natural Frequency Equation and Major Critical Speed

With regard to leaf springs, the natural frequency equation of the rotor system is obtained as follows:

$$(1 + h_L) + i_p \omega p - p^2 = 0. \tag{6}$$

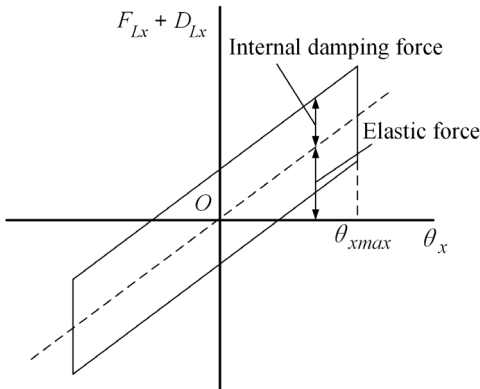


Fig. 2. Hysteretic characteristic of leaf springs

The relationship between natural frequencies and the rotational speed is obtained by solving Eq. (6), and the results are shown in Fig. 3. There are two natural frequencies  $p_f < 0$  and  $p_b > 0$  shown in Fig. 3. The  $p_f$  is a natural frequency of a forward whirling mode and  $p_b$  is that of a backward whirling mode. In addition, the major critical speed can be expressed as follows:

$$\omega_c = \sqrt{\frac{(1 + h_L)}{(1 - i_p)}}. \tag{7}$$

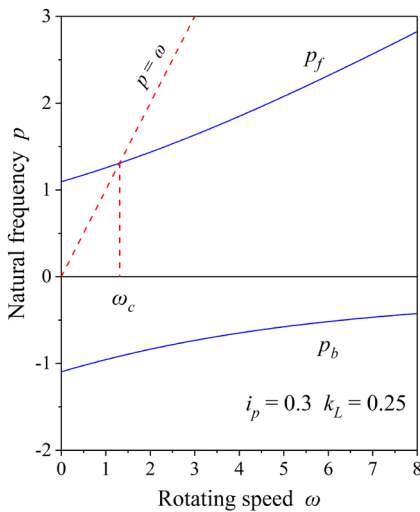


Fig. 3. Natural frequency of the 2 DOF system

2 THEORETICAL ANALYSIS WITHOUT IMBALANCE

In this chapter, the theoretical analysis is executed under the case without an imbalance ( $\tau = 0$ ). Because self-excited vibrations occur above the major critical speed, the following analyses will set the case of

$\omega > \omega_c$ . In addition, because the self-excited vibration does not appear under the case of  $\omega < \omega_c$ , the solutions with zero-amplitude are stable.

2.1 Theoretical Analysis

When the imbalance is not considered, and the rotational speed considers the case of  $\omega > \omega_c$ , solutions for self-excited vibrations are as follows:

$$\begin{cases} \theta_x = R \cos(p_f t + \delta) \\ \theta_y = R \sin(p_f t + \delta) \end{cases} \tag{8}$$

Substitute solutions Eq. (8) into the equations of motion, and represent the order of magnitude by the notation  $O(\epsilon)$  in this following. Based on the assumption that the amplitude R and the phase angle  $\delta$  change slowly, the  $\cos(p_f t + \delta)$  and  $\sin(p_f t + \delta)$  will be compared with the accuracy of  $O(\epsilon^2)$  to obtain their coefficients.

The internal damping force can be expanded as follows:

$$D_{ix} = -h \left[ \begin{aligned} & \frac{\dot{R} \cos(p_f t + \delta)}{R(\omega - p_f) - R\dot{\delta} + O(\epsilon^2)} \\ & - \frac{R(p_f + \dot{\delta}) \sin(p_f t + \delta)}{R(\omega - p_f) - R\dot{\delta} + O(\epsilon^2)} \\ & + \frac{\omega R \sin(p_f t + \delta) + O(\epsilon^2)}{R(\omega - p_f) - R\dot{\delta} + O(\epsilon^2)} \end{aligned} \right] = -h \left\{ \sin(p_f t + \delta) + \frac{\dot{R} \cos(p_f t + \delta)}{R(\omega - p_f)} \right\} + O(\epsilon^3). \tag{9}$$

The damping force of the leaf spring can be expanded as follows:

$$\begin{aligned} D_{Lx} &= -h_L \frac{\dot{\theta}_x}{|\dot{\theta}_x|} \\ &= -h_L \frac{\cos \alpha \cos(p_f t + \delta) - \sin \alpha \sin(p_f t + \delta)}{|\cos \alpha \cos(p_f t + \delta) - \sin \alpha \sin(p_f t + \delta)|} \\ &= -h_L \frac{\cos(p_f t + \delta + \alpha)}{|\cos(p_f t + \delta + \alpha)|} \\ &= -\frac{4h_L}{\pi} \cos(p_f t + \delta + \alpha) + \dots \\ &= -\frac{4h_L}{\pi} \left\{ \begin{aligned} & \frac{\dot{R} \cos(p_f t + \delta)}{\sqrt{\dot{R}^2 + R^2(p_f + \dot{\delta})^2}} \\ & - \frac{R(p_f + \dot{\delta}) \sin(p_f t + \delta)}{\sqrt{\dot{R}^2 + R^2(p_f + \dot{\delta})^2}} \end{aligned} \right\} + \dots, \tag{10} \end{aligned}$$

where  $\alpha = \arctan \frac{R(p + \dot{\delta})}{\dot{R}}$ .

As a result, the equations of theoretical solutions can be obtained following:

$$\begin{cases} -R2p\dot{\delta} + i_p\omega R\dot{\delta} + c\dot{R} \\ +h\frac{\dot{R}}{R(\omega - p)} + \frac{4h_L}{\pi} \frac{\dot{R}}{\sqrt{\dot{R}^2 + R^2(p + \dot{\delta})^2}} = 0 \\ -2\dot{R}p + i_p\omega\dot{R} - cR(p + \dot{\delta}) \\ +h - \frac{4h_L}{\pi} \frac{R(p + \dot{\delta})}{\sqrt{\dot{R}^2 + R^2(p + \dot{\delta})^2}} = 0 \end{cases} \quad (11)$$

### 2.2 Steady-state Solution

If the convergence of self-excited vibrations approaches a limit cycle, the steady-state solutions can be obtained as follows:

$$R = R_0, \delta = \delta_0. \quad (12)$$

The steady-state solutions can be obtained from equations given by setting derivatives of the left-hand sides of Eq. (11), which equals zero. The solution is shown as follows:

$$R_0 = \left( h - \frac{4h_L}{\pi} \right) \frac{1}{cp_f}. \quad (13)$$

### 2.3 Stability Analysis of the Solution

To investigate the stability of solutions, we consider small variations  $\zeta(t)$  and  $\eta(t)$  of  $O(\epsilon)$  as follows:

$$\begin{cases} R = R_0 + \zeta \\ \delta = \delta_0 + \eta \end{cases} \quad (14)$$

Substituting Eq. (14) into Eq. (11), the small terms  $O(\epsilon^3)$  will be neglected, and the equations of solutions are obtained following:

$$\begin{cases} -2p_f R_0 \dot{\eta} + i_p \omega R_0 \dot{\eta} \\ + \frac{h}{(\omega - p_f) R_0} \dot{\zeta} + \frac{4h_L}{\pi} \frac{\dot{\zeta}}{R_0 p_f} = 0 \\ -2\dot{\zeta} p_f + i_p \omega \dot{\zeta} - c \dot{\zeta} p_f = 0 \end{cases} \quad (15)$$

Assuming variations  $\zeta(t)$  and  $\eta(t)$  to be  $\zeta(t) = Ae^{st}$  and  $\eta(t) = Be^{st}$ , and substituting them into Eq. (15), Eq. (16) can be obtained as follows:

$$s = -\frac{cp_f}{(2p_f - i_p\omega)} < 0. \quad (16)$$

Obviously, the solutions are always stable because  $\zeta(t)$  and  $\eta(t)$  are convergent.

The resonance response curves are obtained by numerical simulations and the theoretical analysis, and the results are shown in Fig. 4. The solid lines represent stable solutions. Fig. 4 shows three cases of the damping force of leaf springs, such as  $h_L=0$  with  $k_L=0$ ,  $h_L=0.005$  with  $k_L=0.25$  and  $h_L=0.01$  with  $k_L=0.25$ . The dotted line I represents the case without leaf springs, and the dotted line II represents the case with leaf springs. The figure shows that each case of the system always has a stable solution in the wide rotational speed range and the amplitude gradually becomes smaller when the rotational speed increases. Under the conditions with leaf springs, the amplitude of self-excited vibrations significantly reduced with the increase of the parameter  $h_L$ . It is concluded that the leaf springs can effectively suppress self-excited vibrations.

Based on Eq. (13), self-excited vibrations do not occur under the case of  $h_L > \pi h/4$ . The results of the above analyses show that leaf springs can effectively suppress self-excited vibrations in the wide rotational speed range.

## 3 THEORETICAL ANALYSIS WITH IMBALANCE

Due to the existence of internal damping terms, the multi-scale perturbation method and the harmonic balance method, it is difficult to theoretically analyse the vibration characteristics of the rotor system. In this paper, the improved shooting method is used to solve approximate solutions of the harmonic component.

### 3.1 Theoretical Analysis

Firstly, we reduce the order of Eq. (1). Putting  $\Delta_{\theta_x} = \dot{\theta}_x$ ,  $\Delta_{\theta_y} = \dot{\theta}_y$ , Eq. (17) with four variables can be obtained as follows:

$$\begin{bmatrix} \dot{\theta}_x \\ \Delta_{\theta_x} \\ \dot{\theta}_y \\ \Delta_{\theta_y} \end{bmatrix} = \begin{bmatrix} f_1(\theta_x, \Delta_{\theta_x}, \theta_y, \Delta_{\theta_y}) \\ f_2(\theta_x, \Delta_{\theta_x}, \theta_y, \Delta_{\theta_y}) \\ f_3(\theta_x, \Delta_{\theta_x}, \theta_y, \Delta_{\theta_y}) \\ f_4(\theta_x, \Delta_{\theta_x}, \theta_y, \Delta_{\theta_y}) \end{bmatrix}$$

$$= \begin{bmatrix} \Delta_{\theta_x} \\ F \cos \omega t - i_p \omega \Delta_{\theta_y} - c \Delta_{\theta_x} - (1 + k_L)\theta_x + D_{ix} + D_{Lx} \\ \Delta_{\theta_y} \\ F \sin \omega t + i_p \omega \Delta_{\theta_x} - c \Delta_{\theta_y} - (1 + k_L)\theta_y + D_{iy} + D_{Ly} \end{bmatrix}, \quad (17)$$

where  $D_{ix} = -h \frac{\Delta_{\theta_x} + \omega\theta_y}{\sqrt{(\Delta_{\theta_x} + \omega\theta_y)^2 + (\Delta_{\theta_y} - \omega\theta_x)^2}}$ ,  
 $D_{iy} = -h \frac{\Delta_{\theta_y} - \omega\theta_x}{\sqrt{(\Delta_{\theta_x} + \omega\theta_y)^2 + (\Delta_{\theta_y} - \omega\theta_x)^2}}$ ,  
 $D_{Lx} = -h_L \frac{\Delta_{\theta_x}}{|\Delta_{\theta_x}|}$  and  $D_{Ly} = -h_L \frac{\Delta_{\theta_y}}{|\Delta_{\theta_y}|}$ .

The components of the harmonic vibration are the main interest in the theoretical analyses, and it is considered that vibration components of constant terms are small. Therefore, we can assume the solutions to be as follows:

$$\begin{cases} \theta_x = P_{\theta_x} \cos(\omega t + \varphi_1) \Delta_{\theta_x} = P_{\Delta_{\theta_x}} \sin(\omega t + \varphi_1) \\ \theta_y = P_{\theta_y} \sin(\omega t + \varphi_1) \Delta_{\theta_y} = P_{\Delta_{\theta_y}} \cos(\omega t + \varphi_1) \end{cases} \quad (18)$$

Substituting the solution Eq. (18) into Eq. (17), we make  $\omega t = 2n\pi$  ( $n$  represents the number of cycles in the system response) to eliminate time parameters in the system. Nonlinear equations of five variables can be obtained as follows:

$$\begin{bmatrix} -P_{\theta_x} \omega \sin(\varphi_1) \\ P_{\Delta_{\theta_x}} \omega \cos(\varphi_1) \\ P_{\theta_y} \omega \cos(\varphi_1) \\ -P_{\Delta_{\theta_y}} \omega \sin(\varphi_1) \end{bmatrix} = \begin{bmatrix} P_{\Delta_{\theta_x}} \sin(\varphi_1) \\ F - i_p \omega P_{\Delta_{\theta_y}} \cos(\omega t + \varphi_1) - c P_{\Delta_{\theta_x}} \sin(\omega t + \varphi_1) \\ -(1 + k_L) P_{\theta_x} \cos(\omega t + \varphi_1) + D'_{ix} + D'_{Lx} \\ P_y \cos(\varphi_1) \\ i_p \omega P_{\Delta_{\theta_x}} \sin(\omega t + \varphi_1) - c P_{\Delta_{\theta_y}} \cos(\omega t + \varphi_1) \\ -(1 + k_L) P_{\theta_y} \sin(\omega t + \varphi_1) + D'_{iy} + D'_{Ly} \end{bmatrix} \quad (19)$$

Therefore, the optimal numerical solution of each parameter in Eq. (19) can be solved by using the genetic algorithm.

### 3.2 Stability Analysis of the Solution

This paper applies the first Lyapunov method for the stability of approximate solutions. According to Eq. (17), the Jacobian matrix **A** can be obtained as follows:

$$\mathbf{A} = \begin{bmatrix} \frac{\partial f_1}{\partial \theta_x} & \frac{\partial f_1}{\partial \Delta_{\theta_x}} & \frac{\partial f_1}{\partial \theta_y} & \frac{\partial f_1}{\partial \Delta_{\theta_y}} \\ \frac{\partial f_2}{\partial \theta_x} & \frac{\partial f_2}{\partial \Delta_{\theta_x}} & \frac{\partial f_2}{\partial \theta_y} & \frac{\partial f_2}{\partial \Delta_{\theta_y}} \\ \frac{\partial f_3}{\partial \theta_x} & \frac{\partial f_3}{\partial \Delta_{\theta_x}} & \frac{\partial f_3}{\partial \theta_y} & \frac{\partial f_3}{\partial \Delta_{\theta_y}} \\ \frac{\partial f_4}{\partial \theta_x} & \frac{\partial f_4}{\partial \Delta_{\theta_x}} & \frac{\partial f_4}{\partial \theta_y} & \frac{\partial f_4}{\partial \Delta_{\theta_y}} \end{bmatrix} \quad (20)$$

Substituting theoretical solutions into matrix **A** to obtain the coefficient matrix, the characteristic equation of the rotor system can be obtained as follows:

$$\begin{bmatrix} a_{11} - \lambda & a_{12} & a_{13} & a_{14} \\ a_{21} & a_{22} - \lambda & a_{23} & a_{24} \\ a_{31} & a_{32} & a_{33} - \lambda & a_{34} \\ a_{41} & a_{42} & a_{43} & a_{44} - \lambda \end{bmatrix} = 0. \quad (21)$$

The stability of theoretical solutions can be investigated by judging the positive and negative of the real part of the eigenvalue  $\lambda_i$ . If all the real parts of eigenvalues are negative, the solution is stable. If there is at least one positive real part and others are negative, the solution is unsteady.

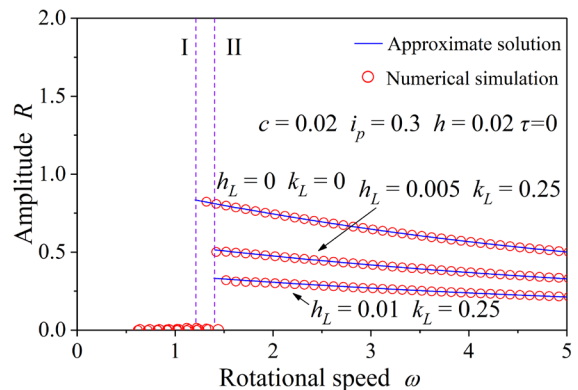


Fig. 4. Resonance responses without an imbalance

Through the above process, theoretical solutions are obtained and shown in Fig. 5. In the figure, the solid lines represent the stable solutions. The results show that the resonance curve of the harmonic vibration is a typical resonance curve of the 2DOF rotor, and the harmonic vibration and self-excited vibration are mutually independent.

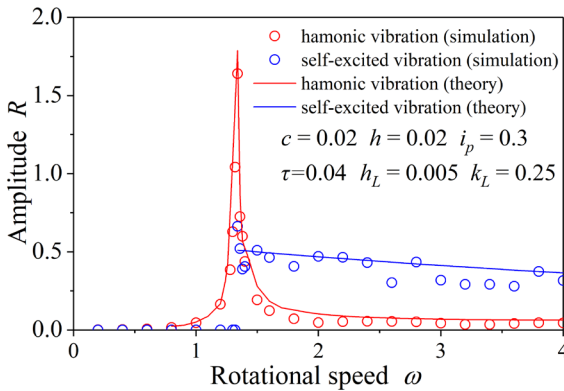


Fig. 5. Resonance responses with an imbalance

#### 4 NUMERICAL SIMULATION

##### 4.1 Simulation without Imbalance

Based on Eq. (1) with  $\tau=0$ , results of the numerical simulation without considering an Imbalance are shown in Fig. 4. The self-excited vibration occurs on the line I under the case without a leaf spring in the rotor system, and the vibration response appears on the line II under the case with leaf springs. The results of simulations consist well with results of the theoretical analysis in Chapter 3. When  $h_L=0.005$  and  $\omega=2$ , the frequency components of the response are shown in Fig. 6. This frequency corresponds to the frequency  $p_f$  shown in Fig. 3, indicating that self-excited vibrations occur in the rotor system.

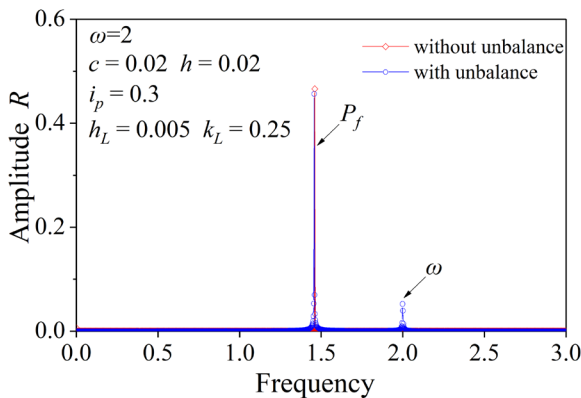


Fig. 6. Spectrum of the response

##### 4.2 Simulation with Imbalance

Based on Eq. (1) with  $\tau \neq 0$ , numerical simulations considering an Imbalance are shown in Fig. 7. The almost-periodic motions occur above the major critical

speed, and the range of the amplitude becomes smaller with the increase of the rotational speed. Fig. 6 shows frequency components of the system response, and it is found that the frequency of self-excited vibrations remain unchanged under the case with the imbalance or without the imbalance. In addition, Fig. 8 shows that beat vibrations occur in the vicinity of the major critical speed because the frequency of self-excited vibrations is close to the frequency of the harmonic vibration.

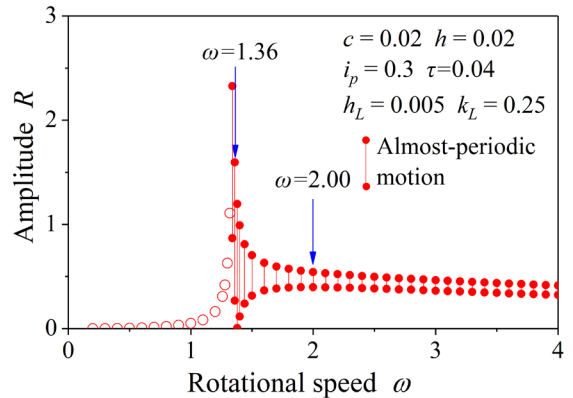


Fig. 7. Simulation with an imbalance

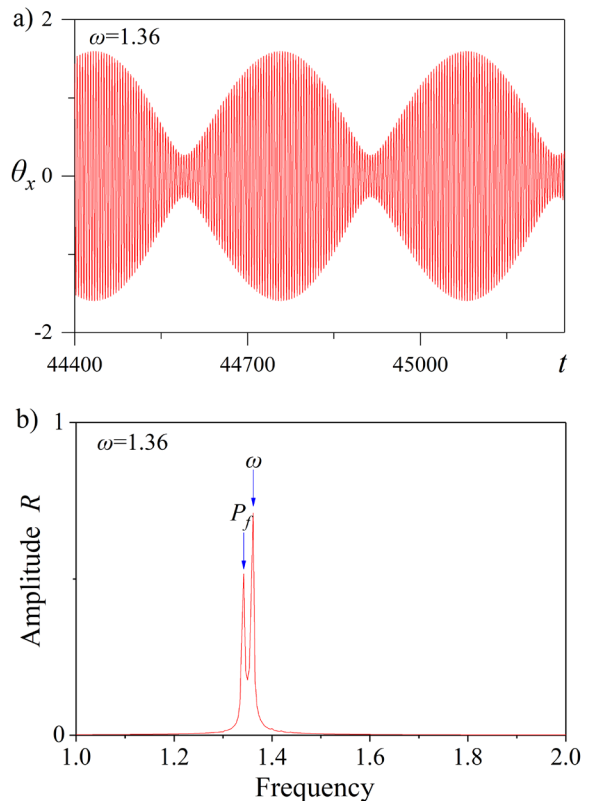


Fig. 8. Vibration response (with an imbalance); a) time history; and b) spectrum of response

Response curves of the harmonic vibration and self-excited vibrations obtained by simulations and theoretical analyses are shown in Fig. 5. Results show that self-excited vibrations appear above the major critical speed and the amplitude gradually decreases with the rotational speed increasing. Approximate solution curves of the harmonic vibration and self-excited vibrations obtained in Chapter 3 are stable and consistent with the results of numerical simulations.

According to the above analyses, the harmonic vibration and self-excited vibrations are basically independent, and the almost-periodic motions occur due to the superposition of the harmonic vibration and self-excited vibrations.

## 5 EXPERIMENTS

### 5.1 Experimental Device

The structure of the experimental setup is shown in Fig. 9. The downside of the rotor system is free, which is called a cantilevered rotor system. The length of the shaft is 760 mm, and the diameter is 12 mm. The diameter of the disk is 260 mm, and the thickness is 10mm. There is a collar to adjust the pre-tightening force on the rotor, and the internal damping force can be obtained by changing the fastening force of the collar. The ball bearing (#6205) is installed on the downward direction from the disk by about 60 mm. Four groups of leaf springs are provided in contact with the outer race of the bearing from four directions. Each group of leaf springs is composed of three leaves with different lengths. The dry friction can be created between leaves. In addition, two laser sensors are applied to measure radial displacements of the disk on the two orthogonal directions, and the vibration amplitude  $R$  of the rotor system can be obtained.

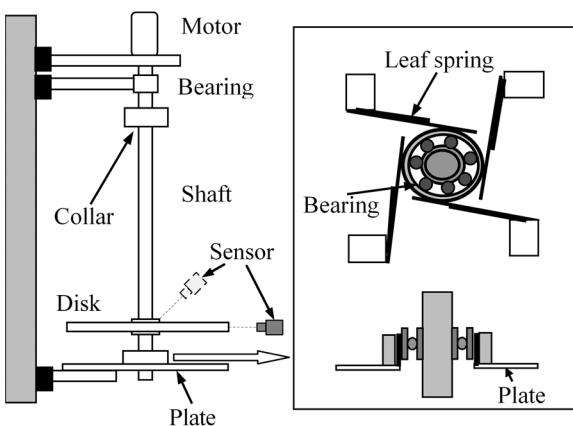


Fig. 9. Experimental setup

### 5.2 Experimental Results

The response curve of the experiment without the leaf springs is shown in Fig. 10a. The arrows indicate that the amplitude of self-excited vibrations gradually increases from the initial amplitude presented by symbol  $\times$ . It can be seen that self-excited vibrations occur when the rotational speed is higher than the major critical speed. Because it is very dangerous, the experiment was stopped when the amplitude is over approximately 2 mm. The limit cycle is not validated. In addition, the time history of Point A is shown in Fig. 10b, and the amplitude of the vibration gradually increases from the initial amplitude.

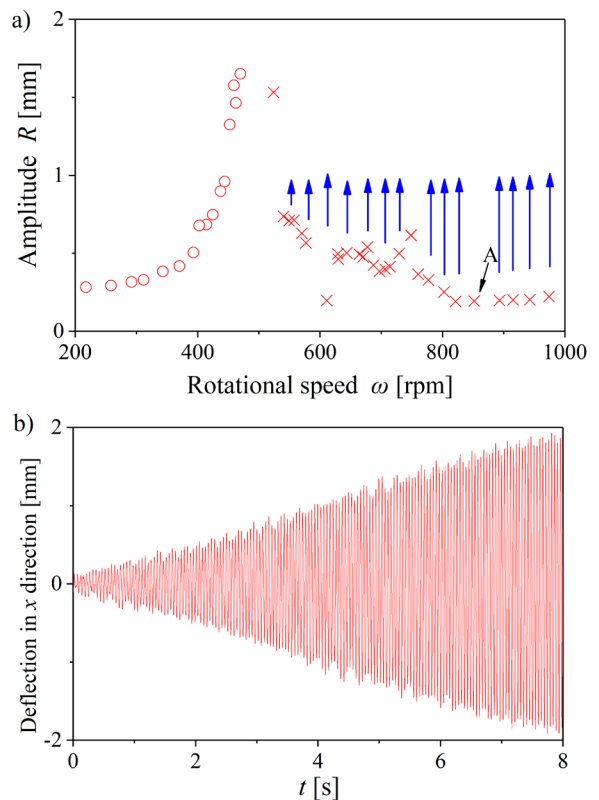


Fig. 10. Self-excited vibration (Without a leaf spring); a) resonance curve; b) time history

The response curve of the experiment with leaf springs is shown in Fig. 11. Due to the damping force of leaf springs, the resonance amplitude in the vicinity of the major critical speed becomes smaller and self-excited vibrations do not occur above the major critical speed. The measurement results are whole harmonic vibrations. For the comparison, the response curve of the experiment with leaf springs and a larger imbalance is shown in Fig. 12. Under the condition

of Fig. 12, the major critical speed can be determined clearly, and no self-excited vibrations occur above the major critical speed. When disturbances were repeatedly applied to the rotor system, self-excited vibrations did not occur above the major critical speed.

The above experimental results show that proposed leaf springs can effectively suppress self-excited vibrations.

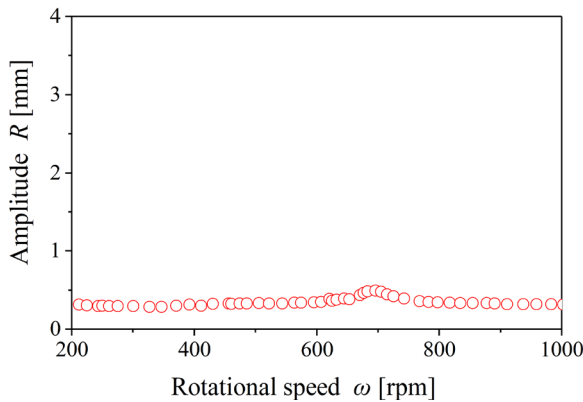


Fig. 11. Experimental result (With leaf springs)

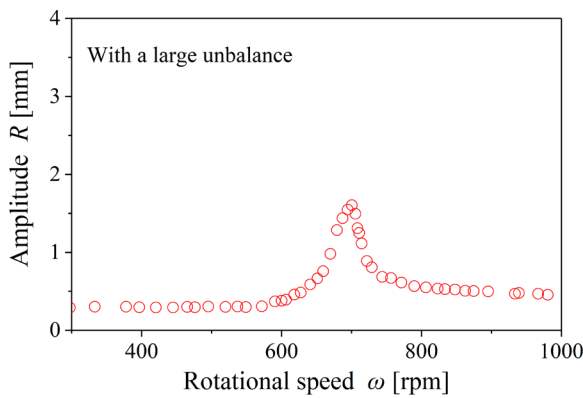


Fig. 12. Experimental result (Addition a large imbalance)

## 6 CONCLUSIONS

The self-excited vibrations caused by the structural damping occur above the major critical speed of rotating machinery. In this research, we propose a method to suppress self-excited vibrations by using leaf springs. The conclusions are as follows.

- (1) The self-excited vibrations occurring above the major critical speed can be suppressed by using leaf springs.
- (2) Under conditions with an imbalance, the rotor system becomes a forced autonomous system. The almost-periodic motions occur above the

major critical speed due to the superposition of the harmonic vibration and self-excited vibrations.

- (3) The theoretical analyses and numerical simulations can be confirmed well by experiments.

## 7 ACKNOWLEDGEMENTS

Thanks the National Key Research and Development Program of China (No.2017YFB1303304) and the Tianjin Natural Science Foundation of China (No.17JCZDJC38500) which give this paper's support.

## 8 NOMENCLATURES

$O-xyz$	rectangular coordinate system in fixed space
$\theta$	inclination angle of the shaft at the position of the disk
$\theta_x, \theta_y$	projections of $\theta$ onto the $xz$ - and $yz$ -planes
$\theta'_x, \theta'_y$	parameters in rotational coordinate system
$D'_{ix}, D'_{iy}$	parameters in rotational coordinate system
$i_p$	ratio of the principal axis of the polar moment of inertia of the disk and the diametrical moment of inertia of the disk
$c$	damping coefficient
$D_{ix}, D_{iy}$	internal damping forces
$D_{Lx}, D_{Ly}$	damping forces of the leaf spring
$K_L$	increase of the spring stiffness
$F$	amplitude of the excitation
$\varphi$	initial phase angle of the excitation
$t$	time
$\omega$	rotational speed, [rpm]
$\omega_c$	major critical speed, [rpm]
$\tau$	inclined angle of the rotor (imbalance)
$h, h_L$	constant coefficients of the internal damping force
$p, p_f, p_b$	natural frequencies of the rotor system
$R$	amplitude of vibrations of the rotor system, [mm]
$P_{\theta x}, P_{\theta y}$	amplitude of vibrations in $x$ and $y$ directions
$P_x, P_y$	first derivative term of amplitude of vibrations in $x$ and $y$ directions
$\delta, \varphi_1$	phase angle of vibrations of the rotor system
$O(\varepsilon)$	orders in magnitude of parameters
$\zeta, \eta$	small variations of $O(\varepsilon)$
$s$	variation in the complex field
$\lambda$	eigenvalue of the characteristic equation of the rotor system

## 9 REFERENCES

- [1] Yamamoto, T., Ishida, Y. (2012). *Linear and Nonlinear Rotordynamics: A Modern Treatment with Applications*. Wiley, New York.
- [2] De Queiroz, M. (2013). An active hydrodynamic bearing for controlling self-excited vibrations: theory and simulation. *Journal of Vibration and Control*, vol. 19, no. 14, p. 2211-2222, DOI:10.1177/1077546312458945.
- [3] Bonello, P., Pham, H.M. (2014). The efficient computation of the nonlinear dynamic response of a foil-air bearing rotor system. *Journal of Sound and Vibration*, vol. 333, no. 15, p. 3459-3478, DOI:10.1016/j.jsv.2014.03.001.
- [4] Boyaci, A., Lu, D.X., Schweizer, B. (2015). Stability and bifurcation phenomena of Laval/Jeffcott rotors in semi-floating ring bearings. *Nonlinear Dynamics*, vol. 79, no. 2, p. 1535-1561, DOI:10.1007/s11071-014-1759-5.
- [5] Bykov, V.G., Tovstik, P.E. (2018). Synchronous whirling and self-oscillations of a statically unbalanced rotor in limited excitation. *Mechanics of Solids*, vol. 53, p. 60-70, DOI:10.3103/S0025654418050047.
- [6] Ishida, Y., Yamamoto, T. (1993). Forced oscillations of a rotating shaft with nonlinear spring characteristics and internal damping (1/2 order subharmonic oscillation and entrainment). *Nonlinear Dynamics*, vol. 4, no. 5, p. 413-431, DOI:10.1007/BF00053689.
- [7] Coudeyras, N., Sinou, J.J., Nacivet, S. (2009). A new treatment for predicting the self-excited vibrations of nonlinear systems with frictional interfaces: The constrained harmonic balance method, with application to disc brake squeal. *Journal of Sound and Vibration*, vol. 319, no. 3-5, p. 1175-1199, DOI:10.1016/j.jsv.2008.06.050.
- [8] Han, D.J., Tang, C.L., Hao, L., Yang, J.F. (2016). Experimental studies on the effects of bearing supply gas pressure on the response of a permanent magnet disk-type motor rotor. *Journal of Mechanical Science and Technology*, vol. 30, no. 11, p. 4887-4892, DOI:10.1007/s12206-016-1008-6.
- [9] Vljajic, N., Champneys, A.R., Balachandran, B. (2017). Nonlinear dynamics of a Jeffcott rotor with torsional deformations and rotor-stator contact. *International Journal of Non-linear Mechanics*, vol. 92, p. 102-110, DOI:10.1016/j.ijnonlinmec.2017.02.002.
- [10] Hua, C.L., Cao, G.H., Rao, Z.S., Ta, N., Zhu, Z.C. (2017). Coupled bending and torsional vibration of a rotor system with nonlinear friction. *Journal of Mechanical Science and Technology*, vol. 31, no. 6, p. 2679-2689, DOI:10.1007/s12206-017-0511-8.
- [11] Nishimura, A., Inoue, T., Watanabe, Y. (2018). Nonlinear analysis and characteristic variation of self-excited vibration in the vertical rotor system due to the flexible support of the journal bearing. *Journal of Vibration and Acoustics*, vol. 140, no. 1, DOI:10.1115/1.4037520.
- [12] Tadokoro, C., Nagamine, T., Nakano, K. (2018). Stabilizing effect arising from parallel misalignment in circular sliding contact. *Tribology International*, vol. 120, p. 16-22, DOI:10.1016/j.triboint.2017.12.003.
- [13] Chouchane, M., Amamou, A. (2011). Bifurcation of limit cycles in fluid film bearings. *International Journal of Non-linear Mechanics*, vol. 46, no. 9, p. 1258-1264, DOI:10.1016/j.ijnonlinmec.2011.06.005.
- [14] Peletan, L., Baguet, S., Torkhani, M., Jacquet-Richardet, G. (2014). Quasi-periodic harmonic balance method for rubbing self-induced vibrations in rotor-stator dynamics. *Nonlinear Dynamics*, vol. 78, no. 4, p. 2501-2515, DOI:10.1007/s11071-014-1606-8.
- [15] Kligerman, Y., Gottlieb, O., Darlow, M.S. (1998). Nonlinear vibration of a rotating system with an electromagnetic damper and a cubic restoring force. *Journal of Vibration and Control*, vol. 4, no. 2, p. 131-144, DOI:10.1177/107754639800400203.
- [16] Inoue, T., Ishida, Y., Niimi, H. (2012). Vibration analysis of a self-excited vibration in a rotor system caused by a ball balancer. *Journal of Vibration and Acoustics*, vol. 134, no. 2, DOI:10.1115/1.4005141.

## Vsebina

### Strojniški vestnik - Journal of Mechanical Engineering

letnik 65, (2019), številka 10

Ljubljana, oktober 2019

ISSN 0039-2480

Izhaja mesečno

#### Razširjeni povzetki (extended abstracts)

David Muženič, Jaka Dugar, Davorin Kramar, Matija Jezeršek, Franci Pušavec: Izboljšanje obdelovalnosti keramike na osnovi cinkovega oksida s frezanjem z lasersko asistenco	SI 67
Daniel Miler, Stanko Škec, Branko Katana, Dragan Žeželj: Eksperimentalna študija kompozitnih drsnih ležajev: vpliv zračnosti na količnik trenja in temperaturo	SI 68
Thangavel Yuvaraj, Paramasivam Suresh: Analiza parametrov procesa elektroerozijske obdelave Inconela 718 po metodah Grey-Taguchi in Topsis	SI 69
Fariha Mukhtar, Faisal Qayyum, Hassan Elahi, Masood Shah: Numerična simulacija vpliva toplotnega utrujanja na napredovanje razpok v tanki gredni prirobnici iz jekla SS316L	SI 70
Mohammad Hadi Izadi, Shahrokh Hosseini Hashemi, Moharam Habibnejad Korayem: Uklon spojenih kompozitnih koničnih lupin pod aksialnimi tlačnimi obremenitvami po teoriji strižnih deformacij	SI 71
Roman Satošek, Michal Valeš, Tomaž Pepelnjak: Študija vplivnih parametrov vtiskovanja krogle za opredelitev nadzorne funkcije lastnosti materiala pri preoblikovalnih operacijah	SI 72
Chang Wang, Jun Liu, Zhiwei Luo: Omejevanje samovzbujenih vibracij pri rotacijskih strojih z listnatimi vzmetmi	SI 73



# Izboljšanje obdelovalnosti keramike na osnovi cinkovega oksida s frezanjem z lasersko asistenco

David Muženič\* – Jaka Dugar – Davorin Kramar – Matija Jezeršek – Franci Pušavec  
Univerza v Ljubljani, Fakulteta za strojništvo, Slovenija

Keramika na osnovi cinkovega oksida (ZnO) je elektronska keramika, ki se večinoma uporablja pri komponentah za zaščito pred impulzi zelo visoke napetosti (nekaj 100 kV). Za doseg pravilnega delovanja takšnih komponent je ena ključnih zahtev oster rob, ki nastane po končni obdelavi sintranega surovca. Zaradi same sestave te keramike, je le-ta izredno krhka, kar posledično privede do krušenja robov izdelka med končno obdelavo.

Trenutno stanje tehnike pri končni obdelavi izdelkov iz ZnO keramike je postopek lepanja. Hitrosti odnašanja materiala so pri postopku lepanja veliko manjše, kot pri postopkih odrezavanja (struženje, frezanje), kar privede do visokih proizvodnih stroškov takih komponent. Uspešna uvedba npr. frezanja v proizvodni proces komponent iz ZnO keramike bi tako privedla do občutnega znižanja proizvodnih stroškov takih komponent.

Kot je bilo ugotovljeno v predhodnih študijah avtorjev tega prispevka na frezanju ZnO keramike, je krušenje robov glavni faktor, ki znižuje obdelovalnost tega materiala in konvencionalen proces frezanja ni primeren za končno obdelavo izdelkov iz ZnO keramike. Z namenom izboljšanja obdelovalnosti tega materiala je bila v konvencionalni proces frezanja uvedena laserska asistenco (angl. Laser-Assisted Milling - LAMill), pri čemer se z uporabo laserja material obdelovanca pred rezalno cono segreje in s tem zmehča. Za določitev vpliva laserske asistencije na proces frezanja, je bila izvedena serija eksperimentov konvencionalnega frezanja ter frezanja z lasersko asistenco, pri katerih so bile uporabljene različne moči laserskega žarka. Rezultati so pokazali, da laserska asistenco lahko izboljša obdelovalnost ZnO keramike preko zmanjšanja krušenja robov ter izboljšanja hrapavosti obdelane površine. Za uporabljene parametre frezanja (globina in širina frezanja  $a_p = 0,1$  mm in  $a_e = 0,33$  mm ter podajalna in rezalna hitrost  $v_f = 250$  mm/min in  $v_c = 78,5$  m/min) je bilo ugotovljeno, da obstaja optimalna moč laserskega žarka, pri kateri je izboljšanje obdelovalnosti največje. Pri optimalni moči laserskega žarka 120 W je bilo zmanjšanje parametrov hrapavosti obdelane površine  $R_a$  in  $R_z$  37 % ter 46 %. Pri tej moči je bilo doseženo tudi 15 % zmanjšanje povprečne ter 17 % zmanjšanje največje širine odkruškov na robu, nastalem med obdelavo. Pri večjih močeh laserskega žarka je bilo doseženo dodatno zmanjšanje odkruškov, vendar so se pri teh močeh laserskega žarka na obdelani površini pojavile razpoke, za katere avtorji sklepajo, da so posledica termičnega šoka.

Čeprav je inovativni pristop k obdelavi ZnO keramike s frezanjem z lasersko asistenco, predstavljen v tem članku, pokazal potencial za izboljšanje obdelovalnosti tega materiala, je potrebno še veliko raziskav, da bi povsem razumeli vpliv laserske asistencije na obdelovalnost tega materiala ter bi lahko tak postopek uvedli v proizvodni proces elektronskih komponent. Krušenje robov, nastalih pri končni obdelavi takih komponent je glavni faktor, ki znižuje obdelovalnost tega materiala in aplikacija laserske asistencije v postopek frezanja je omejena s termičnim šokom, ki ga hitro ogrevanje z laserskim žarkom povzroči v materialu obdelovanca. Naslednji korak, nujen za razumevanje tega procesa je torej formacija modela prenosa toplote, s katerim se lahko zanesljivo napove temperatura blizu robov obdelovanca, kot posledica segrevanja z laserjem. Poleg tega je za obvladovanje tega procesa potrebno raziskati mehanizme, ki povzročijo povečanje obdelovalnosti tega materiala pri povišanih temperaturah.

**Ključne besede:** keramika na bazi cinkovega oksida (ZnO), obdelovalnost, frezanje z lasersko asistenco, hrapavost obdelane površine, krušenje robov

# Eksperimentalna študija kompozitnih drsnih ležajev: vpliv zračnosti na količnik trenja in temperaturo

Daniel Miler<sup>1</sup> – Stanko Škec<sup>1,2\*</sup> – Branko Katana<sup>1</sup> – Dragan Žeželj<sup>1</sup>

<sup>1</sup> Univerza v Zagrebu, Fakulteta za strojništvo in ladjedelništvo, Hrvaška

<sup>2</sup> Danska tehniška univerza, Danska

Drсни ležaji so se uveljavili zaradi svoje kompaktnosti in cenovne dostopnosti. Ti ležaji ne potrebujejo dodatnih kotalnih elementov in imajo zato manjši zunanji premer, velika kontaktna površina pa izboljšuje njihovo nosilnost. Na torne in obrabne lastnosti drsnih ležajev vpliva več parametrov, med drugim obremenitev, drsna hitrost, temperatura in površinska hrapavost. Pri pregledu literature niso bile odkrite študije, ki bi opisovale vpliv zračnosti na trenje v drsnih ležajih. Zato je bila opravljena eksperimentalna študija s ciljem določitve vpliva zračnosti na količnik trenja, temperaturo, obrabo in površinsko hrapavost pri drsnih ležajih.

Eksperiment je bil zasnovan kot faktorski poskus z dvema ravnema obremenitev (65 N in 115 N), dvema vrstama mazanja (suhu, s PTFE) in štirimi vrednostmi zračnosti (0,15 mm, 0,25 mm, 0,5 mm in 0,9 mm). Vsaka serija eksperimentov je bila ponovljena dvakrat zaradi zagotavljanja zanesljivosti rezultatov. Skupaj je bilo opravljenih 48 serij, vsaka pa je trajala dve uri.

Ležaji so bili izdelani iz kompozita NORDEN Maritim 605. Vsi ležaji so bili enake širine in nazivnega premera, razlikovali pa so se v zračnosti. Količnik trenja je bil izračunan iz velikosti sil na preizkuševališču, izmerjenih z merilno celico. Žarek termometra je bil usmerjen na drsni ležaj v bližini točke stika. Obraba je bila določena s tehtanjem preizkušancev pred eksperimentom in po njem, na enak način pa je bila izmerjena tudi površinska hrapavost.

Rezultati so pokazali, da zračnost vpliva na trenje tako v ležajih brez mazanja kot v ležajih, podmazanih s trdnim mazivom (PTFE). Pri ležajih brez mazanja se je količnik trenja zmanjševal s povečevanjem zračnosti. Pri ležajih, mazanih s PTFE, je treba poiskati optimum, saj je bil ugotovljen lokalni minimum količnika trenja znotraj opazovanega intervala zračnosti. Pri obravnavi temperature ležajev, obremenjenih s silo 65 N, je bila ugotovljena linearna odvisnost med količnikom trenja in temperaturo ležaja. Splošno veljavni trendi za obrabo in spremembo površinske hrapavosti niso bili ugotovljeni.

Čeprav je študija pokazala, da zračnost vpliva na količnik trenja, temperaturo in obrabo ležajev brez mazanja in ležajev, mazanih s PTFE, so prvi rezultati pokazali, da bodo za določitev optimalnih vrednosti potrebne še dodatne raziskave. S povečanjem števila ravni zračnosti bi se tako bilo mogoče izogniti morebitnim sedlastim točkam pri ugotavljanju obrabe. Za izboljšanje kakovosti rezultatov bi bilo mogoče med spremenljivke poleg zračnosti dodati še nazivni premer ležajev.

Članek je prispevek k boljšemu razumevanju vpliva zračnosti na lastnosti drsnih ležajev. Množina zbranih podatkov bo lahko dobra osnova za nadaljnje študije in za pridobivanje novih zaključkov.

**Ključne besede: drsni ležaj, zračnost, kompozit, količnik trenja, mazanje, eksperimentalna študija**

# Analiza parametrov procesa elektroerozijske obdelave Inconela 718 po metodah Grey-Taguchi in Topsis

Thangavel Yuvaraj\* – Paramasivam Suresh

Tehniški kolidž Muthayammal (avtonomni), Oddelek za strojništvo, Indija

Elektroerozijska obdelava (EDM) je postopek posebnega pomena za obdelavo trdih materialov in superzlitin. Toplotno obstojne superzlitine (HRSA) in še posebej Inconel so razširjene v letalski in vesoljski industriji, v pomorstvu, kriogenih skladiščnih rezervoarjih in jedrskih reaktorjih. Pregled literature je pokazal, da na elektroerozijsko obdelavo lukenj v Inconelu 718 vplivajo različni vhodni parametri. Za doseganje optimalnih rezultatov za vsak posamezni parameter obdelave so potrebni različni parametri procesa, izbira optimalnih parametrov obdelave pa je zato težavna naloga. Sistem Grey, ki ga je predlagal Deng, omogoča večciljno optimizacijo po metodi GRA. V članku je predstavljena optimizacija parametrov procesa EDM  $I$ ,  $V$ ,  $t_{on}$  in  $t_{off}$  z ortogonalno zasnovo eksperimenta  $L_{18}$  in metodo GRA z več odzivi, kot so stopnja odzema materiala ( $MR$ ), stopnja obrabe orodja ( $TWR$ ), nadmera ( $OC$ ) in konična nadmera ( $TOC$ ). Čeprav sta metodi Grey-Taguchi in TOPSIS primerni za večciljno optimizacijo, do sedaj še nista bili uporabljeni na tem področju. Pomemben prispevek te raziskave je v uporabi metod za preučevanje vplivnih parametrov, ki dajejo najboljše rezultate z razpoložljivimi podatki. Določene so bile optimalne vrednosti parametrov EDM po metodah GRA in TOPSIS. Obraba orodja pri različnih napetostih je bila preiskana z vrstično elektronsko mikroskopijo (SEM).

Uporabljena je bila medeninasta elektroda  $\varnothing$  0,5 mm in olje za EDM kot dielektrik. Debelina obdelovanca je bila 3,1 mm. Parametri so bili izbrani na osnovi pregleda literature in vrednosti so bile določene na osnovi preliminarnih eksperimentov. Uporabljene so bile vrednosti toka 10 A, 12 A in 14 A ter vrednosti napetosti 30 V, 40 V in 50 V. Vrednosti ton so bile 100  $\mu$ s, 150  $\mu$ s in 200  $\mu$ s, vrednosti toff pa 20  $\mu$ s, 30  $\mu$ s in 40  $\mu$ s. Oblikovana je bila zasnova eksperimenta  $L_{18}$  OA.

Optimalna kombinacija vhodnih parametrov za boljši odziv po metodi Grey Taguchi je bila  $I = 10$  A,  $V = 30$  V,  $t_{on} = 200$   $\mu$ s in  $t_{off} = 20$   $\mu$ s. Analiza variance je pokazala, da imata pglavitno vlogo pri obdelavi Inconela 718 napetost in čas toff. Potrditveni preizkusi so pokazali znatno izboljšavo vrednosti GRA pri optimalni kombinaciji parametrov, z 0,6969 na 0,7122. Potrditveni preizkus je dokazal, da je metoda GRA primerna za optimizacijo parametrov procesov EDM v proizvodni industriji in s tem za izboljšanje konkurenčnosti. Najboljša kombinacija za izboljšanje zmogljivosti po metodi TOPSIS je bila 10 A, 30 V, 100  $\mu$ s in 20  $\mu$ s. Obraba orodja pri različnih napetostih je bila preiskana z vrstično elektronsko mikroskopijo. Mikroposnetki SEM potrjujejo odvisnost vzorcev obrabe od napetosti. V prihodnje bo tako mogoče opraviti podrobnejše analize in optimizacijo električnih parametrov.

Pomemben prispevek raziskave je v uporabi metod za preučevanje vplivnih parametrov, ki dajejo najboljše rezultate z razpoložljivimi podatki. Z metodama GRA in TOPSIS so bile tako določene optimalne vrednosti parametrov za EDM.

**Ključne besede:** Inconel, ANOVA, Grey-Taguchi, nadmera, konus, TOPSIS

# Numerična simulacija vpliva toplotnega utrujanja na napredovanje razpok v tanki gredni prirobnici iz jekla SS316L

Fariha Mukhtar<sup>1</sup> – Faisal Qayyum<sup>2</sup> – Hassan Elahi<sup>3,\*</sup> – Masood Shah<sup>1</sup>

<sup>1</sup> Tehniška univerza, Oddelek za strojništvo, Pakistan

<sup>2</sup> Tehniška univerza Bergakademie Freiberg, Inštitut za preoblikovanje kovin, Nemčija

<sup>3</sup> Univerza v Rimu Sapienza, Oddelek za strojništvo in letalsko tehniko, Italija

Tudi po več kot desetletju raziskovanja pojava razpok v komponentah jedrskih reaktorjev zaradi toplotnega utrujanja še vedno obstajajo vrzeli v znanju. Obstaja potreba po znanju o napredovanju razpok in vplivih razpok na utrujenostno trajnostno dobo jeklenih komponent zaradi intenzivnega toplotnega utrujanja. Raziskovalci so se v preteklosti ukvarjali z eksperimentalnimi preiskavami, ki zaradi omejitev pri zbiranju podatkov zagotavljajo le omejeno razumevanje. Raziskovalna tema je bil tudi razvoj analitičnih in numeričnih metod z različnimi aproksimacijami, ki ne dajejo zanesljivih rezultatov. Točni modeli za numerične simulacije lahko pripomorejo k boljšemu razumevanju vpliva različnih dejavnikov na napredovanje razpok.

V predstavljeni raziskavi je bil razvit model za numerično simulacijo na osnovi končnih elementov s pomočjo komercialne programske opreme ABAQUS. Cilj je bil pridobitev vpogleda v napredovanje in zaustavitev širitve razpok v tanki gredni prirobnici iz jekla SS316L. Sestav je bil hlajen od znotraj, vir cikličnih toplotnih obremenitev pa je bil postavljen na obod prirobnice. Opravljeni so bili eksperimenti na posebnem preizkuševališču s tuljavo za indukcijsko ogrevanje zunanega oboda. Za določitev natančnega temperaturnega profila so bili uporabljeni termoelementi, radialno pritrjeni na obod. Modelu so bili dodeljeni realnočasovni in temperaturno odvisni podatki o elastoplastičnih lastnostih materiala. Robni pogoji in toplotni profil za numerični model so bili usklajeni s podatki eksperimentov.

Pridobljeni rezultati simulacije so bili za validacijo primerjani z rezultati eksperimentov. V predstavljenem delu so ovrednotene napetosti, ki povzročijo začetek razpok, vpliv števila in dolžine razpok na napetosti, absorpcija energija na vrhu razpoke v vsakem toplotnem ciklu in pragovne vrednosti razpok. Ugotovljeno je bilo, da se vrednost CMOD povečuje neodvisno od števila ali dolžine razpok in zato ni primerna za identifikacijo poškodb zaradi toplotnega utrujanja. Razviti model za simulacijo pripomore k boljšemu razumevanju evolucije napetosti in deformacij zaradi cikličnih toplotnih obremenitev v disku iz jekla SS316L. Ugotovljeno je bilo, da je nastanek razpok posledica obodnih napetosti v prirobnici. Razviti model omogoča boljše razumevanje pojavov napredovanja razpok in sproščanja energije na vrhu razpok ter bo uporaben pri prihodnjih raziskavah na področju projektiranja komponent, ki so izpostavljene toplotnemu utrujanju, npr. v jedrskih elektrarnah.

**Ključne besede: toplotno utrujanje, numerična simulacija, SS316L, obodna napetost, napredovanje razpoke, J-integral**

# Uklon spojenih kompozitnih koničnih lupin pod aksialnimi tlačnimi obremenitvami po teoriji strižnih deformacij

Mohammad Hadi Izadi – Shahrokh Hosseini Hashemi\* – Moharam Habibnejad Korayem  
Iranska univerza za znanost in tehnologijo, Oddelek za strojništvo, Iran

Članek obravnava kritične uklonske obremenitve pri spojenih koničnih lupinah pod vplivom aksialnega tlaka. Konične lupinaste konstrukcije se uporabljajo v raznih aplikacijah kot so rezervoarji za skladiščenje ogljikovodikov, naprave v rafinerijah, hladilni stolpi, ohišja in vmesniki izstrelkov, trupi letal, šobe izstrelkov in reaktivnih motorjev, cevovodi in tankerji za transport kapljev, naprave v elektrarnah, turbine in tlačne posode, trupi podmornic ter različne konstrukcije in silosi.

Pregled literature je pokazal, da obstaja le malo študij spojenih lupin. Večina raziskav je omejenih na spojene cilindrično-konične lupine in na tanke lupine. Obravnavane lupine so bile poleg tega pogosto izdelane iz elastičnih izotropnih homogenih materialov.

V predstavljeni študiji so bile raziskane uklonske lastnosti spojenih koničnih lupin pod aksialno obremenitvijo ob upoštevanju vpliva strižne deformacije. Klasični linearni uklon spojenih stožcev, izdelanih iz križnih laminatov, ojačenih z vlakni, je bil preučen z analitičnim pristopom.

Vodilne enačbe so bile določene po teoriji strižne deformacije prvega reda (FSDT) in za določitev kritičnih uklonskih obremenitev je bila uporabljena analitična rešitev. Sistem parcialnih diferencialnih enačb je bil razrešen z ločitvijo spremenljivk z razvojem v Fourierjevo vrsto in po metodi razvoja v potenčno vrsto. Preučen je bil vpliv števila slojev, vrstnega reda laminacije, polkota ob vrhu, debeline lupin, dolžine lupin in robnih pogojev na stabilnost spojenih stožcev. Validacija je bila opravljena s primerjavo rezultatov pričujoče in predhodnih študij. Za analizo po metodi končnih elementov je bila uporabljena programska oprema ABAQUS/CAE. Rezultati predstavljene metode se dobro ujemajo z rezultati simulacije po metodi končnih elementov in drugimi.

V območju približevanja polkotov nastopi ostro zmanjšanje uklonske obremenitve. Z drugimi besedami: pri krajših lupinah se uklonska obremenitev hitro zmanjša na mestu, kjer se približata polkota dveh lupin. Sledi ugotovitev, da ima uporaba dveh spojenih lupin z ustrežno izbranima polkotoma prednost pred uporabo enotnega stožca. Pri tankih lupinah je konstrukcija najbolj toga pri skoraj identičnih polkotih, pri debelejših lupinah pa ima togost lupin zaradi debeline večji vpliv kot polkoti lupin, ki izhajajo iz geometrije. Uklonska obremenitev je minimalna, ko je ena od lupin ploščata.

Pridobljene ugotovitve za debele lupine bo mogoče primerjati z rezultati prihodnjih raziskav na osnovi HSDT. Raziskati bo mogoče tudi vpliv transverzalnih in rotacijskih obremenitev ter aksialnih in obodnih ojačitev na stabilnost spojenih lupin. Prihodnje raziskave se bodo lahko osredotočile tudi na eksperimentalno analizo uklona spojenih stožcev. Uklon spojenih koničnih lupin končno tudi še ni bil analiziran po metodi GDQM in rezultate GDQM bo tako mogoče primerjati z rezultati razvoja v potenčno vrsto.

**Ključne besede:** uklon, spojena laminirana konična lupina, strižna deformacija prvega reda, potenčna vrsta, MKE, aksialni tlak, križna laminacija

# Študija vplivnih parametrov vtiskovanja krogle za opredelitev nadzorne funkcije lastnosti materiala pri preoblikovalnih operacijah

Roman Satošek<sup>1</sup> – Michal Valeš<sup>2</sup> – Tomaž Pepelnjak<sup>1,\*</sup>

<sup>1</sup>Univerza v Ljubljani, Fakulteta za strojništvo, Slovenija

<sup>2</sup>Češka tehniška univerza v Pragi, Fakulteta za strojništvo, Češka republika

Odstopanja od predpisanih lastnosti preoblikovanega izdelka v sodobnih, prilagodljivih preoblikovalnih procesih se delijo na napake in motnje delovanja proizvodnega procesa. Za boljši nadzor nad proizvodnjo je potrebno zmanjšati motnje v procesu preoblikovanja. V ta namen je bil uveden nov in inovativen sistem pretoka podatkov, ki je za vse materialne parametre povezan v novo opredeljeno "funkcijo nadzora lastnosti materiala". Za sprotni nadzor proizvodne linije pri procesih preoblikovanja in pridobivanje potrebnih materialnih podatkov je bil izveden preizkus vtiskovanja krogle v merjen material. Glavni parametri, ki jih je treba pri tem upoštevati, so vrednosti izbočenja ali vbočenja preoblikovane okolice kalote po vtisnjenju orodja v obliki krogle ob upoštevanju anizotropnega popisa materiala. Parametrična študija primernosti preskusa vtiskovanja krogle je izvedena na podlagi materialnih podatkov aluminijeve zlitine AW 5754-H22. Metoda končnih elementov (MKE) je uporabljena za oceno vplivov premera krogle orodja, kontaktnega trenja in zgodovine preoblikovanja uporabljenega materiala. Novost tega pristopa in znanstven doprinos dela pri vtiskovanju krogle v material sta: a) povezava linearne korelacije izbočenja z globino vtiskovanja krogle opredeljeno z naklonom  $k$ , in b) povezava naklona  $k$  z različnimi prednapetostmi z novo potenčno funkcijo. Slednja predstavlja nov koncept parametričnega popisa vplivov materiala na proces vtiskovanja in se ga bo v bodoče integriralo v krmilne sisteme preoblikovalnih procesov.

V članku je predstavljena linearna korelacija ter definicija nove potenčne funkcije opredeljene s parametri  $a$ ,  $f_0$  in  $b$  povezave med gradientom razmerja  $s_u$  napram  $h$  v odvisnosti od tehnološke zgodovine materiala izvedena za primer aluminijeve zlitine AW 5754-H22. Za njen popis potrebujemo opredelitev naslednjih robnih pogojev: velikosti vtiskovane krogle, vpliva debeline materiala, globine odtisa ter kontaktnega trenja. Našteti robni pogoji so s pomočjo MKE vrednoteni napram višini izbočenja po vtiskovanju krogle v material. Za primer analize trenja so dobljeni numerični rezultati tudi eksperimentalno preverjeni. Ugotovljeno je ujemanje med MKE in eksperimentom pri koeficientu Coulombovega trenja z vrednostjo  $\mu=0.2$ , ki se v nadaljevanju raziskav uporabi pri izvedbi študije o vplivu anizotropije ter tehnološke zgodovine opazovanega materiala. V MKE je uporabljen Hillov potencialni kriterij tečenja, ki upošteva anizotropne lastnosti materiala. Za popis Hillovih potencialov je uporabljena napetost tečenja v smeri valjanja ter eksperimentalno pridobljeni Lankfordovi parametri anizotropije materiala  $r$  ( $r_0$ ,  $r_{45}$  in  $r_{90}$ ).

Trenje ima pomemben vpliv na izbočenje in zmanjšuje njegovo vrednost. V primeru anizotropnega materiala je izbočenje odvisno od smeri valjanja. Popis odvisnosti se prikaže z naklonom linije v  $s_u-h$  diagramu. Naklon v smeri  $\theta=45^\circ$  je najbližji naklonu pri izotropnem material, medtem ko je pri  $\theta=0^\circ$  nagib povečan in obratno, pri  $\theta=90^\circ$  je manjši kot pri izotropnem materialu.

Tehnološko zgodovino materiala je mogoče zabeležiti s pomočjo linearne odvisnosti med izbočenjem in globino kalote pri čemer ob večjem gradientu navedene odvisnosti, ki je posledica pred-utrjevanja zaradi tehnološke zgodovine materiala, dosežemo opazovano ciljno deformacijo pri nižjih kalotah kot v primeru mehko žarjenega deviškega materiala.

Študija omogoča nadaljevanje raziskav opredeljenega modela generatorja kontrolnih funkcij za nadzor preoblikovalnega procesa. Prav tako odpira vprašanja generalizacije novo opredeljene potenčne funkcije povezave med gradientom razmerja  $s_u$  napram  $h$  v odvisnosti od tehnološke zgodovine na različne kovinske materiale, njeno generalizacijo in njeno implementacijo v krmilno funkcijo za nadzor preoblikovalnega procesa.

**Ključne besede:** test vtiskovanja, anizotropija, sprotni nadzorni sistem, preoblikovalni proces, parametrična študija

# Omejevanje samovzbujenih vibracij pri rotacijskih strojih z listnatimi vzmetmi

Chang Wang<sup>1</sup> – Jun Liu<sup>1,2,\*</sup> – Zhiwei Luo<sup>3</sup>

<sup>1</sup> Državni laboratorij za napredne mehatronske sisteme in inteligentno vodenje, Tehniška univerza v Tianjinu, Kitajska

<sup>2</sup> Nacionalni demonstracijski center za eksperimentalno delo pri pouku strojništva in elektrotehnike, Tehniška univerza v Tianjinu, Kitajska

<sup>3</sup> Organizacija za napredno znanost in tehnologijo, Univerza v Kobeju, Japonska

Pri delovanju rotacijskih strojev nad zgornjo kritično hitrostjo se zaradi notranjega trenja na gredi pojavljajo samovzbujene vibracije. V članku je preučen mehanizem nastanka samovzbujenih vibracij in predstavljena učinkovita metoda za omejevanje samovzbujenih vibracij z listnatimi vzmetmi.

Lastnosti rotorjev z listnatimi vzmetmi so bile sistematično preučene z numeričnimi simulacijami in teoretično analizo. Teoretična analiza vibracijskih lastnosti rotorskih sistemov po večskalni perturbacijski metodi in metodi harmoničnega ravnovesja je težavna zaradi notranjih dušilnih členov. V tej študiji je bila uporabljena izboljšana strelna metoda za pridobivanje aproksimativnih rešitev za harmonično komponento. Veljavnost predlagane metode omejevanja vibracij je bila preverjena tudi eksperimentalno.

Pojavi notranjega trenja se razvrščajo v histerezo dušenje zaradi notranjega trenja v materialu gredi in v strukturno dušenje zaradi suhega trenja med gredjo in zunanji elementi. Strukturno dušenje rotorja v tem primeru šteje v notranje dušenje. Ob upoštevanju sil dušenja in elastičnih sil listnatih vzmeti so bile pridobljene enačbe dinamike rotorskega sistema. Na podlagi analize lastnih frekvenc je bilo ugotovljeno, da imajo sile dušenja listnatih vzmeti velik vpliv na glavno kritično hitrost rotorskega sistema, ki se povečuje z rastjo koeficienta dušilnih sil. Za pridobivanje aproksimativnih rešitev za rotorski sistem v pogojih ravnotežja in neravnotežja sta bili uporabljeni metoda harmoničnega ravnotežja in izboljšana strelna metoda. V kombinaciji z numeričnimi simulacijami so bili pridobljeni resonančni odzivi za analizo vibracijskih lastnosti rotorskega sistema.

Amplituda samovzbujenih vibracij v pogojih brez neravnotežja se je bistveno zmanjšala s povečanjem koeficienta dušilnih sil. Ko ta doseže kritično vrednost, ne more priti do samovzbujenih vibracij. Harmonične vibracije in samovzbujene vibracije v pogojih brez neravnotežja so praktično neodvisne, skoraj periodična gibanja pa se pojavljajo zaradi seštevanja harmoničnih in samovzbujenih vibracij. Listnate vzmeti lahko učinkovito omejijo samovzbujene vibracije v širokem razponu vrtilnih frekvenc. Za preverjanje učinkovitosti predlagane metode omejevanja je bil zgrajen enorotorski sistem z listnatimi vzmetmi. Puša omogoča nastavitev sile prednapetosti med pušo in gredjo, notranja sila dušenja pa se prilagaja z uravnavanjem sile zategovanja puše. Pod diskom je vgrajen krogljčni ležaj. Štirje paketi listnatih vzmeti se dotikajo zunanjega obroča ležaja na štirih mestih. Vsak paket listnatih vzmeti je sestavljen iz treh listov različnih dolžin in med listi nastane suho trenje. Brez listnatih vzmeti pri vrtilnih frekvencah nad zgornjo kritično hitrostjo nastopijo samovzbujene vibracije in validacija mejnega cikla ni mogoča. Rezultati eksperimentov z listnatimi vzmetmi so pokazali odsotnost samovzbujenih vibracij nad glavno kritično hitrostjo tudi ko je rotorski sistem z listnatimi vzmetmi izpostavljen ponavljajočim se motnjam.

Raziskava je bila osredotočena na vibracijske lastnosti pri vrtilnih frekvencah v bližini glavne kritične hitrosti. V prihodnje bodo raziskane še vibracijske lastnosti v bližini podharmonične resonance reda 1/2, saj ima rotorski sistem eliptične orbite.

Rezultate teoretičnih analiz in numeričnih simulacij potrjujejo tudi rezultati eksperimentov: z listnatimi vzmetmi je mogoče omejiti samovzbujene vibracije nad glavno kritično hitrostjo.

**Ključne besede:** rotorski sistem, samovzbujene vibracije, notranje dušenje, omejevanje vibracij, listnata vzmet, eksperiment

# Information for Authors

All manuscripts must be in English. Pages should be numbered sequentially. The manuscript should be composed in accordance with the Article Template given above. The maximum length of contributions is 10 pages. Longer contributions will only be accepted if authors provide justification in a cover letter. For full instructions see the Information for Authors section on the journal's website: <http://en.sv-jme.eu>.

## SUBMISSION:

Submission to SV-JME is made with the implicit understanding that neither the manuscript nor the essence of its content has been published previously either in whole or in part and that it is not being considered for publication elsewhere. All the listed authors should have agreed on the content and the corresponding (submitting) author is responsible for having ensured that this agreement has been reached. The acceptance of an article is based entirely on its scientific merit, as judged by peer review. Scientific articles comprising simulations only will not be accepted for publication; simulations must be accompanied by experimental results carried out to confirm or deny the accuracy of the simulation. Every manuscript submitted to the SV-JME undergoes a peer-review process.

The authors are kindly invited to submit the paper through our web site: <http://ojs.sv-jme.eu>. The Author is able to track the submission through the editorial process - and will participate in the copyediting and proofreading of submissions accepted for publication - by logging in, and using the username and password provided.

## SUBMISSION CONTENT:

The typical submission material consists of:

- A **manuscript** (A PDF file, with title, all authors with affiliations, abstract, keywords, highlights, inserted figures and tables and references),
  - Supplementary files:
    - a **manuscript** in a WORD file format
    - a **cover letter** (please see instructions for composing the cover letter)
    - a ZIP file containing **figures** in high resolution in one of the graphical formats (please see instructions for preparing the figure files)
    - possible **appendices** (optional), cover materials, video materials, etc.
- Incomplete or improperly prepared submissions will be rejected with explanatory comments provided. In this case we will kindly ask the authors to carefully read the Information for Authors and to resubmit their manuscripts taking into consideration our comments.

## COVER LETTER INSTRUCTIONS:

Please add a **cover letter** stating the following information about the submitted paper:

1. **Paper title**, list of **authors** and their **affiliations**.
2. **Type of paper**: original scientific paper (1.01), review scientific paper (1.02) or short scientific paper (1.03).
3. A **declaration** that neither the manuscript nor the essence of its content has been published in whole or in part previously and that it is not being considered for publication elsewhere.
4. State the **value of the paper** or its practical, theoretical and scientific implications. What is new in the paper with respect to the state-of-the-art in the published papers? Do not repeat the content of your abstract for this purpose.
5. We kindly ask you to suggest at least two **reviewers** for your paper and give us their names, their full affiliation and contact information, and their scientific research interest. The suggested reviewers should have at least two relevant references (with an impact factor) to the scientific field concerned; they should not be from the same country as the authors and should have no close connection with the authors.

## FORMAT OF THE MANUSCRIPT:

The manuscript should be composed in accordance with the Article Template. The manuscript should be written in the following format:

- A **Title** that adequately describes the content of the manuscript.
- A list of **Authors** and their **affiliations**.
- An **Abstract** that should not exceed 250 words. The Abstract should state the principal objectives and the scope of the investigation, as well as the methodology employed. It should summarize the results and state the principal conclusions.
- 4 to 6 significant **key words** should follow the abstract to aid indexing.
- 4 to 6 **highlights**; a short collection of bullet points that convey the core findings and provide readers with a quick textual overview of the article. These four to six bullet points should describe the essence of the research (e.g. results or conclusions) and highlight what is distinctive about it.
- An **Introduction** that should provide a review of recent literature and sufficient background information to allow the results of the article to be understood and evaluated.
- A **Methods** section detailing the theoretical or experimental methods used.
- An **Experimental section** that should provide details of the experimental set-up and the methods used to obtain the results.
- A **Results** section that should clearly and concisely present the data, using figures and tables where appropriate.
- A **Discussion** section that should describe the relationships and generalizations shown by the results and discuss the significance of the results, making comparisons with previously published work. (It may be appropriate to combine the Results and Discussion sections into a single section to improve clarity.)
- A **Conclusions** section that should present one or more conclusions drawn from the results and subsequent discussion and should not duplicate the Abstract.
- **Acknowledgement** (optional) of collaboration or preparation assistance may be included. Please note the source of funding for the research.
- **Nomenclature** (optional). Papers with many symbols should have a nomenclature that defines all symbols with units, inserted above the references. If one is used, it must contain all the symbols used in the manuscript and the definitions should not be repeated in the text. In all cases, identify the symbols used if they are not widely recognized in the profession. Define acronyms in the text, not in the nomenclature.
- **References** must be cited consecutively in the text using square brackets [1] and collected together in a reference list at the end of the manuscript.
- **Appendix(-ies)** if any.

## SPECIAL NOTES

**Units:** The SI system of units for nomenclature, symbols and abbreviations should be followed closely. Symbols for physical quantities in the text should be written in italics (e.g.  $v$ ,  $T$ ,  $n$ , etc.). Symbols for units that consist of letters should be in plain text (e.g.  $\text{ms}^{-1}$ , K, min, mm, etc.). Please also see: <http://physics.nist.gov/cuu/pdf/sp811.pdf>.

**Abbreviations** should be spelt out in full on first appearance followed by the abbreviation in parentheses, e.g. variable time geometry (VTG). The meaning of symbols and units

belonging to symbols should be explained in each case or cited in a **nomenclature** section at the end of the manuscript before the References.

**Figures** (figures, graphs, illustrations digital images, photographs) must be cited in consecutive numerical order in the text and referred to in both the text and the captions as Fig. 1, Fig. 2, etc. Figures should be prepared without borders and on white grounding and should be sent separately in their original formats. If a figure is composed of several parts, please mark each part with a), b), c), etc. and provide an explanation for each part in Figure caption. The caption should be self-explanatory. Letters and numbers should be readable (Arial or Times New Roman, min 6 pt with equal sizes and fonts in all figures). Graphics (submitted as supplementary files) may be exported in resolution good enough for printing (min. 300 dpi) in any common format, e.g. TIFF, BMP or JPG, PDF and should be named Fig1.jpg, Fig2.tif, etc. However, graphs and line drawings should be prepared as vector images, e.g. CDR, AI. Multi-curve graphs should have individual curves marked with a symbol or otherwise provide distinguishing differences using, for example, different thicknesses or dashing.

**Tables** should carry separate titles and must be numbered in consecutive numerical order in the text and referred to in both the text and the captions as Table 1, Table 2, etc. In addition to the physical quantities, such as  $t$  (in italics), the units [s] (normal text) should be added in square brackets. Tables should not duplicate data found elsewhere in the manuscript. Tables should be prepared using a table editor and not inserted as a graphic.

## REFERENCES:

A reference list must be included using the following information as a guide. Only cited text references are to be included. Each reference is to be referred to in the text by a number enclosed in a square bracket (i.e. [3] or [2] to [4] for more references; do not combine more than 3 references, explain each). No reference to the author is necessary.

References must be numbered and ordered according to where they are first mentioned in the paper, not alphabetically. All references must be complete and accurate. Please add DOI code when available. Examples follow.

### Journal Papers:

Surname 1, Initials, Surname 2, Initials (year). Title. Journal, volume, number, pages, DOI code.

- [1] Hackenschmidt, R., Alber-Laukant, B., Rieg, F. (2010). Simulating nonlinear materials under centrifugal forces by using intelligent cross-linked simulations. *Strojniški vestnik - Journal of Mechanical Engineering*, vol. 57, no. 7-8, p. 531-538, DOI:10.5545/sv-jme.2011.013.

Journal titles should not be abbreviated. Note that journal title is set in italics.

### Books:

Surname 1, Initials, Surname 2, Initials (year). Title. Publisher, place of publication.

- [2] Groover, M.P. (2007). *Fundamentals of Modern Manufacturing*. John Wiley & Sons, Hoboken.

Note that the title of the book is italicized.

### Chapters in Books:

Surname 1, Initials, Surname 2, Initials (year). Chapter title. Editor(s) of book, book title. Publisher, place of publication, pages.

- [3] Carbone, G., Ceccarelli, M. (2005). Legged robotic systems. Kordić, V., Lazinica, A., Merdan, M. (Eds.), *Cutting Edge Robotics*. Pro literatur Verlag, Mammendorf, p. 553-576.

### Proceedings Papers:

Surname 1, Initials, Surname 2, Initials (year). Paper title. Proceedings title, pages.

- [4] Štefanič, N., Martinčević-Mikić, S., Tošanović, N. (2009). Applied lean system in process industry. *MOTSP Conference Proceedings*, p. 422-427.

### Standards:

Standard-Code (year). Title. Organisation. Place.

- [5] ISO/DIS 16000-6.2:2002. *Indoor Air - Part 6: Determination of Volatile Organic Compounds in Indoor and Chamber Air by Active Sampling on TENAX TA Sorbent, Thermal Desorption and Gas Chromatography using MSD/FID*. International Organization for Standardization. Geneva.

### WWW pages:

Surname, Initials or Company name. Title, from <http://address>, date of access.

- [6] Rockwell Automation. Arena, from <http://www.arenasimulation.com>, accessed on 2009-09-07.

## EXTENDED ABSTRACT:

When the paper is accepted for publishing, the authors will be requested to send an **extended abstract** (approx. one A4 page or 3500 to 4000 characters). The instruction for composing the extended abstract are published on-line: <http://www.sv-jme.eu/information-for-authors/>.

## COPYRIGHT:

Authors submitting a manuscript do so on the understanding that the work has not been published before, is not being considered for publication elsewhere and has been read and approved by all authors. The submission of the manuscript by the authors means that the authors automatically agree to transfer copyright to SV-JME when the manuscript is accepted for publication. All accepted manuscripts must be accompanied by a Copyright Transfer Agreement, which should be sent to the editor. The work should be original work by the authors and not be published elsewhere in any language without the written consent of the publisher. The proof will be sent to the author showing the final layout of the article. Proof correction must be minimal and executed quickly. Thus it is essential that manuscripts are accurate when submitted. Authors can track the status of their accepted articles on <http://en.sv-jme.eu/>.

## PUBLICATION FEE:

Authors will be asked to pay a publication fee for each article prior to the article appearing in the journal. However, this fee only needs to be paid after the article has been accepted for publishing. The fee is 380 EUR (for articles with maximum of 6 pages), 470 EUR (for articles with maximum of 10 pages), plus 50 EUR for each additional page. The additional cost for a color page is 90.00 EUR. These fees do not include tax.

Strojniški vestnik - Journal of Mechanical Engineering  
Aškerčeva 6, 1000 Ljubljana, Slovenia,  
e-mail: [info@sv-jme.eu](mailto:info@sv-jme.eu)



<http://www.sv-jme.eu>

# Contents

## Papers

- 539 David Muženič, Jaka Dugar, Davorin Kramar, Matija Jezeršek, Franci Pušavec:  
**Improvements in Machinability of Zinc Oxide Ceramics  
by Laser-Assisted Milling**
- 547 Daniel Miler, Stanko Škec, Branko Katana, Dragan Žeželj:  
**An Experimental Study of Composite Plain Bearings:  
The Influence of Clearance on Friction Coefficient and Temperature**
- 557 Thangavel Yuvaraj, Paramasivam Suresh:  
**Analysis of EDM Process Parameters on Inconel 718  
Using the Grey-Taguchi and Topsis Methods**
- 565 Fariha Mukhtar, Faisal Qayyum, Hassan Elahi, Masood Shah:  
**Studying the Effect of Thermal Fatigue on Multiple Cracks Propagating  
in an SS316L Thin Flange on a Shaft Specimen Using a Multi-Physics  
Numerical Simulation Model**
- 574 Mohammad Hadi Izadi, Shahrokh Hosseini Hashemi,  
Moharam Habibnejad Korayem:  
**Buckling of Joined Composite Conical Shells Using Shear Deformation Theory  
under Axial Compression**
- 585 Roman Satošek, Michal Valeš, Tomaž Pepelnjak:  
**Study of Influential Parameters of the Sphere Indentation Used  
for the Control Function of Material Properties in Forming Operations**
- 599 Chang Wang, Jun Liu, Zhiwei Luo:  
**Suppression of Self-Excited Vibrations in Rotating Machinery  
Utilizing Leaf Springs**